VARIABILITY OF INTEGRATED WATER VAPOUR: AN ASSESSMENT ON VARIOUS SCALES WITH OBSERVATIONS AND MODEL SIMULATIONS OVER GERMANY

INAUGURAL–DISSERTATION

ZUR

ERLANGUNG DES DOKTORGRADES

DER MATHEMATISCH-NATURWISSENSCHAFTLICHEN FAKULTÄT

DER UNIVERSITÄT ZU KÖLN

VORGELEGT VON

SANDRA STEINKE

AUS LANGENFELD (RHLD.)

BERICHTERSTATTER:
Prof. Dr. Susanne Crewell
Prof. Dr. Roel Neggers

TAG DER MÜNDLICHEN PRÜFUNG:
19.1.2017

ABSTRACT

Since water vapour plays a key role in several atmospheric processes on various scales including cloud formation and precipitation it is highly variable in both space and time. The characterization and quantification of its variability is crucial for improvement in parametrization of subgrid scale processes in climate and weather prediction models as well as for evaluation of highly resolving simulations. The present work focuses on the characterization and quantification of integrated water vapour (IWV) variability on meso-α to meso-γ scales over Germany.

First of all, a multi-instrument intercomparison during the two months of High Definition Clouds and Precipitation for advancing Climate Prediction (HD(CP)^2) Observational Prototype Experiment (HOPE) is performed to provide a realistic error estimate for the individual instruments observing IWV. The campaign took place from 1 April to 31 May 2013 at the Forschungszentrum Jülich (FZJ) in Germany (50.9°N, 6.4°E). During this two-month period, standard instrumentation for observing water vapour at Jülich ObservatorY for Cloud Evolution (JOYCE), including Global Positioning System (GPS) antenna of the GeoForschungsZentrum Potsdam (GFZ), a scanning microwave radiometer (MWR), and a sunphotometer from Aerosol Robotic Network (AERONET), was complemented by frequent radiosoundings and four additional MWRs all within less than 4 km distance of each other. In addition to the ground-based measurements, IWV estimates from two Moderate Resolution Imaging Spectroradiometer (MODIS) retrievals, near infrared (NIR) and infrared (IR), that provide information with spatial resolution of 1 and 3 km, respectively, are available from satellite overpasses. The comparison reveals a good agreement in terms of standard deviation ($\leq 1\,\mathrm{kg\,m^{-2}}$) and correlation coefficient (≥ 0.98). The exception is MODIS, which appears to suffer from insufficient cloud filtering.

Based on the results of the intercomparison, observations of the Germany-wide GPS network are chosen for evaluation of two novel Consortium for Small-scale Modelling (COSMO) reanalyses — COSMO-REA2 and COSMO-REA6 — and ERA-Interim to assess their ability to represent IWV. The two highly resolved COSMO reanalyses exhibit a distinctly lower median standard deviation ($1.6\,\mathrm{kg\,m^{-2}}$) than the global reanalysis ERA-Interim ($2.4\,\mathrm{kg\,m^{-2}}$) over all GPS stations. In this context it is also shown that a full reanalyses is superior to a dynamical downscaling which is computationally less costly.

For the assessment of the variability of IWV multiple methods are applied. The analysis of the auto-correlation of GPS observations

and COSMO-REA6 simulation shows the importance of synoptic processes on meso-α scale and the analysis of the power spectrum shows a clear seasonal dependency of IWV variability. On meso-γ scales, standard deviations of IWV derived from MWR measurements reveal high variability ($> 1\,\mathrm{kg\,m^{-2}}$) even at time scales of a few minutes. This variability cannot be captured by measurements with lower temporal resolution. However, for time intervals above 30 min, observations with 15 min resolution are as capable as MWR to capture the temporal variability. Spatio-temporal variability is assessed with the ICOsahedral Non-hydrostatic (ICON) simulation in Large Eddy Simulation (LES) configuration with a resolution of 156 m for three days. This study reveals that time differences of 30–45 min or a spatial mismatch of 9–10 km can induce standard deviations of approximately $0.7\,\mathrm{kg\,m^{-2}}$. This error depends on the weather situation.

The mean diurnal cycle of IWV is analysed in the COSMO reanalyses, ERA-Interim, and GPS observations for spring and summer. In general, the mean diurnal cycles exhibit a minimum in the morning (4:00–10:00 UTC) and a maximum between 14:00 and 23:00 UTC. While the amplitudes of the mean diurnal cycle of IWV observed with GPS vary between 0.4 and $2.0\,\mathrm{kg\,m^{-2}}$ (3.0–13.7%) in spring and 0.4–$2.6\,\mathrm{kg\,m^{-2}}$ (1.4–12.0%) in summer, the mean diurnal cycle simulated with the reanalyses exhibits smaller amplitudes and lower variability in their amplitudes. Also regional differences are found: coastal regions exhibit a shifted diurnal cycle with lower amplitudes while high altitudes exhibit larger amplitudes. Furthermore, the distinction between western and eastern weather situations shows that the strong advection of water vapour associated with western weather situations interferes with the evolution of the diurnal cycle.

The reanalysis COSMO-REA6 covering a time period of 19 years allows for assessing regional analysis of trends in IWV. Mean trends of 0.32 and $0.21\,\mathrm{kg\,m^{-2}}$ per decade are analysed for COSMO-RE6 and ERA-Interim, respectively.

The present work characterizes IWV variability on meso scales over Germany and shows the importance of the consideration of IWV variability e. g. for model evaluations and instrument intercomparisons.

ZUSAMMENFASSUNG

Da Wasserdampf eine Schlüsselrolle in vielen atmosphärischen Prozessen auf unterschiedlichen Skalen, einschließlich Wolkenbildung und Niederschlag, spielt, ist er sowohl räumlich als auch zeitlich sehr variabel. Die Charakterisierung und Quantifizierung seiner Variabilität ist wesentlich für die Verbesserung von Parametrisierungen von Prozessen, die von Klima- und Wettervorhersagemodellen nicht aufgelöst werden können, sowie für die Evaluierung von hoch auflösenden Simulationen. In der vorliegende Arbeit liegt de Schwerpunkt auf der Charakterisierung und Quantifizierung der Variabilität von integriertem Wasserdampf (IWV) auf Skalen von Meso-α bis Meso-γ in Deutschland.

Zuallererst wird ein Messinstrumentenvergleich für den zweimonatigen Zeitraum des High Definition Clouds and Precipitation for advancing Climate Prediction (HD(CP)^2) Observational Prototype Experiments (HOPE) durchgeführt um eine realistische Fehlerabschätzung für die einzelnen Instrumente zu geben. Die Kampagne fand vom 1. April bis zum 31. Mai 2013 am Forschungszentrum Jülich (FZJ) in Deutschland (50,9°N, 6,4°E) statt. Während dieser zwei Monate wurde die standardmäßige Geräteausstattung des Jülich ObservatorY for Cloud Evolution (JOYCE), die eine Global Positioning System (GPS) Antenne des GeoForschungsZentrums Potsdam, ein scannendes Mikrowellenradiometer (MWR) und ein Sonnenphotometer des Aerosol Robotic Network (AERONET) einschließt, ergänzt um regelmäßige Radiosondenaufstiege und vier weitere MWR, wobei alle Geräte in einer Entfernung von weniger als 4 km zueinander positioniert wurden. Zusätzlich zu den bodengebundenen Messungen, stehen IWV Abschätzungen von zwei Moderate Resolution Imaging Spectroradiometer (MODIS) Produkten, aus Messungen im infraroten und nahem infraroten Bereich, von Satellitenüberflügen zur Verfügung, die Information mit einer räumlichen Auflösung von jeweils 1 und 3 km liefern. Der Vergleich zeigt eine gute Übereinstimmung im Hinblick auf Standardabweichung ($\leq 1\,\mathrm{kg\,m^{-2}}$) und Korrelationskoeffizienten ($\geq 0,98$) mit Ausnahme von MODIS, das unter unzureichender Wolkenfilterung leidet.

Basierend auf den Ergebnissen des Vergleichs, werden Messungen des Deutschlandweiten GPS Netzwerks zur Evaluierung zweier neuartiger COSMO Reanalysen — COSMO-REA2 und COSMO-REA6 — verwendet um ihre Darstellung des IWV zu bewerten. Die zwei hoch auflösenden COSMO Reanalysen weisen einen deutlich geringeren Median über alle GPS Stationen der Standardabweichung ($1{,}6\,\mathrm{kg\,m^{-2}}$) auf als ERA-Interim ($2{,}4\,\mathrm{kg\,m^{-2}}$). In diesem Zusammenhang wird

außerdem gezeigt, dass eine vollständige Reanalyse einem dynamischen Downscaling, dass weniger rechenzeitintensiv ist, überlegen ist.

Für die Untersuchung der Variabilität von IWV werden mehrere Methoden angewandt. Die Analyse der Autokorrelation von GPS Messungen und COSMO-REA6 Simulationen zeigt die Bedeutung synoptischer Prozesse auf der Meso-α-Skala. Die Analyse der Spektraldichte zeigt eine deutliche jahreszeitliche Abhängigkeit der IWV Variabilität. Auf Meso-γ-Skalen zeigen die Standardabweichungen von IWV, gemessen mit einem MWR, sogar auf Zeitskalen von wenigen Minuten eine hohe Variabilität ($> 1\,\mathrm{kg\ m^{-2}}$). Diese Variabilität kann von Messungen mit einer geringeren zeitlichen Auflösung nicht erfasst werden. Für Zeiträume über 30 min jedoch sind Messungen mit einer zeitlichen Auflösung von 15 min in der Lage die räumliche Variabilität genauso gut wiederzugeben, wie die Messungen mit einem Mikrowellenradiometer. Die räumlich-zeitliche Variabilität wird aus einer Simulation mit dem ICOsahedral Non-hydrostatic (ICON) Modell in Large Eddy Simulations (LES) Konfiguration mit einer Auflösung von 156 m über drei Tage abgeschätzt. Diese Studie zeigt, dass Zeitunterschiede von 30–45 min oder eine räumlich Verschiebung von 9-10 km Standardabweichungen von ca. $0{,}7\,\mathrm{kg\ m^{-2}}$ verursachen kann. Dieser Fehler hängt von der jeweiligen Wettersituation ab.

Der mittlere Tagesgang des IWV im Frühling und Sommer wird in den COSMO Reanalysen, ERA-Interim und GPS Messungen untersucht. Grundsätzlich weist der mittlere Tagesgang ein Minimum am Morgen (4:00–10:00 UTC) und ein Maximum zwischen 14:00 und 23:00 UTC auf. Während die Amplituden des mittleren Tagesgangs des IWV gemessen mit GPS je nach Station zwischen 0,4 und $2{,}0\,\mathrm{kg\ m^{-2}}$ (3,0–13,7%) im Frühling und $0{,}4$–$2{,}6\,\mathrm{kg\ m^{-2}}$ (1,4–12,0%) im Sommer variieren, zeigt der mittlere Tagesgang der Reanalysen kleinere Amplituden und eine geringer Variabilität in den Amplituden. Außerdem werden regionale Unterschiede gefunden: küstennahe Regionen weisen eine Verschiebung im Tagesgang mit kleineren Amplituden auf während in höheren Lagen der Tagesgang größere Amplituden aufweist. Des Weiteren zeigt eine Unterscheidung zwischen westlichen und östlichen Wettersituationen, dass die Wasserdampfadvektion, die mit westlichen Wetterlagen einhergeht, die Entwicklung des Tagesgangs überlagert.

Die Reanalyse COSMO-REA6 deckt einen Zeitraum von 19 Jahren ab und ermöglicht somit die regionale Analyse von Trends im IWV. Mittlere Trends von 0,32 und $0{,}21\,\mathrm{kg\ m^{-2}}$ pro Dekade werden in COSMO-REA6 und ERA-Interim gefunden.

Die vorliegende Arbeit charakterisiert die Meso-skalige Variabilität von IWV in Deutschland und zeigt die Bedeutung der Berücksichtigung von IWV Variabilität z.B. für Modellevaluationen und Instrumentenvergleiche.

CONTENTS

ACRONYMS

AERONET	Aerosol Robotic Network
AIRS	Atmospheric Infrared Sounder
AMSL	above mean sea level
CAM5	Community Atmosphere Model, version 5
CHAMP	CHAllenging Minisatellite Payload
COSMO	Consortium for Small-scale Modelling
COSMIC	Constellation Observing System for Meteorology, Ionosphere, and Climate
CWT	Circulation Weather Type
DIAL	Differential Absorption Lidar
DWD	Deutscher Wetterdienst
ECMWF	European Centre for Medium-range Weather Forecasting
ERA-Interim	European Centre for Medium-range Weather Forecasting (ECMWF) Re-Analysis Interim
FZJ	Forschungszentrum Jülich
GEWEX	Global Energy and Water Cycle Exchanges project
GFDL	Geophysical Fluid Dynamics Laboratory
GFZ	GeoForschungsZentrum Potsdam
GLONASS	GLObal NAvigation Satellite System
GNSS	Global Navigation Satellite System
GNSS-RO	Global Navigation Satellite System-Radio Occultation
GOME	Global Ozone Monitoring Experiment
GPS	Global Positioning System
GRACE	Gravity Recovery And Climate Experiment
G-VAP	Global Energy and Water Cycle Exchanges project (GEWEX) water vapor assessment
HATPRO	Humidity and Temperature Profiler
HD(CP)^2	High Definition Clouds and Precipitation for advancing Climate Prediction
HErZ	Hans-Ertel-Zentrum für Wetterforschung
HOPE	HD(CP)^2 Observational Prototype Experiment
ICON	ICOsahedral Non-hydrostatic
IGS	International GNSS Service
IR	infrared
IWV	integrated water vapour
JOYCE	Jülich ObservatorY for Cloud Evolution
LEO	Low Earth Orbiter
LES	Large Eddy Simulation

LHN	latent heat nudging
LT	local time
MERRA	Modern ERA Retrospective Analysis for Research and Applications
MODIS	Moderate Resolution Imaging Spectroradiometer
MPI-M	Max Planck Institute for Meteorology
MWR	microwave radiometer
NAVSTAR	Navigational Satellite Timing and Ranging
NIR	near infrared
NWP	numerical weather prediction
NRT	near real-time
PPP	Precise Point Positioning
SAPOS	Satellite Positioning
SCIAMACHY	SCanning Imaging Absorption spectrometer for Atmospheric CHartographY
SSM/I	Special Sensor Microwave Imager
SYNOP	surface synoptic observations
WMO	World Meteorological Organization
ZHD	Zenith Hydrostatic Delay
ZTD	Zenith Total Delay
ZWD	Zenith Wet Delay

Part I

INTRODUCTION

1 INTRODUCTION

1.1 MOTIVATION

Due to its influence on atmospheric processes on various scales, the importance of atmospheric water vapour cannot be underestimated. It is not only the most effective greenhouse gas (Kiehl and Trenberth, 1997) but it plays also a key role in other major atmospheric processes including cloud formation and precipitation. It is also involved in surface and dynamic processes (cf. Fig. 1.1).

Water vapour has an important role in the water cycle (e. g. Bengtsson et al., 2014) as the atmospheric storage term with a residence time of only approximately nine days. Water of clouds, precipitation, soil, and water bodies, especially the ocean, vaporizes to water vapour. Other sources of water vapour are the transpiration of vegetation and in the upper stratosphere methane oxidation. Water vapour is removed from the atmosphere by condensation especially during cloud formation and subsequent precipitation, which in turn increases the soil moisture, the run-off or is transported by rivers to the ocean. In Europe, most of the continental water emanates from the Atlantic and is also returned to the Atlantic. Due to the heterogeneous land surface in terms of vegetation and soil moisture, the water cycle is more complex over land than over ocean. Most of the described processes occur in the planetary boundary layer emphasizing its importance.

Condensation and vaporization are associated with the release or storage of latent heat. Therefore, transport of water vapour is always associated with energy transport. Water vapour transport occurs on different scales: from turbulent mixing in the boundary layer via convection to large-scale advection.

Water vapour interacts with radiation across the whole spectrum. Its absorption properties in the infra-red spectrum make it the most important greenhouse gas. About 60% of the greenhouse effect can be attributed to water vapour (Kiehl and Trenberth, 1997). In combination with the dependency of saturation water vapour pressure on temperature, this results in a positive feedback due to warming. Therefore, analysing trends in the amount of water vapour is important.

Some of the processes involving water vapour as cumulus cloud formation and convection happen on such small scales that they cannot be resolved by numerical weather prediction (NWP) and climate models. These unresolved processes are nevertheless very important for accurate model simulations (Stevens and Bony, 2013). Especially

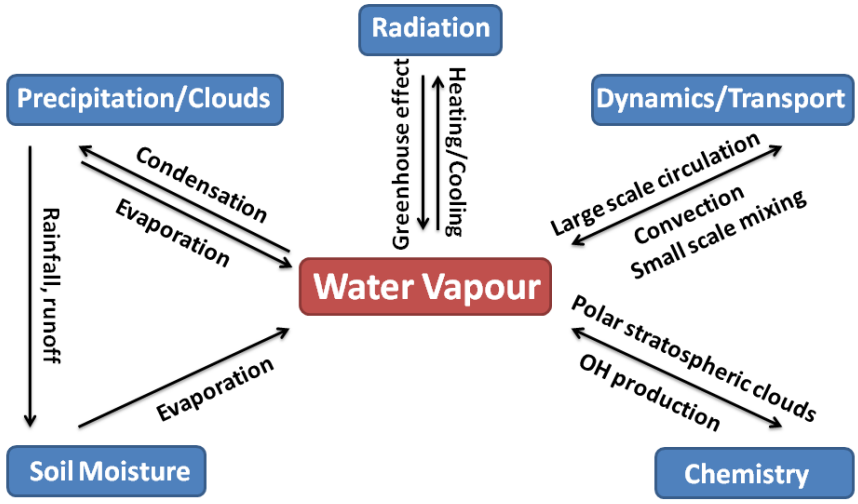

Figure 1.1: The role of water vapour in atmospheric processes (adapted from Gérard et al. (2004)).

the interactions between convection and water vapour are not yet completely understood (Sherwood et al., 2010). Therefore, the understanding of the water vapour distribution is crucial for improvement of the parametrization of these subgrid-scale processes.

The resolution of atmospheric models increased steadily. Thus, they become less prone to uncertainties induced by parametrizations at the cost of computationally expensive simulations. For example within High Definition Clouds and Precipitation for advancing Climate Prediction (HD(CP)^2), the first ever simulation with ICOsahedral Non-hydrostatic (ICON) in Large Eddy Simulation (LES) configuration with a horizontal grid spacing of 156 m on the domain of Germany is run (Heinze et al., 2016). To evaluate these models, measurements resolving these small-scale processes are needed.

Operational measurements with a high temporal resolution of the profile of water vapour do not exist yet especially not within a dense network. Satellites observations could provide water vapour profiles though they are limited due to several reasons. When using observations in the microwave band measurements are only available over ocean which is not suitable for the present work focusing on Germany. Observations in the infrared band are limited to clear sky and they are not able to capture the lower troposphere which is, as mentioned above, crucial for the water cycle.

Measuring the total amount of water vapour within an atmospheric column is much easier. Considering the profile of water vapour it can be seen that at a typical midlatitude site about half of the total amount of water vapour is within the planetary boundary layer, meaning within about the lowest 1200 m, as the main sources are at the surface (Fig. 1.2). Furthermore, the variability of water vapour is highest

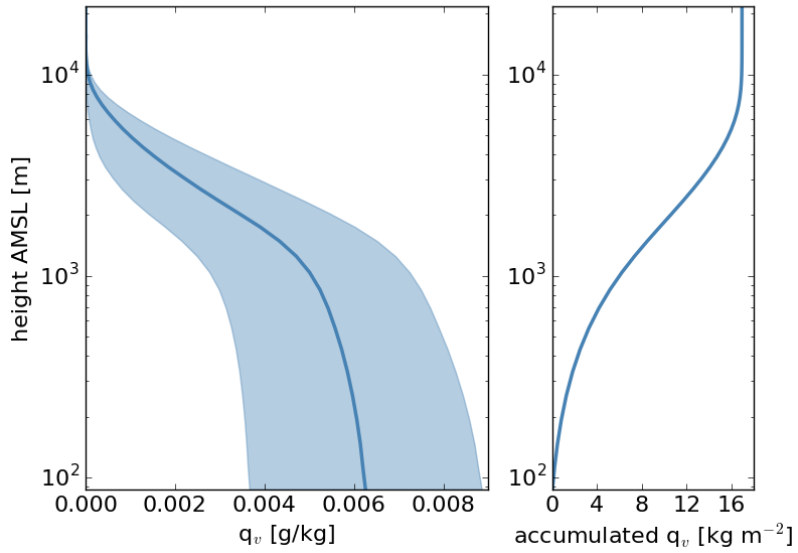

Figure 1.2: (left) solid line: Mean profile of q_v at station 2624 (50.9°N, 7.1°E) between Cologne and Bonn over the years 2007–2013 simulated with COSMO-REA6. shaded area: standard deviation of mean profile. (right) Water vapour integrated up to a distinct height level.

in the planetary boundary layer in absolute values. Although the vertical variability through vertical mixing and advection cannot be seen in the column integrated water vapour (IWV), the temporal and horizontal variability can be reproduced well from IWV measurements.

IWV is defined as the integral of the absolute humidity ρ_v [kgm $-$ 3] from the surface (z_0) to the top of the atmosphere (z_{TOA}):

$$IWV = \int_{z_0}^{z_{TOA}} \rho_v \, \mathrm{d}z. \tag{1.1}$$

Its unit is 1 kg m^{-2}. This is equivalent to 1 mm column of condensed water.

There is no unified naming convention for this variable. Frequently used names are e. g.: total column water vapour, precipitable water, or total-column precipitable water. In the present work the term integrated water vapour (IWV) is used.

A wide range of techniques exists for measuring IWV. Different instruments sample different atmospheric conditions due to different integration times, beam widths, geometries, sampling strategies, locations, etc. To asses which measurements can capture which variabilities, a detailed intercomparison of a large set of instruments is needed. Many studies compare various IWV measurements in different geographical regions and for different time periods using different criteria for temporal and spatial matching and elevation corrections (cf.

Bennouna et al., 2013; Martin et al., 2006; Morland et al., 2009; Pałm et al., 2010; Schneider et al., 2010; Torres et al., 2010). Frequently, these comparisons involve data sets with more than 1 h temporal and more than 20 km spatial difference as well as with different horizontal resolutions. An assessment of the representativeness error is therefore needed. This holds true for relatively small temporal and spatial mismatches of e. g. ground-based instruments as well as for daily averages derived from observations of orbiting satellites which are provided only for one or two overpasses a day for the same location (Diedrich et al., 2016). The same is valid for radiosoundings, which are operationally conducted only once or twice a day at most locations. To evaluate the representativeness of the latter measurements the variations during a day should be assessed. Furthermore, a better understanding of the diurnal cycle of IWV could improve the understanding of the relationship between evaporation and precipitation since these processes determine primarily the amount of IWV.

1.2 OBJECTIVES OF THE PRESENT STUDY

This study aims at the quantification and characterization of IWV variability over a wide range of spatial and temporal scales — from meso-γ (2–20 km) to meso-α (200–2000 km) — over Germany focusing on terrestrial surfaces that are associated with strong variability. To this end, the ability of models and instruments to capture this variability is assessed.

First of all there is the question how well state-of-the-art ground-based instruments can observe IWV variability. Therefore, a multi-instrument intercomparison during the two months of HD(CP)^2 Observational Prototype Experiment (HOPE) is performed to provide a realistic error estimate for the individual instruments observing IWV. A wide range of instruments — Global Positioning System (GPS) antenna, scanning microwave radiometer (MWR), sunphotometer, frequent radiosoundings, infrared and near-infrared MODIS retrievals — is compared. This unique set of observations is used for a statistical intercomparison to assess the representativeness of measurements from instruments with different temporal and spatial resolution and which can measure under different atmospheric conditions. Furthermore, the ability of the continuous measurements to capture variability within time intervals of a few minutes is assessed.

Secondly, the question arises whether IWV reanalysis can provide domain wide and temporal and spatially continuous IWV estimates that cannot be derived from instruments alone. Therefore, an evaluation of the models used in the present study with independent GPS observations is performed to assess how well IWV is represented in the respective model. In the course of this evaluation the question why a dynamical downscaling is not good enough and a full reana-

lysis is needed to assess IWV variability is tackled. The two novel Consortium for Small-scale Modelling (COSMO) reanalyses COSMO-REA2 and COSMO-REA6 performed within Hans-Ertel-Zentrum für Wetterforschung (HErZ) Simmer et al. (2015) are compared with the lower resolved reanalysis ECMWF Re-Analysis Interim (ERA-Interim). To this end, the reanalyses are evaluated with GPS observations. The first ever Large Eddy Simulation (LES) with ICOsahedral Non-hydrostatic (ICON), which is run over Germany within the framework of HD(CP)^2 is also evaluated with GPS. All models are used to assess IWV variability. Therefore, the quality of the simulations has to be evaluated first.

Thirdly, this study aims at the quantification and qualification of IWV variability on meso scales. To this end, the evaluated observations and simulations of IWV are used.

Previous studies assessing water vapour variabilities (e. g. Kahn et al., 2011; Fischer et al., 2012; Pressel et al., 2014) use scale analysis on scales of a few kilometres up to some hundreds of kilometres. However, either these studies do not include the planetary boundary layer, where the absolute variability of water vapour is highest, or/ and they do not assess the meso-γ scale. Therefore, an extension of these analyses to smaller scales is needed. Additionally, the error of representativeness of measurements is assessed.

A further aim of the present work is to characterize the diurnal cycle of IWV, meaning the amplitude, as well as the time of minimum and maximum, focusing on the identification of regional differences and the influence of season and weather situations. Accompanied with a simultaneous analysis of the diurnal cycle of precipitation, a better understanding of the processes influencing the diurnal cycle of IWV can be given. These analyses are performed with GPS observations as well as with reanalyses to assess the suitability of them for the analysis of the water cycle since reanalyses are frequently used for this purpose (e. g. Lorenz and Kunstmann, 2012).

Finally, since water vapour is the most important greenhouse gas and a warming of the atmosphere results in a strong positive feedback, identification and estimation of the trend in IWV is important. In the present study trends in IWV within a time period of up to 19 years (1995–2013) will be analysed in the COSMO reanalyses, ERA-Interim and GPS observations.

Summarized, the overarching question of the present work is:

How large is the variability of IWV on scales from meso-γ (2–20 km) to meso-α (200–2000 km) over Germany?

To assess this question the following scientific questions have to be tackled:

Q1 How well do IWV measurements of different instruments agree?

Q2 Which instrument allows to observe the variability of IWV on which scales?

Q3 To which degree can the COSMO reanalyses, ERA-Interim and ICON reproduce IWV and its variability and what is the benefit of high resolution simulations?

Q4 How variable is IWV on meso scales for time periods between a few minutes and a few days?

Q5 What are the characteristics of the diurnal cycle of IWV and how is it influenced by region, season and weather situation?

Q6 Is there a trend in IWV and how does it differ across Germany?

The present study is structured as follows. Chap. 2 and Chap. 3 provide information about all observations and model simulations which are used to assess the variability of IWV. In Chap. 4, a multi-instrument comparison is given. Chapt. 5 provides an extended evaluation of the three reanalyses COSMO-REA2, COSMO-REA6, and ERA-Interim, and also compares a dynamical downscaling with a full reanalysis. Additionally, ICON in LES configuration is evaluated with GPS observations. The following chapters contain the actual assessment of IWV variabilities. Firstly, in Chap. 6 variability on meso-γ scale and below are assessed with various observations and a highly resolved ICON simulation. Secondly, in Chap. 7 the diurnal cycle of IWV is characterized with reanalyses and GPS observations focusing on the influence of season, region and weather situation. This chapter is complemented by a simultaneous analysis of the diurnal cycle of IWV and precipitation. Thirdly, in Chap. 8 a trend analysis of IWV within reanalyses and GPS observations is performed. Finally, in Chap. 9, the presented results are summarized. Additionally, suggestions for future research are presented.

The multi-instrument comparison as presented in Sect. 4 and the study on temporal IWV variability presented in Sect. 6.3 have recently been published in

Steinke, S., Eikenberg, S., Löhnert, U., Dick, G., Klocke, D., Di Girolamo, P., and Crewell, S. (2015). Assessment of small-scale integrated water vapour variability during HOPE. *Atmospheric Chemistry and Physics*, 15(5):2675–2692.

The evaluation of a dynamical downscaling of ERA-Interim, COSMO-REA6 and ERA-Interim with GPS observations as presented in Sect. 5.1.1 has recently been published in

Bollmeyer, C., Keller, J. D., Ohlwein, C., Wahl, S., Crewell, S., Friederichs, P., Hense, A., Keune, J., Kneifel, S., Pscheidt, I., Redl, S., and Steinke, S. (2015). Towards a high-resolution regional reanalysis for the European CORDEX domain. *Quarterly Journal of the Royal Meteorological Society*, 141(686):1–15.

2

OBSERVATIONS

In order to address the variability of IWV on different spatio-temporal scales and to evaluate various models (Sect. 3), a wide range of instruments — GPS (Sect. 2.1), microwave radiometer (Sect. 2.2), sunphotometer (Sect. 2.4), MODIS (Sect. 2.5), and radiosondes (Sect. 2.3) — is used in this study. The measurement principles of the instruments as well as their error characteristics and limitations are described in the following (Tab. 2.1. An extensive comparison of the instruments for a case study is provided in Sect. 4.

2.1 GLOBAL POSITIONING SYSTEM

The principle of deriving IWV from the signal of Global Navigation Satellite System (GNSS) satellites is based on the fact that the signal transmitted from a satellite is refracted by the atmosphere. This leads to an increase of the path length through the atmosphere (Bevis et al., 1992) because the refraction depends, amongst other things, on the amount of water vapour in the atmosphere.

The two globally operational systems are the US-American Navigational Satellite Timing and Ranging (NAVSTAR) - Global Positioning System (GPS) and the Russian GLObal NAvigation Satellite System (GLONASS) nowadays. The European Galileo and the Chinese BeiDou are currently being developed into operational systems. The four systems differ in number and orbit constellation of their satellites as well as in the frequencies of the emitted signal. Once, all four systems are fully deployed, approximately 120 navigation satellites will be available. Therefore, the combination of GNSS will significantly increase the number of observed satellites and consequently optimize the spatial geometry and improve continuity and reliability of positioning. Nowadays, there are several studies combining two systems, especially GPS with GLONASS or BeiDou (e. g. Cai and Gao, 2013) and also combinations of all four systems (Li et al., 2015).

Beidou is Chinese for the Big Dipper, which includes the north star that was used for navigation.

In general, there are two measurement geometries. Firstly, the signal emitted by a GNSS satellite and refracted by the atmosphere is received by a Low Earth Orbiter (LEO), e. g. the German CHAllenging Minisatellite Payload (CHAMP) satellite, the US/German Gravity Recovery And Climate Experiment (GRACE)-A satellite or the six satellites of the Taiwan/US FORMOSAT-3/Constellation Observing System for Meteorology, Ionosphere, and Climate (COSMIC) mission (Wickert et al., 2009). Then with the so called Global Navigation Satellite System-Radio Occultation (GNSS-RO) method, vertical profiles of

Table 2.1: Temporal resolution, spatial resolution or representativeness, limitations, systematic (s), random (r) or combined error of measurements as found in literature for the instruments used in the present study (from Steinke et al. (2015)).

instrument	temporal resolution	spatial resolution/ representativeness	limitations	uncertainty kg m^{-2} or %	reference
MWR HATPRO	≈2 s	3.5° beam width; 122 m beam width at 2 km height	no measurements during rain	0.5 (s) 0.5-0.8 (r)	Rose et al. (2005)
GPS	15 min	ca. 32 km[a]	no zenith measurement	1-2	Gendt et al. (2004)
sunphotometer	10 min	1.2° beam width	daytime/clear-sky only, direction towards sun	10%	Alexandrov et al. (2009)
Graw DFM-09 radiosonde	at least 1 h	drift up to 100 km	drift, measurement takes ca. 1 h	1.2 (s) 1.7 (r)	Wang and Zhang (2008)
MODIS-NIR	≤6 times per day	1 km	daytime/clear-sky only	5-10%	Gao and Kaufman (2003)
MODIS-IR	≤6 times per day	3 km	clear-sky only	5-10%	Seemann et al. (2003)

a The planetary boundary layer with an assumed height of 2 km contributes most to IWV. The GPS slants with the lowest angles (7°) leave the boundary layer in a distance of approximately 16 km from the GPS station and the slants are on average azimuthally, equally distributed. This leads to a spatial representativeness of 32 km.

atmospheric parameters — temperature and water vapour — starting in the upper boundary layer can be derived globally. Secondly, the signal is received by a receiver on the ground. This geometry allows for deriving integrated parameters as IWV. The latter method is used in this study.

In the following, the general method of GPS is explained and afterwards the configurations used by GFZ for near real-time processing is described. An explanation of the quality checks applied to the data set provided by GeoForschungsZentrum Potsdam (GFZ) follows.

2.1.1 *General method*

The GPS system comprises of two parts: the satellites on the one hand and the network of ground-based stations, consisting of antenna and receiver, on the other hand. 24 GPS satellites are in an orbit at approximately 20 200 km height. They transmit signals with carrier waves with frequencies of 1575.42 MHz (L1) and 1227.60 MHz (L2). These carrier waves are amplitude-modulated with information on position and time of their respective atomic clock.

Since little shifts in the position of the antenna can lead to differences in the derived IWV, the antenna needs to be firmly fixed on ground. The ground-based GPS stations can receive at 12 different channels. That means that such a receiver can detect the signal of up to 12 satellites simultaneously. For the measurements to be scientifically usable, the following criteria need to be fulfilled: Firstly, the signals of at least four satellites need to be received. Secondly, only signals that reach the receiver at an elevation angle higher than 7° are used. This optimum cut-off angle depends on the application. A low cut-off angle implies a good geometry and a low uncertainty in the individual IWV estimates (Ning and Elgered, 2012). However, if the angle is too low, systematic errors are introduced, for example interference by signal multi-path, including scattering (Elósegui et al., 1995). Additionally, the signal is too weak if the path through the atmosphere is too long and the atmosphere is not homogeneous.

In the following, the method to derive the position of the receiver as described, e. g. by Seeber (2008) is summarized. The position of the receiver can be determined by using the pseudo range PR. This is the product of the speed of light c and the time the signal takes from the satellite to the ground-based receiver, i. e. the time difference of the two clocks. It can be determined with an accuracy of a few meters:

$$PR = c(t - T) = R + c(dt - dT) + d_{ion} + d_{tro} + \epsilon \tag{2.1}$$

with satellite clock error dt and receiver clock error dT. R is the slant range between the satellite and receiver, d_{ion} and d_{tro} are the delays

due to ionospheric and tropospheric components, respectively, and ϵ is the the observation noise.

In contrast to the accuracy of a few meters achieved by using PR, the tropospheric delay is in the mm-scale. In order to achieve this high accuracy, the phase difference between the carrier phase of the satellite signal ϕ_{sat} and the reference phase of the receiver ϕ_{rec} is additionally used:

$$\Phi = \lambda(\phi_{sat} - \phi_{rec}) = R + c(dt - dT) + \lambda N + d_{ion} + d_{tro} + \epsilon \quad (2.2)$$

where λ is the wavelength of the carrier wave and N is its integer phase ambiguity. Because of the dispersive nature of the ionosphere, the ionospheric delay can be approximated by combining the measurements of the two frequencies L1 and L2. To eliminate all the unknowns, equations for different time steps and different satellite receiver combinations are set up. This over-determined equation system can be solved e. g. with least square adjustment.

In principle, two approaches exist to derive the tropospheric delay. With the network approach, the tropospheric delay for all receivers within a network is computed simultaneously which leads to a huge computational cost for large networks of a few hundred stations. Instead, the Precise Point Positioning (PPP) is used (Zumberge et al., 1997). This method exhibits an accuracy comparable to the network approach (Stoew et al., 2001) but is much faster for large networks. First, the orbits of the satellites and their clock corrections are determined from a globally distributed network of a few GPS receivers. These parameters are fixed values for each satellite. The following steps are conducted for each station individually.

To derive IWV from the tropospheric delay d_{tro}, the dry tropospheric component is subtracted and the wet delay is mapped to zenith. The Zenith Total Delay (ZTD) is defined as the sum of the Zenith Hydrostatic Delay (ZHD) and the Zenith Wet Delay (ZWD):

$$ZTD = ZHD + ZWD \quad (2.3)$$

To build up a relation with d_{tro}, the mapping functions $m_h(\beta)$ and $m_w(\beta)$ for the hydrostatic delay and the wet delay, respectively, are needed. They depend on the elevation angle β at which the ground station receives the signal of the satellite:

$$d_{tro} = m_h(\beta)ZHD + m_w(\beta)ZWD \quad (2.4)$$

In general, a mapping function is a continued fraction of $\frac{1}{\sin(\beta)}$ with several parameters, which can be some combination of constants and functions of geographic location, local meteorological conditions, and season (Younes and Elmezayen, 2012).

ZHD is approximated by surface pressure p_s, latitude l, and height h of the receiver, with a high accuracy (Saastamoinen, 1972):

$$ZHD = 10^{-6} k_1 R_d \int_z \rho dz \approx k_1' p_s \tag{2.5}$$

with the specific gas constant for dry air $R_d = 287.05\,\mathrm{Jkg^{-1}K^{-1}}$, air density ρ, empirical constant k_1, which is evaluated by actual measurements of the refractive index (Thayer, 1974), and the constant k_1' depending on k_1, height, and latitude of the receiver. The Zenith Wet Delay (ZWD) depends on a function of the weighted mean temperature $k'(T_m)$ and the integral of water vapour density ρ_w :

$$ZWD = k'(T_m) \int_z \rho_w dz. \tag{2.6}$$

The weighted mean temperature can be approximated by a function of the surface temperature T_s, which introduces an error of approximately 2% (Bevis et al., 1992). The surface temperature T_s is used because it can be measured at the GPS station itself or interpolated from the next surface synoptic observations (SYNOP) stations. However, since the diurnal variation of the surface temperature is larger than the diurnal variation of the mean temperature of the atmosphere, this approximation can lead to an error of less than $0.1\,\mathrm{kg\,m^{-2}}$ in the amplitude of the diurnal cycle and a shift of the diurnal cycle by 1 to 2 hours later (Morland et al., 2009).

With equations 2.3 and 2.5, IWV can be written as:

$$IWV = \int_z \rho_w dz = \frac{1}{k(T_s)}(ZTD - ZHD) \tag{2.7}$$

With this technique, IWV can be derived with an accuracy of 1–$2\,\mathrm{kg\,m^{-2}}$ (Gendt et al., 2004), which is an absolute uncertainty. This means it does not depend on the magnitude of IWV.

2.1.2 *Near-Realtime processing at GFZ*

The network of ground-based stations, GFZ makes use of the Satellite Positioning (SAPOS) network operated by the land surveying offices of the federal states (Landesversmessungsämter) and additional own GPS stations. Nearly 300 GPS stations in Germany and some stations abroad are used to derive IWV. The receivers produce rawfiles with a temporal resolution of 30 s.

GFZ uses EPOS software (Gendt et al., 2004) for near real-time (NRT) data processing. This software uses the least squares adjustment. At the beginning of each day the positions of the GPS stations are determined using International GNSS Service (IGS) final products. These positions are fixed for one day. The initial values

for the processing are 3-hourly ultra rapid orbit predictions, which are performed with global hourly IGS data within a sliding 24 h data window. These orbit predictions are used as basis for both orbit and clock adjustment. Higher accuracy of these adjustments is achieved by orbit estimation with data of 20 well-distributed global sites and five additional German stations in a 12 h window.

The next step of data processing uses the precise point positioning which allows parallel computing of several sites in clusters keeping computing time low even for several hundred stations and a high temporal resolution of 15 minutes. Within this step, a system of 40–50 equations, depending on the number of satellites visible to the receiver within the time interval of 15 minutes, is solved with the least squares adjustment to retrieve ZTD for each station. The standard deviation of ZTD (σZTD) is computed from the inversion of the normal equations and scaled with the standard deviation of unit weight computed from the least square residuals (Gendt et al., 2004).

The mapping functions for the dry and wet delay are both continued fractions from Niell (1996) whose coefficients depend on the latitude of the site. Additionally, the coefficients of the mapping function of the dry delay depends on the height above sea level of the observing site and on the day of the year. Surface pressure and surface temperature needed to derive IWV from ZTD are either measured directly at the GPS station or interpolated from the smallest surrounding triangle of SYNOP stations, which is the case for most GPS stations.

A height correction is applied beforehand and stations with a height above 1000 m AMSL are excluded. The RMSE due to the correction of pressure is normally 0.3 hPa and can reach $0.5 - 1$ hPa, which corresponds to 0.2 to 0.4 $\mathrm{kg\,m^{-2}}$ (Gendt et al., 2004).

The near-realtime processed GPS measurements exhibit two distinct features: firstly, they show a jump at the beginning of most full hours, which can be up to 1 $\mathrm{kg\,m^{-2}}$. These jumps are caused because each complete hour is processed at the same time and the retrieval tend to smooth these four quaterhourly measurements. Secondly, even larger differences can be seen between the observations at 23:45 UTC and 00:00 UTC of the next day. This is a known characteristic of the near-real-time processing of GPS data, which is also seen in the investigation of the daily cycle at stations in North America by Dai et al. (2002). The exact reason for this feature is not finally clarified yet and subject of ongoing investigation. However, the measurements of the beginning of the day which exhibit such large differences to the last measurements of the day before also exhibits large σIWV and can be filtered with the quality check described in Sect.. 2.1.3.2.

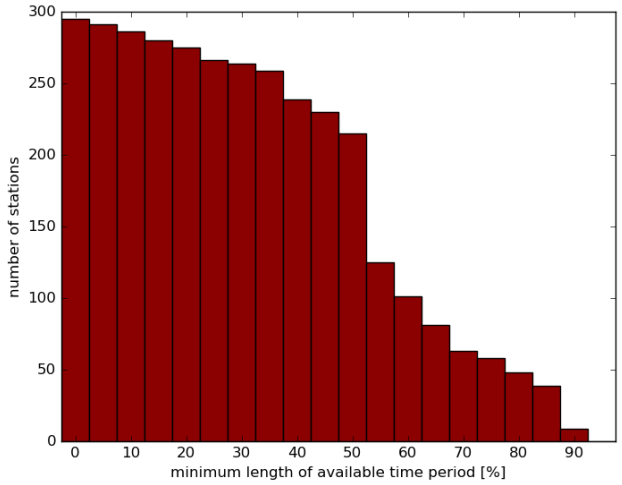

Figure 2.1: Number of GPS stations whose measurement period covers at least a distinct percentage of the time period 2007-2013.

2.1.3 *Quality check for GPS measurements*

GFZ provides a data set with measurements at about 400 GPS stations whereof 294 are located within the domain of COSMO-REA2 with a height difference lower than 200 m to the next reanalysis grid point (cf. Sect. 3.1) as of 1 January 2014. Before GPS measurements are used for any further investigations, a quality check is performed. First, stations with data available for too short time periods and erroneous stations are removed (cf. Sect. 2.1.3.1). Afterwards, single measurements are removed through a plausibility check and a threshold of σIWV is computed during the processing of IWV (cf. Sect. 2.1.3.2).

2.1.3.1 *Quality check of stations*

Visual inspection and different test algorithm have been developed to identify and subsequently remove erroneous stations. Some stations, mainly non-German stations, in general show unrealistic values or behaviour of IWV. The IWV measurements at the station in Brussels, Belgium (BRUS) for example are distinctly lower than close by radiosoundings. This is due to the too low surface pressure used for the processing of the data. Four stations show such biases due to wrong surface pressure. Three stations inhibit regular jumps in the mean diurnal cycle probably due to different data sources of surface pressure used at different times (Fig. 2.2). Furthermore, 19 stations show sudden jumps when differences with a nearby station or model data are analysed. This might occur due to a change of receiver or antenna but cannot be clearly attributed in retrospect. Another five stations show regular patterns in the time series of differences to a nearby sta-

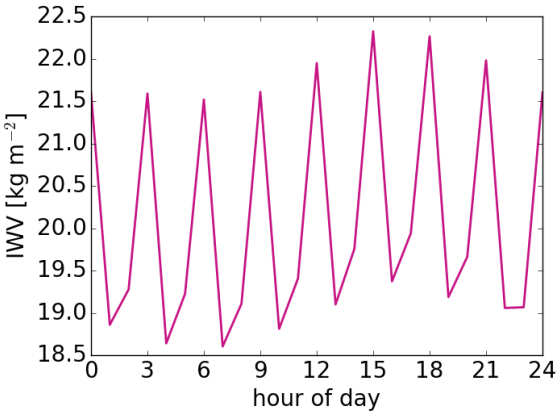

Figure 2.2: Mean diurnal cycle of IWV derived from GPS measurements for the years 2009-2013 at station 0291 in the vicinity of Salzburg (47.8°N, 12.9°E).

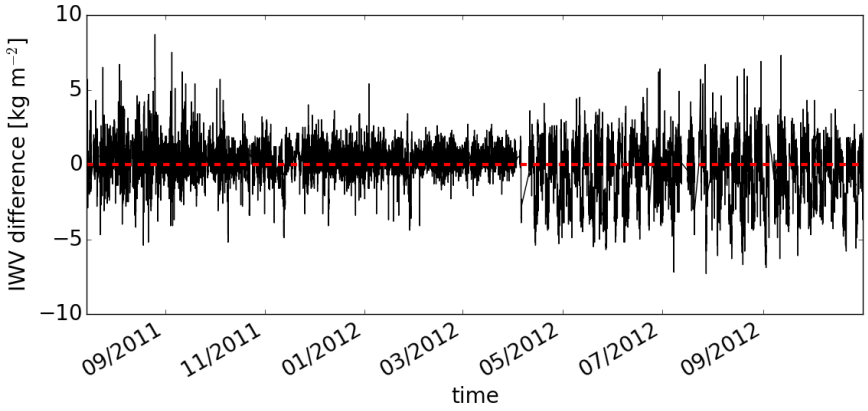

Figure 2.3: Time series of differences between IWV of GPS station 2577 (51.2°N, 6.8°E) and IWV of GPS station 2579 (51.3°N, 6.4°E).

tion for some times (cf. Fig. 2.3) and are rejected. The reason for these patterns is still under investigation. A detailed list of stations with the respective reasons of rejection can be found in Appendix A.

After the quality checks of the stations, 183 of 294 stations (64%) within the domain of COSMO-REA2 remain to be used for further analysis.

2.1.3.2 *Quality check of single of measurements*

Two checks are applied to the measurements: a plausibility check and a check of σIWV. In general, only IWV measurements higher than $1\,\mathrm{kg\,m^{-2}}$ and lower than $50\,\mathrm{kg\,m^{-2}}$ are considered, since measurements outside this range are not considered to be meteorological

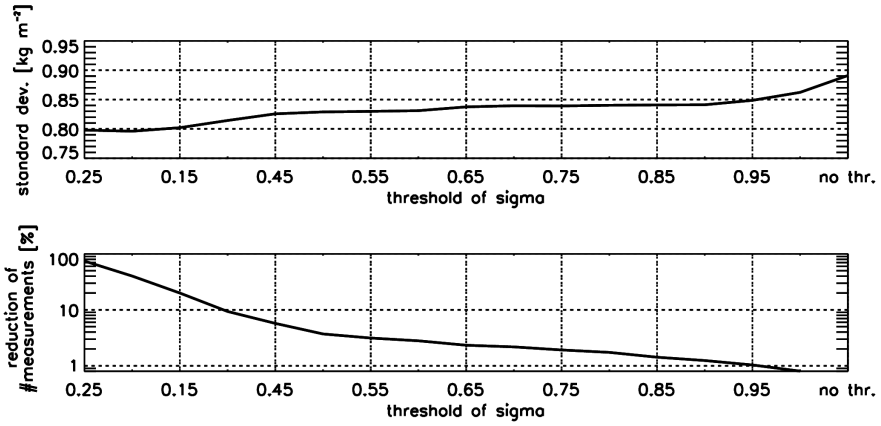

Figure 2.4: Standard deviation (top) of GPS measurements compared to microwave radiometer measurements and reduction of the number of measurements (bottom) if GPS data with σIWV higher than a distinct threshold is rejected. Measurements were carried out in April and May 2013 at JOYCE.

consistent within the investigated domain of central Europe. Less than 1% of the measurements are removed due to this criterion.

As described in Chapter 2.1.2, while processing ZTD, σZTD is computed which provides information on the accuracy of the delay. A rough estimate in terms of IWV is σIWV = 0.15 * σZTD. To test which threshold of σIWV is useful, a two month time series (April and May 2013) of GPS and simultaneous microwave radiometer measurements in Jülich is used. A previous study (Steinke et al., 2015) shows good agreement between measurements of both instruments except for very few samples especially during the first hour of the day, which is a known issue of the GPS near real-time retrieval (cf. Sect. 2.1.2). A filtering depending on different thresholds of σIWV shows a reduction in standard deviation between microwave radiometer and GPS measurements with lower thresholds for σIWV. It has to be mentioned that this quality check is not applied to the GPS measurements of the multi-instrument comparison (Sect. 4) since the development of this check is partly based on this study.

The threshold σIWV_{THR} is determined to be $0.85\,\text{kg}\,\text{m}^{-2}$ due to the following considerations. With this threshold the standard deviation is reduced from $0.89\,\text{kg}\,\text{m}^{-2}$ to $0.84\,\text{kg}\,\text{m}^{-2}$ (Fig. 2.4). Especially the GPS measurements with high differences up to $4\,\text{kg}\,\text{m}^{-2}$ compared to the microwave radiometer measurements are filtered out. Meanwhile, the reduction of the number of measurements is less than 1%. Lower thresholds do not distinctly reduce the standard deviation but reduce the number of measurements significantly. Therefore, the threshold $\sigma\text{IWV}_{THR} = 0.85\,\text{kg}\,\text{m}^{-2}$ is used for the whole data set.

2.2 MICROWAVE RADIOMETER

Microwave radiation is defined as radiation with frequencies between 3 and 300 GHz. A passive microwave radiometer (MWR) measures this radiation emitted by the atmosphere, i. e. gases and hydrometeors, at selected frequencies in this range. The range of frequencies (20–60 GHz is suited for deriving liquid water path, IWV, as well as temperature and humidity profiles. This is enabled through the distinct absorption characteristics of water vapour and oxygen within this frequency range, meaning an absorption line of water vapour at 22.235 GHz and an absorption band of oxygen at 60 GHz. The emission of both gases can be measured with a MWR. Furthermore, the emission of atmospheric liquid water increases with frequency. Typically, these measurements are calibrated directly to so-called brightness temperatures. For this purpose, the Rayleigh-Jeans approximation is normally used for microwave radiation. This approximation assumes a linear relation between spectral radiance and temperature. For very low temperatures occurring at frequencies lower than 40 GHz, this relationship no longer holds true and errors of some tenth degrees can occur (Janssen, 1993). Due to this, the relation between brightness temperature and spectral radiance is better described with Planck's function:

$$B_\nu(T) = \frac{2h\nu^3}{c^2} \frac{1}{e^{h\nu/k_B T} - 1}. \tag{2.8}$$

Here T is the temperature of a black body, which emits the spectral radiance B at frequency ν, h is the Planck's constant, c is the speed of light, and k_B is the Boltzmann's constant.

In principle, a MWR consists of an antenna, several amplifiers, and a detection system. The MWR Humidity and Temperature Profiler (HATPRO) manufactured by Radiometer Physics GmbH[1] has an antenna with a half power beam width of 3.5° for the water vapour sensitive channels. Thus, the MWR measures a comparatively narrow part of the atmosphere. The incident radiation is spilt with a wire grid in both orthogonal polarizations. This allows simultaneous processing by two receivers after amplification. One receiving unit measures at seven frequencies between 51.3 and 58.0 GHz along slope of the oxygen absorption complex, while the other unit receives the radiation at seven frequencies along the water vapour absorption line (22.24 GHz, 23.04 GHz, 23.84 GHz, 25.44 GHz, 26.24 GHz, 27.84 GHz) and one frequency in an atmospheric window (31.40 GHz). From the brightness temperatures of the latter seven frequencies, the IWV, the integrated liquid water content and a vertically coarse resolved water vapour profile with up to three independent layers (Löhnert et al., 2009) can be derived. With a low noise level of approximately 0.05 K

1 http://www.radiometer-physics.de

in the measured brightness temperatures, HATPRO is able to detect small variations in atmospheric water vapour.

IWV is derived following a statistical approach based on a least squares linear regression model (Löhnert and Crewell, 2003) from the multi-frequency brightness temperatures **TB** assuming the error characteristics mentioned above. Its general form can be written as

$$IWV = c_0 + \mathbf{c}_1 \cdot \mathbf{TB} + \mathbf{c}_2 \cdot \mathbf{TB}^2. \tag{2.9}$$

To derive the coefficients c_0, $\mathbf{c}_1$, and $\mathbf{c}_2$, a training data set is used. This data set consists of more than 13 000 non-precipitating radiosoundings at De Bilt, Netherlands, which is about 150 km apart from JOYCE. With this algorithm, IWV can be derived with a random error of approximately 0.5–0.8 $\mathrm{kg\,m^{-2}}$ from zenith measurements (Maschwitz et al., 2013). The systematic error is assumed to be 0.5 $\mathrm{kg\,m^{-2}}$ and the noise level is 0.05 $\mathrm{kg\,m^{-2}}$. Note that the MWR is able to measure automatically with a temporal resolution of ca. 2 s under all weather conditions with the exception of when the radome is wet. In these cases, no IWV values are provided based on visual inspection.

2.3 RADIOSONDES

Attached to a balloon, instruments can ascent through the atmosphere. In combination with a GPS sensor, which determines the position of the sonde, the instruments measure profiles of pressure, temperature and humidity. Additionally, profiles of wind speed and wind direction are derived from the movement of the sonde.

The radiosoundings used in this study are performed with Graw DFM-09 sondes[2]. These feature a thin film capacitance sensor in order to measure relative humidity. Together with the temperature measurements and the pressure profile derived from GPS measurements, the absolute humidity is computed. Afterwards, the absolute humidity is integrated to derive IWV from the radiosoundings.

Several studies asses the error of radiosonde measurements showing that the error strongly depends on the type of radiosonde. Furthermore, the systematic and random error of the relative humidity sensor depend on temperature and differ between day- and nighttime. A World Meteorological Organization (WMO) comparison (Nash et al., 2011) to IWV derived from GPS showed that the difference between Graw DFM-09 and GPS is 2 $\mathrm{kg\,m^{-2}}$ higher during daytime than during nighttime. Other radiosonde types showed the opposite behaviour. The reason for this could be that the correction algorithm applied by the Graw software probably overcorrects the original dry bias. It is not known if the correction of the software was changed since the test. In general, IWV comparisons of radiosondes with ca-

2 http://www.graw.de

pacitance sensors to GPS measurements show a dry bias for the radiosondes of approximately 1.2 kg m^{-2} during daytime due to sensor exposition to solar radiation (Wang and Zhang, 2008).

An additional error source is the drift of radiosondes during ascent. The radiosondes used in this study drift horizontally on average 5 km during their ascent to 850 hPa and 39 km to the 200 hPa-layer. The maximum drifts to these pressure levels are 8 km and 106 km, respectively. Therefore, it has to be kept in mind that a radiosonde may well sample a different air mass than a zenith-pointing ground-based instrument would do. However, IWV variability is low above the boundary layer because the flow is determined by large-scale advection and therefore homogeneity is high (Shao et al., 2013).

2.4 SUNPHOTOMETER

The sunphotometer (CE 318 N-EBS9, Cimel Eletronique S.A.S[3]) used in this study measures the extinction of direct solar irradiance and sky radiance at 9 wavelengths (340 , 380 , 440 , 500 , 675 , 870 , 937 , 1020 , and 1640 nm) fully automatically. Allowing for the extinction due to aerosols, the extinction due to the amount of water vapour in the line of sight to the sun T_w can be derived from the extinction at 937 nm. The extinction can be described with the following equation

$$T_w = \exp[-a(m \cdot IWV)^b] \tag{2.10}$$

where a, and b are constants, and m is the relative optical air mass (Schmid et al., 2001). From this relationship, IWV can be derived with an accuracy of 10% (Alexandrov et al., 2009).

The sunphotometer is part of Aerosol Robotic Network (AERONET), meaning that data processing is performed by the National Aeronautics and Space Administration (NASA) (Dubovik et al., 2006). The data used within the present study is of quality level 1.0 and has a temporal resolution of approximately 10 min.

Since the sunphotometer measures the direct sunlight, its IWV retrieval is limited to daytime and clear-sky conditions. Additionally, since the instrument tracks the sun, the retrieved IWV is not zenith viewing, but along a slant path through the atmosphere. This implies that it samples a different atmospheric volume than zenith-pointing instruments. An additional problem due to the changing viewing paths can occur when the sunphotometer is measuring at low solar zenith angles in combination with high IWV values. This saturation could lead to transmission approaching zero (Ingold et al., 2000).

3 http://www.cimel.fr

2.5 MODIS

The Moderate Resolution Imaging Spectroradiometer (MODIS) is a space-borne, passive, whisk-broom scanning radiometer which measures the radiation backscattered and emitted from Earth, clouds, and atmosphere at 36 spectral bands between 0.4 and 14.4 µm wavelength. Two MODIS instruments are currently operational in space on board of NASA's sun-synchronous near-polar-orbiting Earth Observing System (EOS) Terra and Aqua platforms[4]. This enables a full global coverage every one to two days. With an orbit height of approximately 705 km and a scanning pattern of $\pm 55\,^{\circ}$, the swath dimension of MODIS amounts to 2330 km across-track and 10 km along-track (at nadir).

Two standard IWV products exist for MODIS: the infrared retrieval (MODIS-IR) and the near-infrared retrieval (MODIS-NIR). Within the present study, MODIS Level 2 MODIS-IR and MODIS-NIR products from Collection 5.1 are used, which have a grid resolution of 3 and 1 km, respectively[5].

MODIS-NIR utilizes three channels located within the water vapour absorption wavelengths, namely 0.905 µm, 0.936 µm and 0.94 µm, and two non-absorbing channels, namely 0.865 µm and 1.24 µm. The ratios in reflected NIR radiation from water vapour absorption channels to window channels give the atmospheric water vapour transmittances. From these, IWV is obtained from look-up tables based on line-by-line calculations. Note that single and multiple scattering effects are assumed to be negligible. The estimated errors in retrieved IWV are typically 5–10% and are mostly assigned to uncertainties in the spectral reflectance of the surface targets and in uncertainties in the amount of haze over dark surfaces. For details on the MODIS-NIR retrieval see Gao and Kaufman (2003).

MODIS-IR utilizes two water vapour absorption bands which deliver information on the moisture distribution and three window bands which also have weak water vapour absorption. From the radiances measured at these bands, water vapour profiles are retrieved via a statistical regression algorithm based on previously determined relationships between radiances and water vapour profiles. Though computationally efficient, this algorithm is sometimes non-physical. Therefore, a non-linear iterative physical algorithm is applied to the retrieved profiles, aiming to improve the solution, that is reduce the known overestimation of IWV. For details on the MODIS-IR retrieval see Seemann et al. (2003).

Being based on thermal radiation, MODIS-IR is available for both day- and nighttime over ocean and land. However, it is limited to clear-sky situations. The same goes for MODIS-NIR, which is ad-

4 http://modis.gsfc.nasa.gov/

5 http://modis.gsfc.nasa.gov/data/

ditionally restricted to daytime and highly reflective surfaces that means land and no ocean. Both MODIS retrievals, if applied to overcast scenes, miss information from within and below clouds.

3 MODELS

Additionally to the observations, runs of different models are used to address the spatio-temporal variability of IWV. Reanalyses, as the COSMO reanalyses (cf. Chap. 3.1) and ERA-Interim (cf. Chap. 3.2), merge observations and modelling for best estimates of atmospheric state over a time period of several years. Hence, a reanalysis is neither pure observation nor pure model. However, to distinguish it from pure observations we use the notation model as it provides gridded, three dimensional, temporally continuous information. The advantages of a reanalyses in comparison to an operational model are first the usage of one model version for a longer time period and therefore no inconsistency in the simulation due to a change in the model version, and second observations which become available too late for operational usage can be assimilated. The novel model ICON (cf. Chap. 3.3), which is run in a LES configuration (Heinze et al., 2016) provides a highly resolved simulation over Germany. In the following, a description of these models and their specific output is given.

3.1 COSMO REANALYSES

Within the Hans-Ertel-Zentrum für Wetterforschung (HErZ; Weissmann et al. 2014, Simmer et al. 2015), two regional reanalyses are produced: COSMO-REA6 (Bollmeyer et al., 2015) and COSMO-REA2 (Wahl et al., 2016), with a resolution of ca. 6 km and 2 km, respectively. In the following, the Consortium for Small-scale Modelling (COSMO) and the special reanalyses framework is introduced.

The limited-area, numerical weather prediction (NWP) model COSMO[1] is a non-hydrostatic, fully compressible model of the atmosphere. The thermo-hydrodynamical equations describing compressible flow in a moist atmosphere are solved using a finite-difference method on an Arakawa-C grid (Arakawa and Lamb, 1977). As for the coordinates, the model uses rotated latitude/longitude coordinates in the horizontal and time-independent terrain-following coordinates in the vertical. COSMO uses a bulk-water continuity model for the grid-scale precipitation (Doms et al., 2011) and a Tiedtke mass flux scheme for subgrid-scale convection (Tiedtke, 1989). The radiative transfer scheme used in COSMO is described in Ritter and Geleyn (1992).

Both reanalyses, COSMO-REA6 and COSMO-REA2, are simulated with COSMO. The domain of COSMO-REA6 is the CORDEX-EURO-

1 http://www.cosmo-model.org/

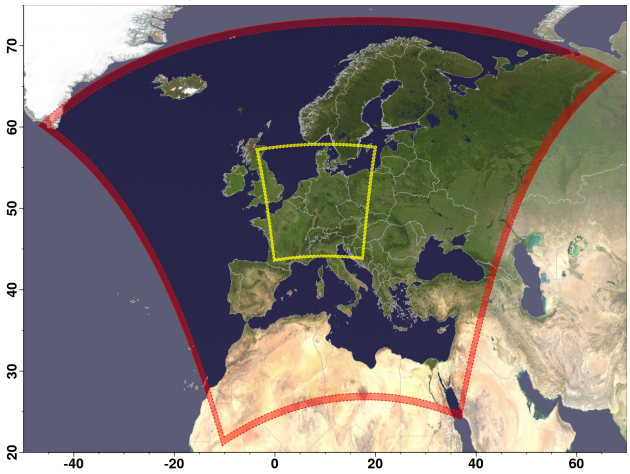

Figure 3.1: Domain of COSMO-REA6 (red) and COSMO-REA2 (yellow). (Source: Bollmeyer et al. (2015))

11 domain, which covers Europe (Fig. 3.1). However, the used grid is finer than the original CORDEX-EURO-11 grid, i. e. 40 vertical layers and a horizontal grid spacing of 0.055°, which corresponds to approximately 6.2 km. The time step of the model is 50 s. The setup of the reanalysis, which uses COSMO version 4.25 (28 September 2012), is generally the same as the setup of COSMO-EU (Steppeler et al., 2003), which was run operationally by DWD until 30 November 2016. The initial field is provided at 00:00 UTC at the start date. From this field, a 6 hours run with a full data assimilation is initiated. After six hours, a snow analysis is performed and a new 6 hours run is started. This lasts until the end of the day. Then a sea surface temperature analysis is performed, followed by a snow analysis and a soil moisture analysis. Then the next day is started and so on until the end of the simulation period is accomplished. The initial field and boundary conditions originate from ERA-Interim (Chap. 3.2).

The COSMO-REA6 run provides initial fields and boundary conditions for COSMO-REA2, which has a finer resolution, i. e. a horizontal grid spacing of 0.018° corresponding to 2 km, 50 vertical levels, and a time step of 18 s. This reanalysis, covering Germany and also parts of its neighbouring countries (Fig. 3.1), uses COSMO version 5.00.2 (21 February 2014). COSMO-REA2 is produced in the same way as described above for COSMO-REA6, with respect to the snow and sea surface temperature analysis, but without soil moisture analysis. Its setup basically corresponds to the setup of the operational COSMO-DE (Baldauf et al., 2011) by Deutscher Wetterdienst (DWD), except for the setting of the latent heat nudging (LHN) which is used to assimilate weather radar measurements. The operational LHN-coefficient of 1.0 disturbs the stability of the model too much resulting in unrealistic cloud structures. Therefore, a reduced LHN-coefficient

of 0.25 is used in the reanalysis, which leads to good results without the drawbacks of the operational constant. The observations assimilated in both COSMO-REA2 and COSMO-REA6 are: measurements from radiosoundings, aicrafts, SYNOP stations, ships and drift buoys but no satellite measurements.

The output of both reanalyses is stored every 15 min for two dimensional variables and every hour for three dimensional variables. While the COSMO-REA2 is available for the years 2007–2013, COSMO-REA6 begins in 1995 and is updated continuously. Due to technical problems, there is a loss of COSMO-REA2 data, which sum up to less than 12 days.

3.2 ERA-INTERIM

At European Centre for Medium-range Weather Forecasting (ECMWF) the ECMWF Re-Analysis Interim (ERA-Interim) is produced since 1979 and is continuously updated (Dee et al., 2011). ERA-Interim is performed on the spectral grid T255, which corresponds to a grid size of approximately 80 km on 60 vertical levels from the surface up to 0.1 hPa. Several in-situ measurements, surface observations from land, ships, and drifting buoys, are assimilated as well as profile information from radiosondes, pilot balloons, dropsondes, wind profiler and aircraft measurements. The majority of assimilated measurements originates from satellites: clear-sky radiance measurements from polar-orbiting and geostationary sounders and imagers, atmospheric motion vectors derived from geostationary satellites, scatterometer wind data, and ozone retrievals from various satellite-borne sensors. Additionally, IWV from GPS radio occultation is used for assimilation with the 1D+4D-Var scheme.

Every 6 hours a reanalysis is produced. Additionally, at 00:00 UTC and 12:00 UTC forecast runs with a 3-hourly output are performed. For reasons of continuity, both the analysis and the forecasts are used for the initialization of COSMO-REA6 as well as for the evaluation in this study.

3.3 ICON

The ICOsahedral Non-hydrostatic (ICON) modelling framework described by (Zängl et al., 2014) is developed jointly by DWD and Max Planck Institute for Meteorology (MPI-M) as the next generation NWP and climate model. The dynamical core is formulated on an icosahedral-triangular Arakawa C grid (Arakawa and Lamb, 1977). Within the HD(CP)^2 project, ICON is extended to perform high-resolution regional simulations (Heinze et al., 2016). For this, ICON is run with LES physics: a 3D Smagorinsky turbulence scheme, and two-moment microphysics, while parametrization of convection,

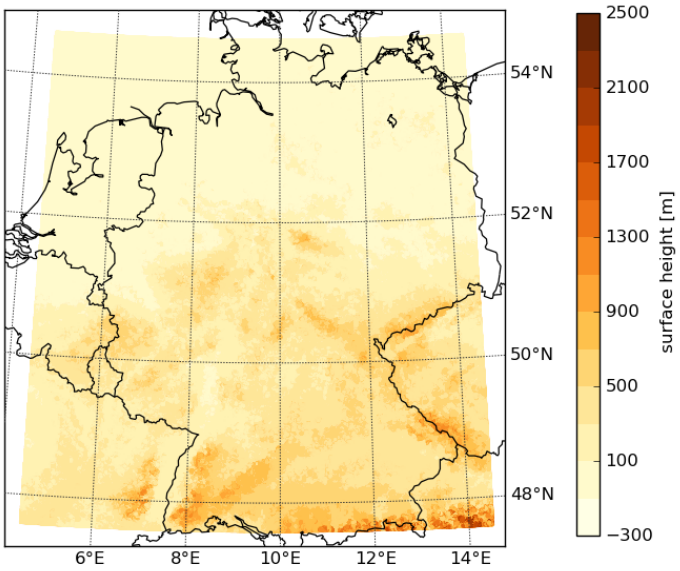

Figure 3.2: Domain of ICON with a resolution of 156 m and its surface height AMSL.

Smagorinsky orography and Smagorinsky gravity wave drag is turned of. A one-way nesting with three domains with resolutions of 624 m, 312 m, and finally 156 m is performed. The domain covers Germany nearly completely and some neighbouring countries partly (Fig. 3.2). 150 generalized terrain-following levels are used in the vertical with reduced level spacings in the lower troposphere. The simulation is initialized each day at 00:00 UTC and nudged hourly on the lateral boundaries with COSMO-DE analysis and forecasts.

Part II

RESULTS

4

MULTI-INSTRUMENT COMPARISON

Before investigating the variability of IWV the quality of the observations needs to be thoroughly assessed. A wide range of measurement techniques exists for the observation of IWV. These instruments can measure under different atmospheric conditions, and have different error characteristics. The instruments used in this thesis are described in the following with their advantages and disadvantages. Given the particular importance of IWV, many studies attempt to intercompare the various measurement techniques. Those studies differ, on the one hand in their framework — that is the combination of instruments, the location of these with respect to each other, the considered time frame, the geographical region and therefore the IWV regime — and on the other hand in their evaluation technique — that is the averaging periods, the temporal matching criteria, and the application of corrections due to vertical and horizontal distance of the instruments to each other.

Since the water vapour column needs to be considered over the same altitude range, the height of the instruments is of particular importance for the observation of IWV. Therefore, corrections are necessary (cf. Böhme et al., 2011; Buehler et al., 2012). Several studies exists with comparisons of various IWV observations in different geographical regions and for different time periods. They use different criteria for temporal and spatial matching and elevation corrections (cf. Bennouna et al., 2013; Martin et al., 2006; Morland et al., 2009; Pałm et al., 2010; Schneider et al., 2010; Torres et al., 2010). Frequently, these comparisons involve data sets with more than 1 h temporal and more than 20 km spatial difference or they do not match the measurements but use statistics with different temporal sampling for their comparisons (cf. Bennouna et al., 2013; Morland et al., 2009).

The following intercomparison avoids/reduces most of the matching problems since all ground-based instruments are within a range of 4 km and only measurements with in the same 15 min time interval are compared (cf. Sect. 4.1). The two months of HOPE (April and May 2013) provide the opportunity to investigate IWV characteristics over a wide range of atmospheric conditions for a typical continental, mid-latitude site. During HOPE the instrument set of the JOYCE at the Forschungszentrum Jülich (FZJ) — MWR, GPS, sunphotometer — was complemented with frequent radiosoundings (Löhnert et al., 2015). Additionally, coincident MODIS infrared and near infrared observations are included in the intercomparison.

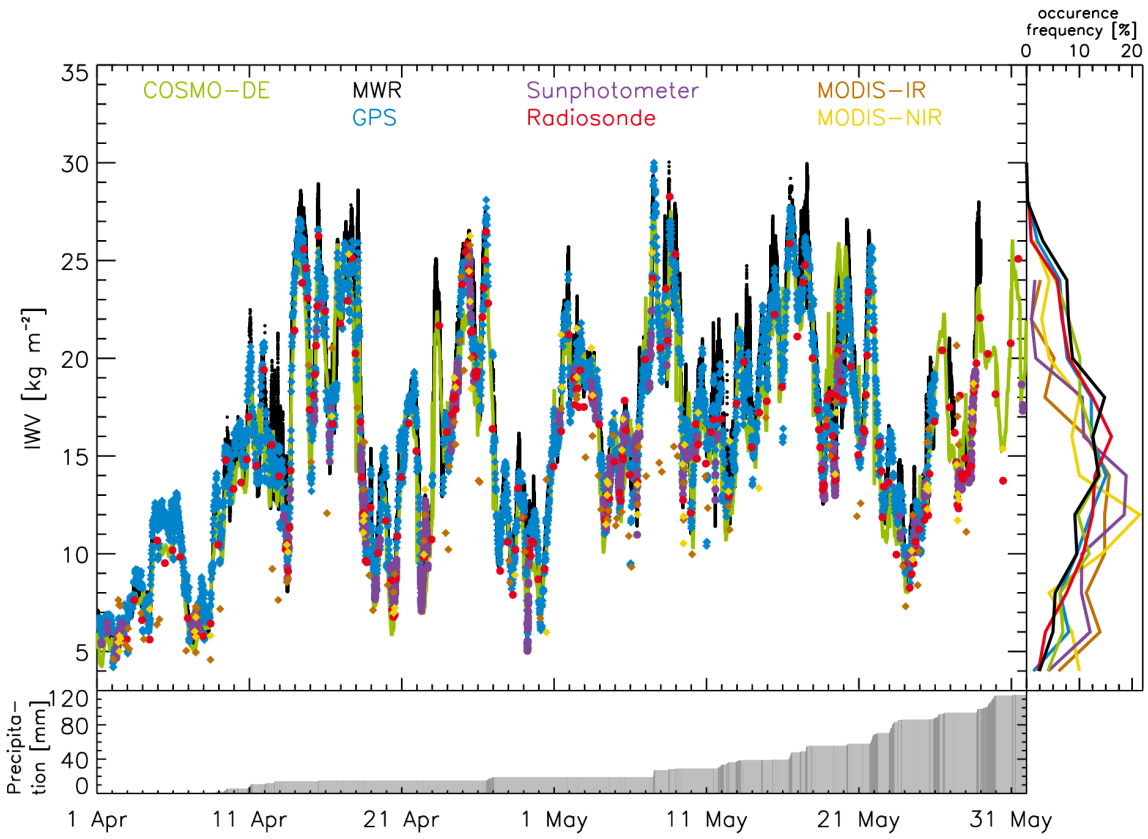

Figure 4.1: Time series of IWV during HOPE. Displayed are: MWR (black), GPS (blue), sunphotometer (purple), radiosoundings (red), MODIS-IR (orange), MODIS-NIR (yellow), and COSMO-DE (light green). The frequencies of occurrence of IWV are displayed in the right panel with corresponding colours. Accumulated precipitation is shaded in grey in the lower panel; dark grey bars indicate the time when precipitation fell. (published in Steinke et al. (2015))

The period of HOPE was characterized by dry polar air masses at the beginning of April that transitioned into a strong synoptically forced regime in mid April with frequent passages of frontal systems over JOYCE during May. There were only a few rain events in April, with total precipitation less than the long-term average, but more in May, even slightly more than the long-term average. Precipitation of the two months accumulate to 115 mm (cf. bottom panel in Fig. 4.1). This is only slightly lower than the long-term average for the two months (120 mm).

In this period, IWV varies by 25 kg m^{-2}, namely between 5 and 30 kg m^{-2} (cf. main panel in Fig. 4.1). IWV can increase or decrease by 10–20 kg m^{-2} within one to two days when the passage of frontal systems lead to fast exchange of air masses. This makes the data set well suitable to evaluate the performance of the instruments for a variety of conditions.

The different IWV data sets reveal a broad frequency distribution with a maximum around 15 kg m^{-2} (cf. right panel in Fig. 4.1). The difference in the distribution reveals the influence of the instrument sampling: GPS, MWR, radiosondes, and COSMO-DE show rather similar characteristics. In contrast, the distribution for the sunphotometer is shifted to lower IWV values as it is restricted to daytime, clear-sky measurements.

The following intercomparison is published in the recent study by Steinke et al. (2015). First, it is described how data is temporally and spatially matched. Afterwards, the instrument performance during the whole period of HOPE is assessed.

4.1 MATCHING THE DATA

In the following, first, the spatial matching of all data sets is addressed, and second, the temporal matching is considered. All JOYCE instruments are located within a distance of 110 m to each other. GPS receiver and sunphotometer are situated on the same roof of a building at a height of 111 m AMSL while the MWR is located on the ground. The height difference to the instruments on the roof is 21 m and therefore the MWR IWV needs to be corrected. For this, the 120 m meteorological tower nearby is used to adjust the IWV of the MWR to the level of GPS and sunphotometer from the water vapour density measured in heights of 2 m, 10 m, and 20 m above ground. The amount of water vapour subtracted from the MWR measurements is 0.3 kg m^{-2} at its maximum.

The location of the radiosonde launches is at exactly the same height as JOYCE at a distance of 3.9 km to the south-east. For MODIS, the horizontal and height distance to JOYCE varies with satellite track. The topography of the MODIS measurements is taken from the Consultative Group on International Agricultural Research-Consortium for Spatial Information Shuttle Radar Topography Mission (CGIAR-CSI SRTM) 90 m database[1]. The topography of the nine nearest CGIAR-CSI SRTM pixels is averaged to retrieve the height of the MODIS pixel. The nearest MODIS pixel within a distance of less than 7 km and a height difference of less than 100 m is used. To correct for the height difference, again the water vapour density of the meteorological tower is used resulting in a maximum correction of 1.5 kg m^{-2}.

Apart from the spatial differences, the temporal differences need to be considered. Each GPS measurement originally represents a time period of 15 min. MWR and sunphotometer measurements are averaged over 15 min. IWV from the other measurements is available only with a coarser temporal resolution. MODIS measurements are

1 http://srtm.csi.cgiar.org

matched to the corresponding 15 min period. The ascent of a radiosonde takes approximately 1 h. Since the largest amount of water vapour is in the lower atmosphere, the radiosoundings are matched to the 15 min interval, during which they are started. This results in a maximum time difference of less than 15 min between two individual measurements of different instruments.

Furthermore, it has to be mentioned that the quality check of the GPS measurements described in Sect. 2.1.3.2 is not applied to the measurements used in this instrument comparison since it was developed afterwards based on the results of this intercomparison.

4.2 INSTRUMENT INTERCOMPARISON DURING HOPE

Since none of the instruments can be considered as "the truth", every instrument is compared to all other instruments (cf. Fig. 4.2). All measurements are considered at 15 min resolution either with 15 min averages or assignment to a 15 min time interval (cf. Sect. 4.1). For the following comparison, it has to be acknowledged that the maximum distance between instruments is 110 m except for the respective MODIS pixels, which are in a distance of up to 7 km and radiosondes, which are started in a distance of approximately 4 km and can drift up to 8 km on their ascent up to 850 hPa (cf. Sect. 2.3).

For the MODIS – radiosondes comparison, too few coincident measurements are available due to the infrequent satellite overflights. Excluding MODIS, the overall agreement between the instrument pairs is good. The standard deviation is not higher than $1\,\mathrm{kg\,m^{-2}}$ and the correlation coefficient is never lower than 0.98. The absolute bias varies from $0\,\mathrm{kg\,m^{-2}}$ for GPS – sunphotometer to $1\,\mathrm{kg\,m^{-2}}$ for radiosondes – MWR. In the following, the individual instrument comparisons are examined in more detail.

With more than 3800 measurements, the GPS – MWR comparison includes the most cases as both instruments also measure during cloudy conditions. The bias ($0.2\,\mathrm{kg\,m^{-2}}$) is very low and the standard deviation ($0.9\,\mathrm{kg\,m^{-2}}$) is within the expected measurement uncertainty (cf. Table 2.1). Larger opposite biases ((-0.5) –$(-0.6)\,\mathrm{kg\,m^{-2}}$) and slightly smaller standard deviations ($0.7\,\mathrm{kg\,m^{-2}}$) are found by Martin et al. (2006). One of the differences between the two observation techniques is the measurement geometry. While MWR is zenith-pointing with a half power beam width of 3.5°, the observations of GPS comprises measurements along paths as low as 7° elevation angle. Deng et al. (2011) compared slant integrated water vapour at 90° of GPS to IWV measurements with a MWR and found a standard deviation of $1.3\,\mathrm{kg\,m^{-2}}$, which is even larger. However, the technique of deriving slant integrated water vapour differs from the technique used to derive IWV for the data set in this study.

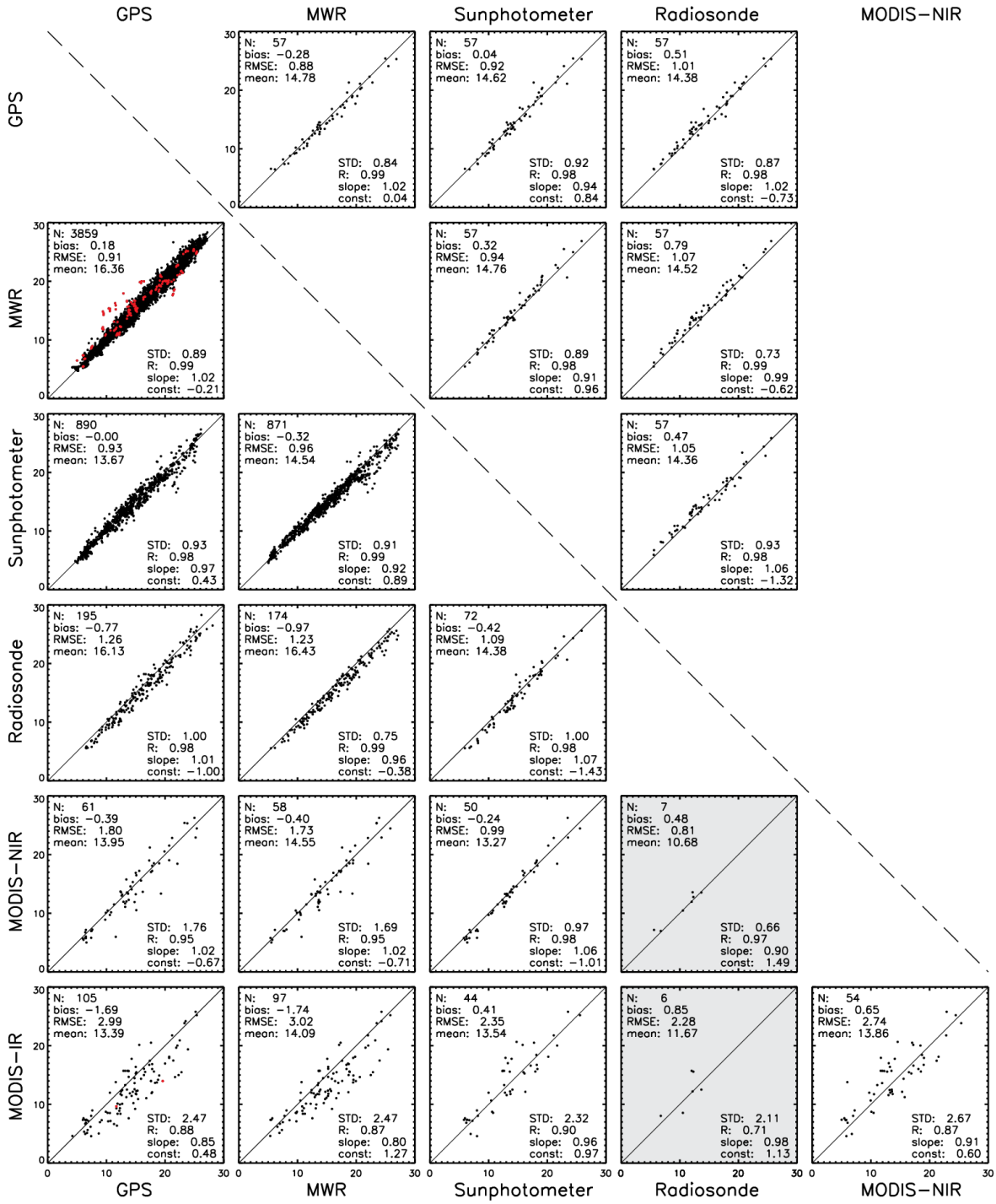

Figure 4.2: Scatterplots of IWV for all instruments against each other. Included are the number of measurements (N), bias (row - column in $\mathrm{kg\,m^{-2}}$), root mean square error (RMSE in $\mathrm{kg\,m^{-2}}$), mean (in $\mathrm{kg\,m^{-2}}$), standard deviation (STD in $\mathrm{kg\,m^{-2}}$), Pearson correlation coefficient (R), and slope and y-intercept (const in $\mathrm{kg\,m^{-2}}$) of linear regression. The lower left half of the figure shows comparisons when the two coincident measurements exist. The upper right half shows comparisons when observations of all instruments are available. MODIS is not included in the upper half due to less measurements. The GPS measurements between 0 and 1 UTC are highlighted in red. (published in Steinke et al. (2015))

Despite the small standard deviation, there are some GPS IWV values which are up to $5\,\mathrm{kg\,m^{-2}}$ lower than observed by the MWR (cf. Fig. 4.2). These differences occur due to problems in the processing of the NRT GPS data at the beginning of the day, as mentioned in Sect. 2.1.2. Excluding the first hour of the day leads to a reduction of the bias to $0.1\,\mathrm{kg\,m^{-2}}$ and of the standard deviation to $0.8\,\mathrm{kg\,m^{-2}}$. Furthermore, a small dependency of the error on the IWV is found. For large IWV values the difference GPS - MWR tends to be smaller than for small IWV values. Other dependencies, such as the influence of wind direction, spatial IWV gradient, temporal IWV variability, liquid water path, and spatial distribution of GPS slants, which are used to retrieve the IWV, are tested but no significant dependency is found (not shown).

On average, the radiosondes are $0.8\,\mathrm{kg\,m^{-2}}$ ($1.0\,\mathrm{kg\,m^{-2}}$) drier than GPS (MWR). However, only a small difference of $0.2\,\mathrm{kg\,m^{-2}}$ between day and night time soundings could be identified probably due to the correction within the Graw software (cf. Sect. 2.3). Previous studies exhibit even higher biases of 1–$2\,\mathrm{kg\,m^{-2}}$ (e. g. Bokoye et al., 2003; Martin et al., 2006).

The comparisons MODIS – GPS and MODIS – MWR show that IWV measurements from both MODIS-IR and MODIS-NIR are frequently too low. However, these MODIS measurements are not included in the MODIS – sunphotometer comparisons, since there are no sunphotometer measurements at these times. The reason for this is probably that cloudy cases are not reliably detected by the MODIS cloud detection algorithm. Clouds lead to a lower IWV because the amount of IWV below and inside the cloud is not detected by MODIS. A clear difference can be seen in the standard deviation in the comparisons involving MODIS-NIR and MODIS-IR: the latter has more than double the standard deviation of the first, which could be due to the coarser resolution but also due to poorer physical constraints in the algorithm.

Since each instrument intercomparison is carried out during different atmospheric conditions (a consequence of the varying instrument limitations), the mean IWV of the measurements included in each comparison differs by approximately $3\,\mathrm{kg\,m^{-2}}$. To allow for a better comparison of the errors of different instrument combinations, 57 simultaneous measurements of all instruments with the exception of MODIS are also investigated separately. The mean of these comparison then only differs by $0.4\,\mathrm{kg\,m^{-2}}$ (cf. Fig. 4.2) and the standard deviation is reduced for all instrument combinations to be lower than $1\,\mathrm{kg\,m^{-2}}$. This results likely from sampling more conditions which are more similar to each other. By including only measurements when the sunphotometer is measuring, night time measurements and most importantly all rainy cases and cases with clouds in the direction of the sun are excluded.

4.3 SUMMARY AND CONCLUSIONS

The different instruments have different sampling characteristics, uncertainties and limitations (cf. Table 2.1) that are important to consider when assessing IWV variability. Most importantly a height correction is necessary as an elevation difference of only 20 (100) m can introduce errors of 0.3 (1.5) $\mathrm{kg\,m^{-2}}$. Pairwise comparison of the instruments with 15 min temporal resolution shows a generally good agreement over the whole HOPE period with a small standard deviation ($\leq$1$\mathrm{kg\,m^{-2}}$) and a high correlation coefficient ($\geq$ 0.98), with the exception of MODIS. The absolute bias varies from 0 to 0.97 $\mathrm{kg\,m^{-2}}$. IWV from MODIS is often lower than from the other instruments because cloud pixels are most probably not always identified by the MODIS cloud detection algorithm. Nevertheless, MODIS is the only instrument capable of assessing the spatial structure of IWV – once corrected for elevation and filtered for clouds – over the whole globe.

As expected, a reduction of the compared data sets by only including coincident measurements simultaneously excluding all night time, rainy and cloudy cases, leads to an improvement in the overall agreement. However, the mean values over the HOPE period range from around 16 $\mathrm{kg\,m^{-2}}$ (GPS, MWR) to lower than 14 $\mathrm{kg\,m^{-2}}$ (sunphotometer, MODIS). This difference, which is distinctly higher than the bias of most of the instrument comparisons, implies significant errors when climatologies are constructed from data sets with a poor sampling.

The multi-instrument intercomparison reveals a number of peculiarities of the individual instruments. Sunphotometer measurements show a good agreement with the other measurements but can only be conducted during clear-sky at daytime and seem to suffer from problems when the sun is low. IWV from MWR and GPS slightly varies (bias: 0.2 $\mathrm{kg\,m^{-2}}$ (1%), standard deviation: 0.9 $\mathrm{kg\,m^{-2}}$ (6%), cf. Fig. 4.2) taking the specified instrument uncertainties into account. However, the near-real time processed GPS data exhibit inconsistencies at the beginning of each day and each hour due to the processing procedure that might also lead to a shift in the diurnal cycle of IWV. Further work on the processing might increase the performance of the GPS measurements. In contrast to MWR, a comprehensive GPS networks exist, thus making GPS better suited to evaluate models over their whole domain.

5 IWV UNCERTAINTIES IN MODEL SIMULATIONS

Before model simulations are used for the investigation of IWV variability the simulated IWV products needs to be thoroughly assessed. The question arises to which degree the COSMO reanalyses, ERA-Interim and ICON can reproduce IWV and its variability. Therefore, the employed models are evaluated with measurements of the German-wide GPS network, which is chosen for evaluation based on the results of the instrument intercomparison (Chap. 4).

5.1 EVALUATION OF REANALYSES WITH GPS MEASUREMENTS

To aim at the question to which degree the COSMO reanalyses and ERA-Interim can reproduce IWV and its variability and which advantage high resolution shows an evaluation with observations is needed. Since GPS measurements showed a good performance in the instrument intercomparison during HOPE and these measurements are available for many stations in Germany with a high temporal resolution of 15 minutes during all weather conditions, these independent measurements are used for the evaluation of the reanalyses. Therefore, measurements of GPS stations are compared to the nearest reanalyses gridpoint. Since GPS stations are not necessarily on the same height level as the surface height of the corresponding model gridpoint, IWV of the reanalyses is increased or decreased according to the height difference, as is done for the multi-instrument comparison (Sect. 4.1). To restrict the uncertainty due to this correction, only stations with an absolute height difference smaller than 200 m are included in the analysis. In the following, the COSMO reanalyses are evaluated with GPS observations and compared to a dynamical downscaling of COSMO (COSMO-DS) and ERA-Interim.

5.1.1 *Why a dynamical downscaling of COSMO is not good enough?*

A dynamical downscaling is an established method to project large-scale simulations on smaller, regional scales. This technique uses the large-scale simulations as initial state and boundary forcing for a regional model with a finer grid. With this approach, spatially enhanced data sets can be generated from global reanalyses. However, since the spatially highly resolved simulations depend on the deduction of small scale details from coarsely resolved initial and boundary conditions, dynamical downscaling systems are always subject to errors. The dynamical downscaling with COSMO used in this study

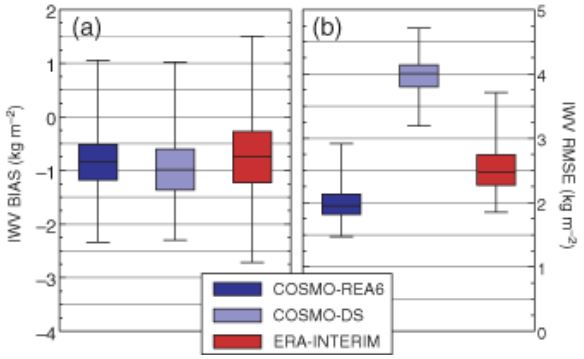

Figure 5.1: Quartiles of errors of IWV at 157 GPS stations: Bias ($IWV_{modelled}$–$IWV_{measured}$) and RMSE for simulations with COSMO-REA6, COSMO-DS, and ERA-Interim against GPS observations. (published in Bollmeyer et al. (2015))

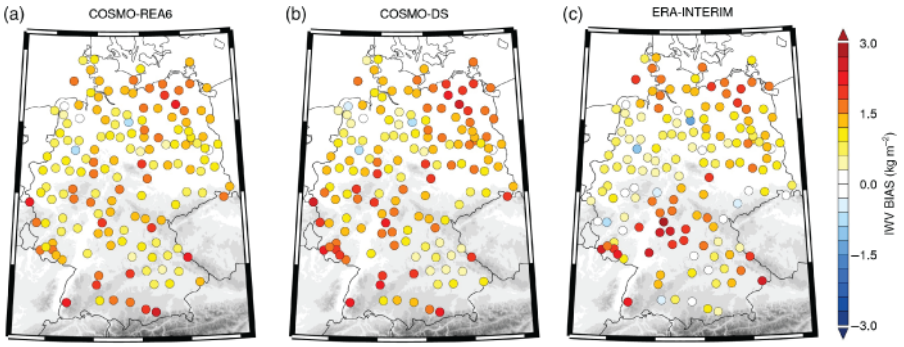

Figure 5.2: Bias of IWV ($IWV_{modelled}$–$IWV_{measured}$) of simulations with COSMO-REA6 (a), COSMO-DS (b), and ERA-Interim (c) against observations at 157 GPS stations. The background is shaded according to orography. (published in Bollmeyer et al. (2015))

is initialised with the state of the full reanalysis at 00:00 UTC on 1 January 2011 and runs freely for the year 2011 without any data assimilation but using the boundary fields of ERA-Interim. Due to the lack of data assimilation, a dynamical downscaling is more simple and less costly than a full reanalysis as the COSMO reanalysis.

To show the advantages concerning IWV from a full reanalysis, a comparison for the year 2011 of a COSMO downscaling from ERA-Interim with the full reanalysis COSMO-REA6 is carried out. This comparison is already published in Bollmeyer et al. (2015). Since the 3-hourly ERA-Interim output has the coarsest temporal resolution, IWV is compared only every 3 h. It has to be mentioned that the quality check of the GPS observations used for this comparison is not as advanced as described in Sect. 2.1.3 but consists of visual inspection only.

On average, all model simulations are drier than the measurements (Fig. 5.1). The absolute value of the mean bias over all stations is

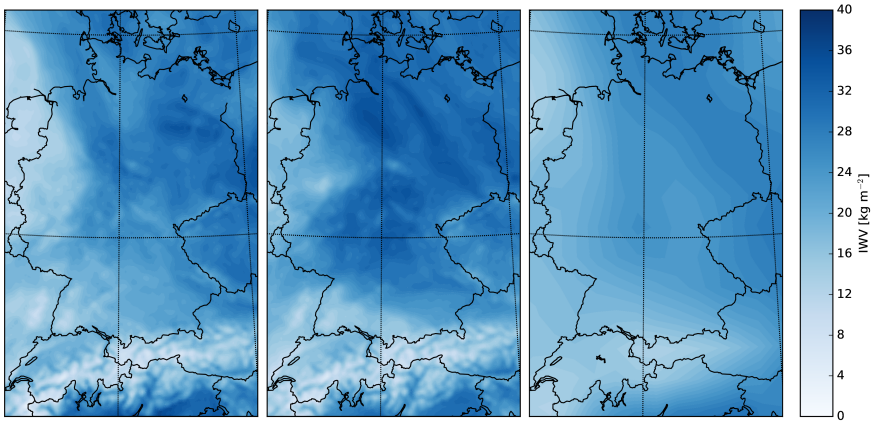

Figure 5.3: Maps of IWV from COSMO-REA6 (left), COSMO-DS (middle), and ERA-Interim (right) for 1 August 2011 00:00 UTC.

slightly smaller for ERA-Interim $-0.7\,\mathrm{kg\,m^{-2}}$ than for COSMO-REA6 ($-0.8\,\mathrm{kg\,m^{-2}}$) and COSMO-DS ($-0.9\,\mathrm{kg\,m^{-2}}$). However, the differences between the models are very small compared to the large spatial variation of the bias within the domain (Fig. 5.2). More importantly, the high-resolution reanalyses show a smaller variation of the bias as expressed by their quartiles and the average RMSE of COSMO-REA6 ($2.0\,\mathrm{kg\,m^{-2}}$) is the smallest of all three datasets (Fig. 5.1). While ERA-Interim exhibits a slightly larger RMSE of $2.5\,\mathrm{kg\,m^{-2}}$, the RMSE for COSMO-DS is twice as large ($4\,\mathrm{kg\,m^{-2}}$).

The IWV fields in COSMO-DS and COSMO-REA6 show small-scale structures, whereas ERA-Interim cannot represent such features which is caused by its coarser resolution (Fig. 5.3). Comparing the small-scale structures of COSMO-DS to those of COSMO-REA6, differences can be found which originate from the lack of a data assimilation process leading to a shift in time and/or space of the structures in the water vapour fields. Here it is not investigated what kind of assimilated measurements have the largest influence. However, most probably the aircraft observations have a large influence since they are the second most frequent observation type after SYNOP and provide information about the horizontal and vertical structure. The differences between COSMO-REA6 and COSMO-DS are presumably also the reason for the different correlation coefficients of the IWV datasets and the measured IWV. The correlation coefficient is largest for COSMO-REA6 (0.98), while it is smaller for ERA-Interim (0.96) and the smallest for COSMO-DS (0.89). The spatial patterns of RMSE and the correlation coefficients (not shown) are much less distinct than the patterns of the bias (Fig. 5.3). Two stations — OSNA and HOBU — stick out because of their error characteristics. The bias between GPS and both COSMO simulations is distinctly smaller than at the other stations. Both GPS stations exhibit an abrupt change in difference to simulated IWV in the end of 2010. They are removed

from the data set used in the following sections due to the advanced quality check (Sect. 2.1.3). This analysis shows that COSMO-REA6 outperforms COSMO-DS, which lead to the conclusion that a full reanalysis is superior to a less costly downscaling concerning IWV.

5.1.2 *Comparison of COSMO-REA2, COSMO-REA6 and ERA-Interim with GPS*

An advanced comparison for a longer time period (2007–2013) for COSMO-REA2, COSMO-REA6, and ERA-Interim to GPS is described in the following. Due to the extended time period the reasons for differences can be better assessed. Additionally, a more strict quality check (cf. Sect. 2.1.3) is applied to the GPS measurements. The height correction (Sect. 4.1) is applied as in the evaluation of COSMO-DS (Sect. 5.1.1).

For the four data sets, the averaged IWV differs (GPS: 16.4 $\mathrm{kg\,m^{-2}}$, COSMO-REA2: 15.3 $\mathrm{kg\,m^{-2}}$, COSMO-REA6: 15.7 $\mathrm{kg\,m^{-2}}$, ERA-Interim: 16.0 $\mathrm{kg\,m^{-2}}$). Besides the mean IWV, the distribution of occurrence of IWV differs. It is broadest for GPS observations and narrowest for ERA-Interim (cf. Fig. 5.5). Furthermore, the averaged IWV exhibits regional differences (cf. Fig. 5.4). In general, higher IWV means occur in the north of Germany, with low orography, and decreases to the south with higher orography. Since the amount of IWV depends on the height range the corresponding atmospheric column covers, height of the ground above mean sea level and mean IWV are anti-correlated with a correlation coefficient of -0.66. In contrast to the generally higher IWV mean of ERA-Interim compared to the COSMO reanalyses, the Alpine region exhibits lower IWV means than the COSMO reanalyses. Due to the coarser resolution of ERA-Interim the orography is not captured here as well as with COSMO.

As mentioned before and seen in the comparison over one year (cf. Sect. 5.1.1), all three reanalyses are on average drier than the observations (cf. Fig. 5.6). The mean bias over all stations for the reanalyses do not differ much. COSMO-REA6 and ERA-Interim are 0.7 $\mathrm{kg\,m^{-2}}$ drier than the observations and COSMO-REA2 exhibits a bias of 1.2 $\mathrm{kg\,m^{-2}}$ in comparison to the observations. Therefore, COSMO-REA2 is about 0.4 $\mathrm{kg\,m^{-2}}$ drier than COSMO-REA6 and ERA-Interim. Interestingly, the opposite bias of a similar order between COSMO-DE and COSMO-EU, which are comparable to COSMO-REA2 and COSMO-REA6, respectively, is found by Böhme et al. (2011). The coarser model (COSMO-EU) is drier than COSMO-DE which has a finer spatial resolution. While the differences between COSMO-DE and COSMO-EU is nearly constant over the two-year period the difference to the observations changes. Therefore, it is rather difficult to conclude if the difference between the bias of COSMO-DE and COSMO-EU and the bias of COSMO-REA2 and COSMO-REA6 is

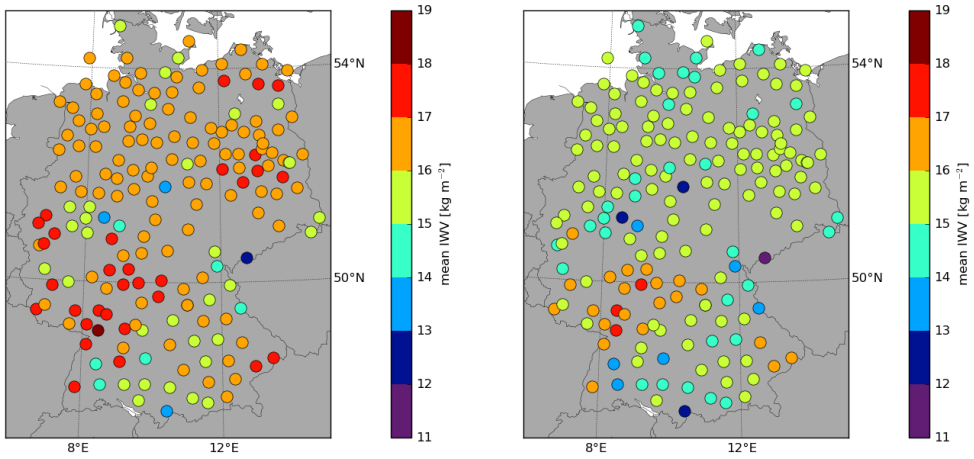

(a) Mean IWV GPS

(b) Mean IWV COSMO-REA2

(c) Mean IWV COSMO-REA6

(d) Mean IWV ERA-Interim

Figure 5.4: Mean IWV for instantaneous values of GPS COSMO-REA2, COSMO-REA6, and ERA-Interim at 183 (COSMO reanalyses) or 133 (ERA-Interim) GPS stations for 2007 - 2013.

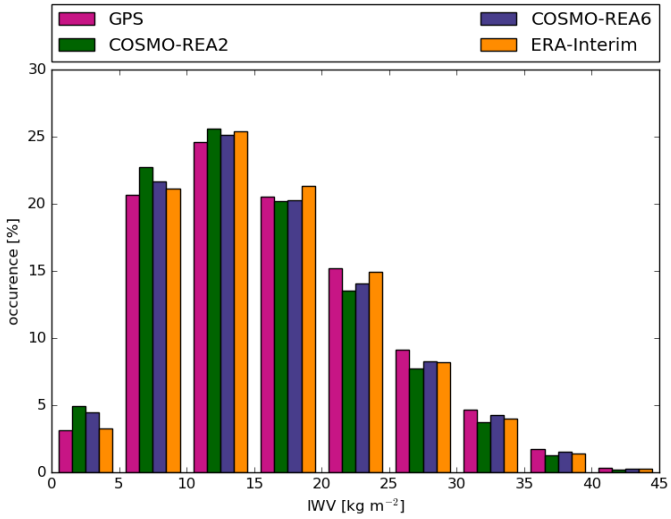

Figure 5.5: Occurrence of IWV values of GPS observations, and COSMO-REA2, COSMO-REA6, and ERA-Interim simulations at 133 GPS stations in 2007 to 2013.

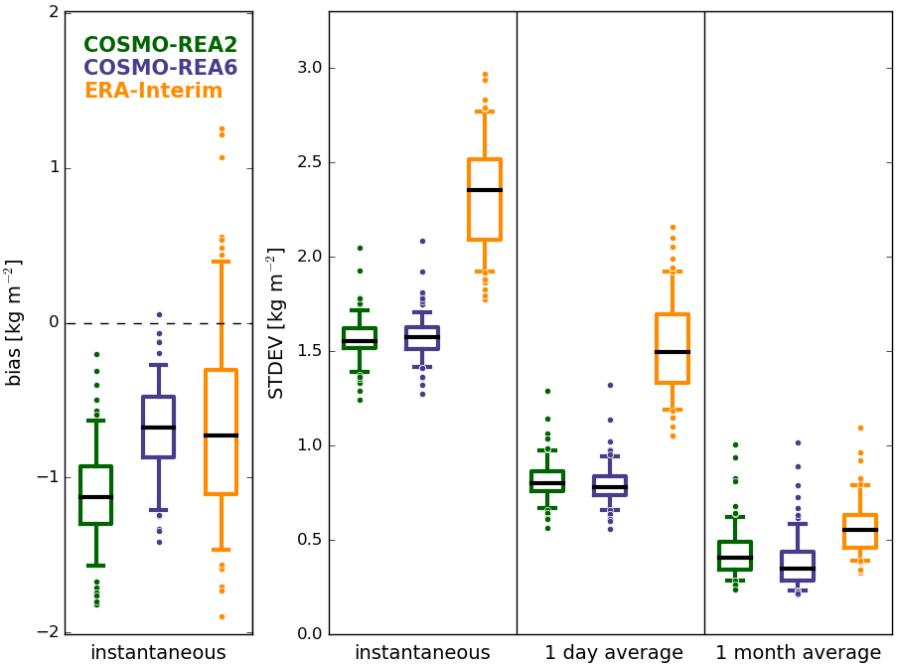

Figure 5.6: 10%-, 25%-, 75%-, 90%-percentiles, outliers (individual points) and median (black horizontal line) of errors of IWV at 133 GPS stations: Bias ($IWV_{simulated}$–$IWV_{measured}$) and standard deviation for simulations with COSMO-REA2 (green), COSMO-REA6 (purple), and ERA-Interim (orange) against GPS observations for instantaneous values, 1 day averages and 1 month averages.

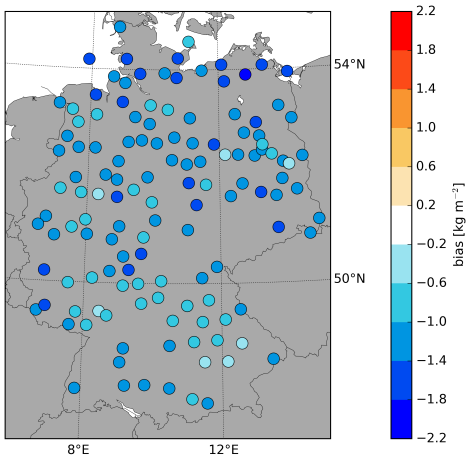

(a) Bias COSMO-REA2 - GPS

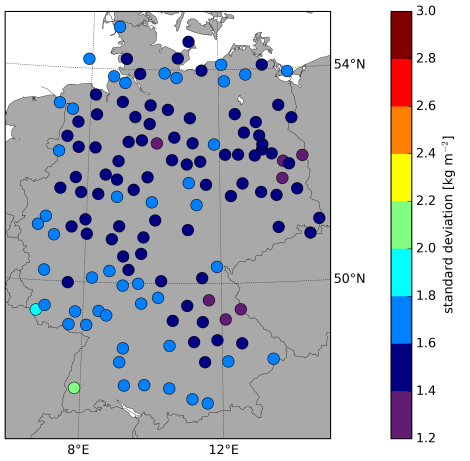

(b) Standard deviation COSMO-REA2 - GPS

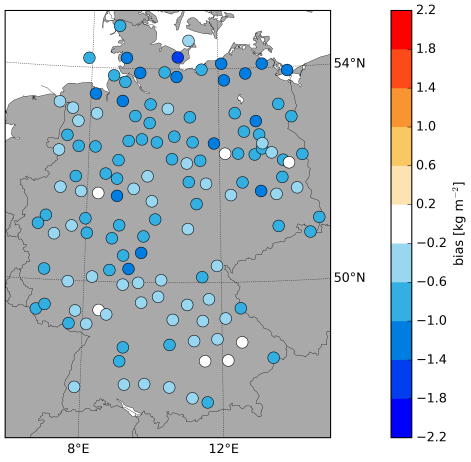

(c) Bias COSMO-REA6 - GPS

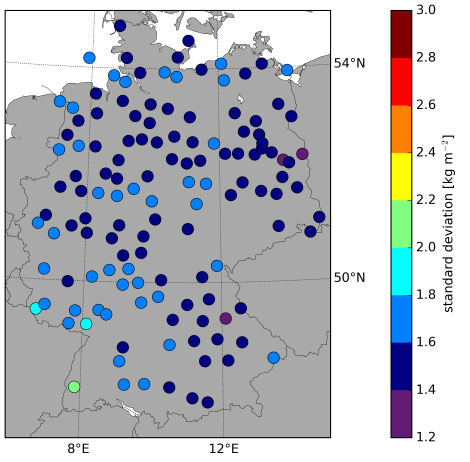

(d) Standard deviation COSMO-REA6 - GPS

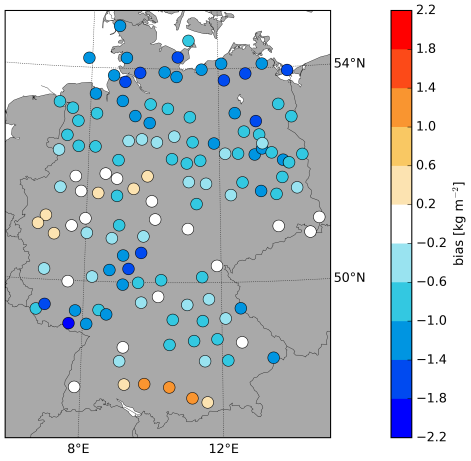

(e) Bias ERA-Interim - GPS

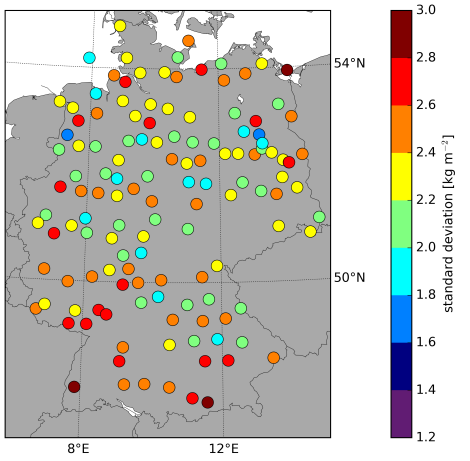

(f) Standard deviation ERA-Interim - GPS

Figure 5.7: IWV bias and standard deviation for instantaneous values of COSMO-REA2, COSMO-REA6, and ERA-Interim compared to 133 GPS stations for 2007 - 2013.

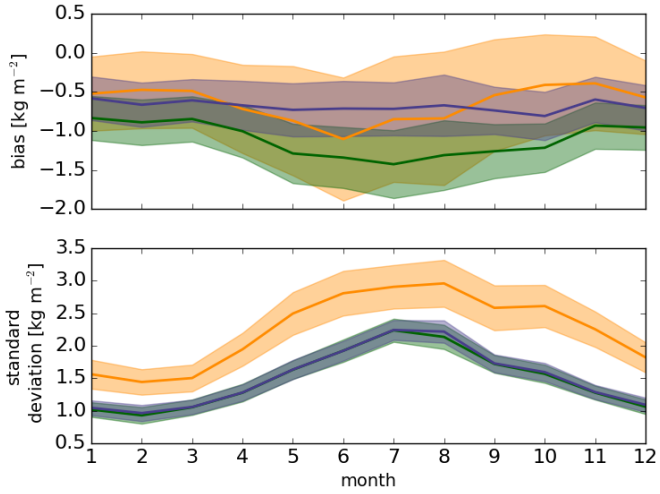

Figure 5.8: (top) Monthly means of bias and (bottom) monthly means of standard deviation of IWV simulated with COSMO-REA2 (green), COSMO-REA6 (purple), and ERA-Interim (orange) compared to observations at 133 GPS stations fort the years 2007-2013. The standard deviation of the respective error is shaded.

caused by a change in the model version. The reduction of LHN in COSMO-REA2 compared to COSMO-DE is also likely to influence the bias (cf. Sect. 3.1).

Again the differences between the reanalyses are small compared to the differences between the stations. For the two COSMO reanalyses, COSMO-REA2 and COSMO-REA6, the bias ranges from $-1.8\,\mathrm{kg\,m^{-2}}$ to $-0.2\,\mathrm{kg\,m^{-2}}$ and from $-1.4\,\mathrm{kg\,m^{-2}}$ to $0\,\mathrm{kg\,m^{-2}}$, respectively. The regional distribution is the same for both reanalyses (Fig. 5.7, left). In contrast to that, the spread of bias at the GPS stations is much larger for ERA-Interim (-1.9–1.3 $\mathrm{kg\,m^{-2}}$). At some stations ERA-Interim is even more moist than the measurements. While in COSMO-REA2 and COSMO-REA6 no regional dependency of the bias can be found, in ERA-Interim IWV at grid points in the Alpine region is larger than of the corresponding observations. This could be due to the coarser ERA-Interim grid which requires a larger height correction to the centre of the ERA-Interim grid cell. A correlation of 0.5 is found between the model height and the bias. Such a correlation could not be found for the COSMO reanalyses. Furthermore, the bias of the COSMO reanalyses is not related to the station height, the height differences between model grid point and GPS station, or the mean IWV. All correlations between the bias and these parameters are lower than 0.2. There is also a dependency of bias on the time of the year (cf. Fig. 5.8, top). In summer months the mean absolute bias for COSMO-REA2 and ERA-Interim is about $0.5\,\mathrm{kg\,m^{-2}}$ higher than during winter. This difference cannot be seen in COSMO-REA6.

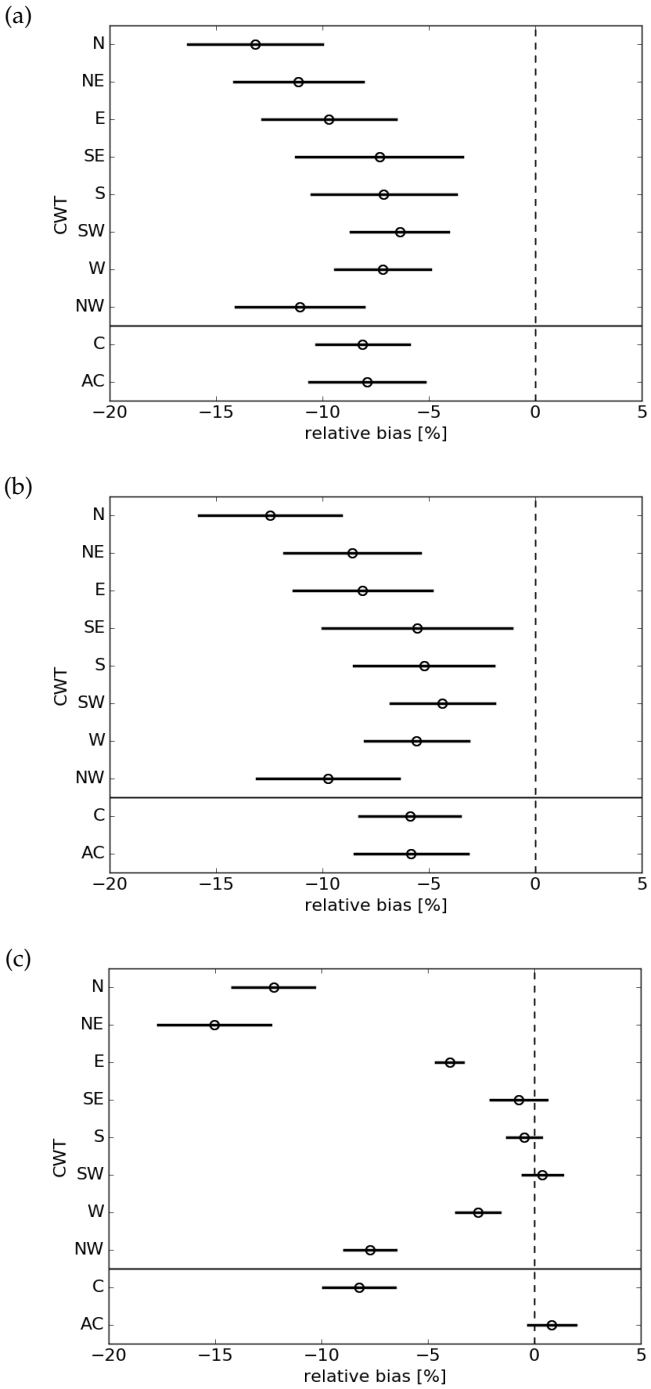

Figure 5.9: (circle) Mean relative bias normalised with the mean IWV of the corresponding CWT class and (solid lines) its standard deviation of (a) COSMO-REA2, (b) COSMO-REA6, and (c) ERA-Interim compared to 133 GPS stations for 2007–2013 distinguished by 10 CWTs: north (N), north-east (NE), east (E), south-east (SE), south (S), south-west (SW), west (W), north-west (NW), cyclonic (C), and anticyclonic (AC).

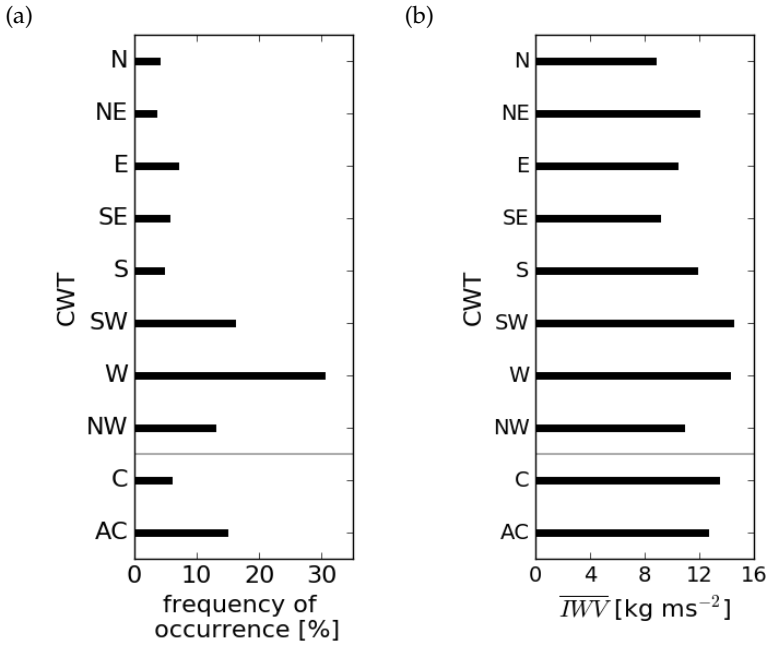

Figure 5.10: (a) Frequency of occurrence and (b) mean IWV of CWT as in Fig. 5.9 in the time period 2007–2013.

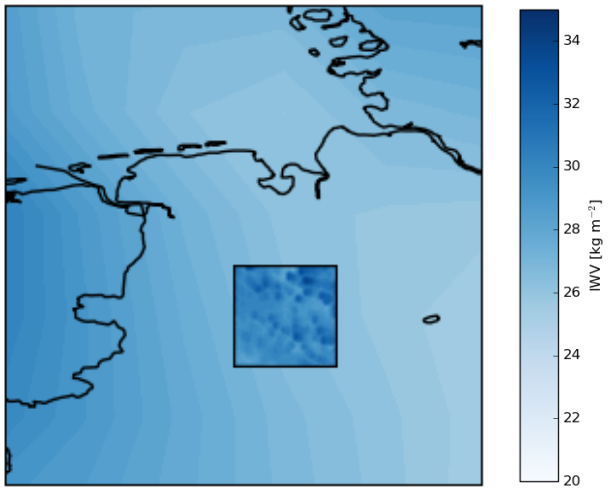

Figure 5.11: Map of IWV in North-West Germany simulated with ERA-Interim and COSMO-REA2 (square) for 2 August 2013, 12 UTC. The square denote one ERA-Interim grid box and includes 1053 COSMO-REA2 grid boxes.

Furthermore, the dependency of the bias on the Circulation Weather Type (CWT) is assessed (Fig. 5.9). The CWT classification distinguishing between 10 CWTs — north (N), north-east (NE), east (E), south-east (SE), south (S), south-west (SW), west (W), north-west (NW), cyclonic (C), and anticyclonic (AC) — based on ERA-Interim reanalysis is provided by Philipp et al. (2016). To eliminate the effect of differences in mean IWV associated with different CWTs (cf. Fig. 5.10), relative biases between the reanalyses and GPS observations normalised with the mean IWV of the respective CWT are used. In general, smallest differences to GPS observations are associated with southern CWTs and largest with northern or north-eastern CWTs. While for both COSMO reanalyses the differences between the CWT classes is about 7 percentage ($0.5\,\mathrm{kg\,m^{-2}}$) the dependency of the relative bias of ERA-Interim is much larger: >15 percentage ($1.9\,\mathrm{kg\,m^{-2}}$). However, the differences in each CWT class is much smaller for ERA-Interim than for the COSMO reanalyses. The directional difference for the COSMO reanalyses is similar to the one identified by Böhme et al. (2011).

The mean standard deviation of the COSMO reanalyses compared to GPS observations is much smaller ($1.6\,\mathrm{kg\,m^{-2}}$) than for ERA-Interim ($2.4\,\mathrm{kg\,m^{-2}}$, cf. Fig. 5.6). Similar to the bias the differences between the reanalyses are low compared to the range of standard deviations at the GPS stations. Thereby, the range of standard deviation across the different stations is larger for ERA-Interim (1.8–$3.0\,\mathrm{kg\,m^{-2}}$) than for COSMO-REA2 and COSMO-REA6 (1.3–$2.1\,\mathrm{kg\,m^{-2}}$). ERA-Interim does show a random distribution of standard deviation while the COSMO reanalyses show a slight tendency to smaller standard deviations in western Germany and higher standard deviation in the east of Germany. There is a strong dependency of standard deviation on the season for all three reanalyses (cf. Fig. 5.8, bottom). During summer the mean standard deviation is about double the mean standard deviation in winter. This indicates higher absolute IWV variability in summer month which is more challenging to simulate.

The higher standard deviations of ERA-Interim compared to the COSMO reanalyses can be explained as mentioned before (cf. Sect. 5.1.1) with the inability of ERA-Interim to represent the small structures in the IWV field related to topography variation due to its coarser resolution. The variability which is missed due to the coarse resolution can be quantified by the standard deviation as a measure of variability within one ERA-Interim grid box showed by COSMO-REA2. Within an ERA-Interim grid box in north-west Germany (Fig. 5.11), which comprises 1053 COSMO-REA2 grid boxes, the mean standard deviation is $0.7\,\mathrm{kg\,m^{-2}}$ for the years 2007-2013. This corresponds to the difference between the mean standard deviation of ERA-Interim and COSMO-REA2. This gridbox is chosen because it exhibit only small

variation in height (24–186 m AMSL) to keep the variability related to topography variation low.

However, an increase in resolution from 6 to 2 km seems not to further enhance this ability of the model. This shows that the high spatial variability of IWV is one factor to hamper the simulation of IWV fields.

As shown, IWV is also highly variable on temporal scales. These variabilities are also challenging to analyse from limited observation. The standard deviation is distinctly reduced when averages instead of instantaneous model values are used (Fig. 5.6). Considering daily averages reduces the standard deviation from $1.6\,\mathrm{kg\,m^{-2}}$ ($2.4\,\mathrm{kg\,m^{-2}}$) to $0.8\,\mathrm{kg\,m^{-2}}$ ($1.5\,\mathrm{kg\,m^{-2}}$) for both COSMO reanalyses (ERA-Interim). The effect is even larger for a longer averaging time of 1 month, namely a reduction to $0.4\,\mathrm{kg\,m^{-2}}$ and $0.6\,\mathrm{kg\,m^{-2}}$ for the COSMO reanalyses and ERA-Interim, respectively. This results in a reduction of differences of standard deviation between the models. Furthermore, the distribution of standard deviations over all stations changes. For instantaneous IWV values it is nearly symmetrical while it is shifted to the lower values with increasing averaging time. The range of standard deviation is nearly constant for the COSMO reanalyses but decreasing with increasing averaging time for ERA-Interim. Depending on the station, the standard deviation is decreased between 58 and 85% by averaging over one month periods. The regional distribution of this reduction are very similar for all three models (cf. Fig. 5.7). In central Germany the standard deviation tend to be more decreased than in north and south Germany. A dependency of station height could not be found. Obviously, the processes which took place on small temporal scales proceed also on small spatial scales. If a model as ERA-Interim is unable to simulate these processes because of its resolution the standard deviation is increased. A temporal average leads to a decrease of standard deviation since these processes are not resolved any more in the averaged observations. Maybe the differences between the stations result from differences in dominance of small-scale processes in the regions. The mean standard deviation for one month averages is nearly the same for the COSMO reanalyses and ERA-Interim. The higher spatial resolution is thus not beneficial any more. Therefore, ERA-Interim is similarly suitable as the COSMO reanalyses for monthly means for example for climate studies

5.1.2.1 *Why do large IWV differences occur?*

As described in Sect. 5.1.2 the overall agreement of the COSMO reanalyses with GPS observations is good. More than 98% of the differences of 15-minute IWV between COSMO-REA2, COSMO-REA6, and GPS are smaller than $5\,\mathrm{kg\,m^{-2}}$. About 40%, 50%, and 70% of the differences COSMO-REA2 - GPS, COSMO-REA6 - GPS, and COSMO-

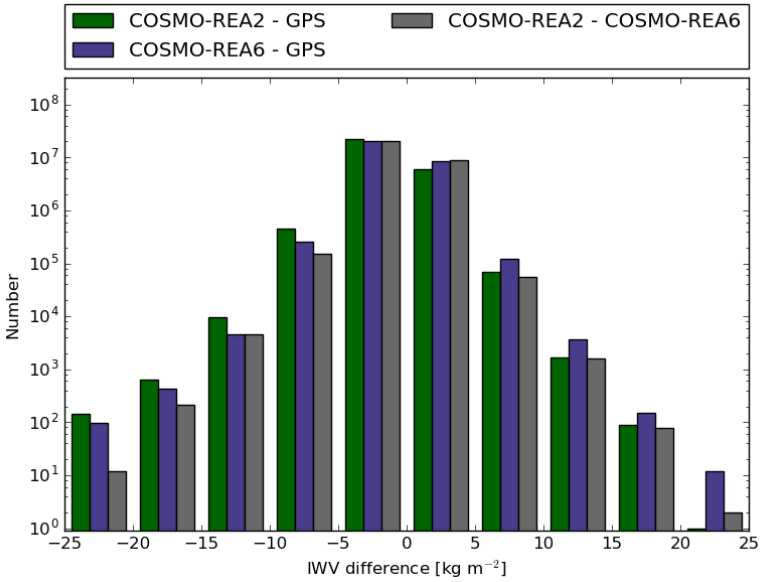

Figure 5.12: Number of pairwise differences between IWV simulated with COSMO-REA2, COSMO-REA6 and observed with GPS at 183 GPS stations in Germany for the years 2007-2013.

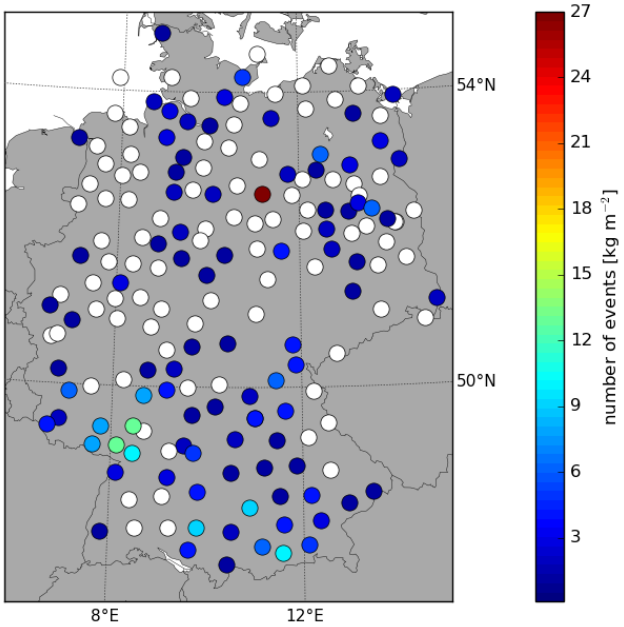

Figure 5.13: Number per gridpoint of pairwise differences larger than 15 kg m^{-2} between IWV simulated with COSMO-REA2 and COSMO-REA6 gridpoints corresponding to 183 GPS stations in Germany for the years 2007-2013.

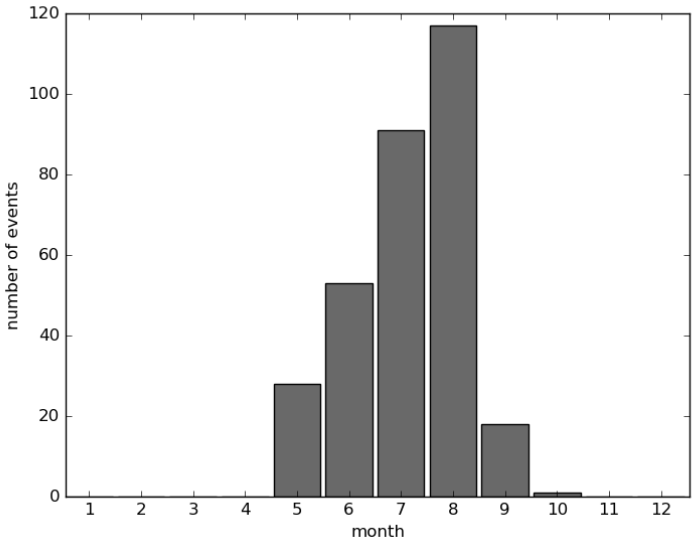

Figure 5.14: Number of pairwise differences larger than 15 kg m^{-2} between IWV simulated with COSMO-REA2 and COSMO-REA6 grid-points corresponding to 183 GPS stations (cf. Fig. 5.13) in Germany for the years 2007-2013 per month.

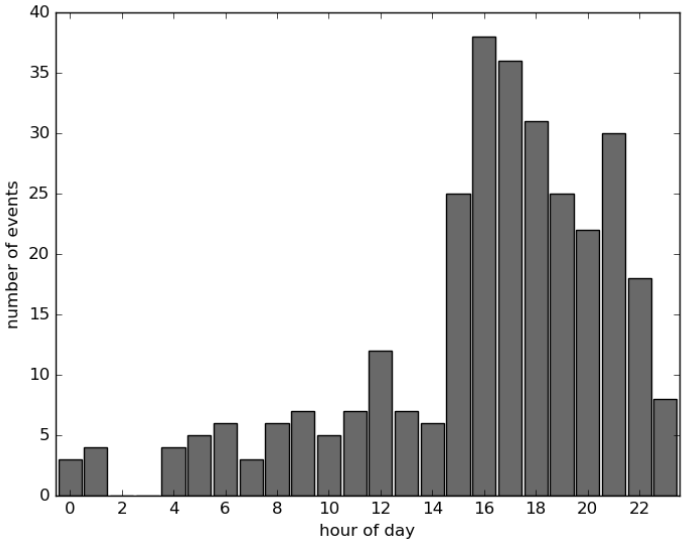

Figure 5.15: Same as Fig. 5.14 but for hour of day.

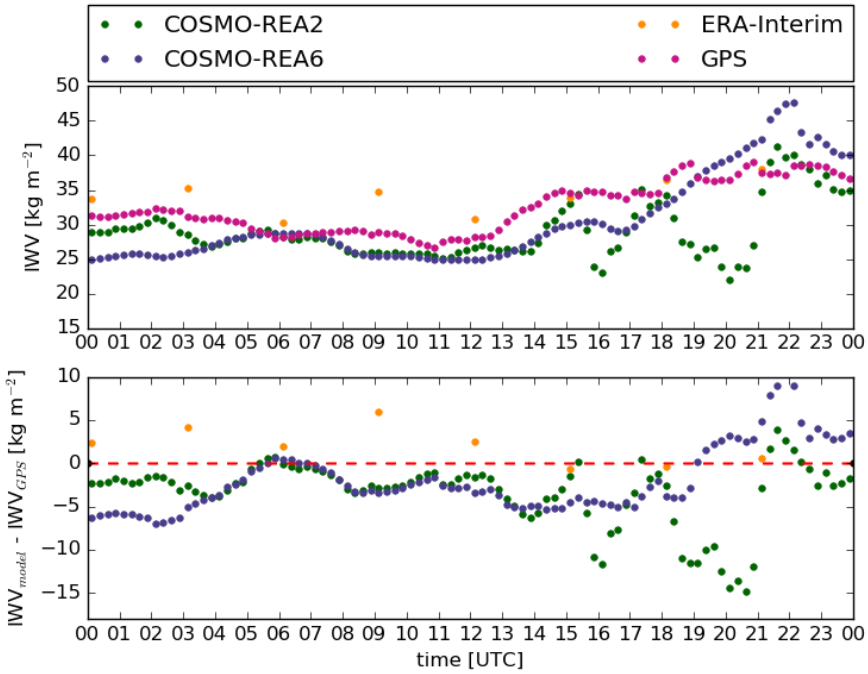

Figure 5.16: Top: Time series of IWV measured with GPS and simulated with COSMO-REA2, COSMO-REA6, and ERA-Interim. Bottom: Time series of the differences $IWV_{simulated}$ - IWV_{GPS} for the same models for 24 August 2011 at the GPS station 0271 (47.84°N, 11.14°E, cf. 5.17).

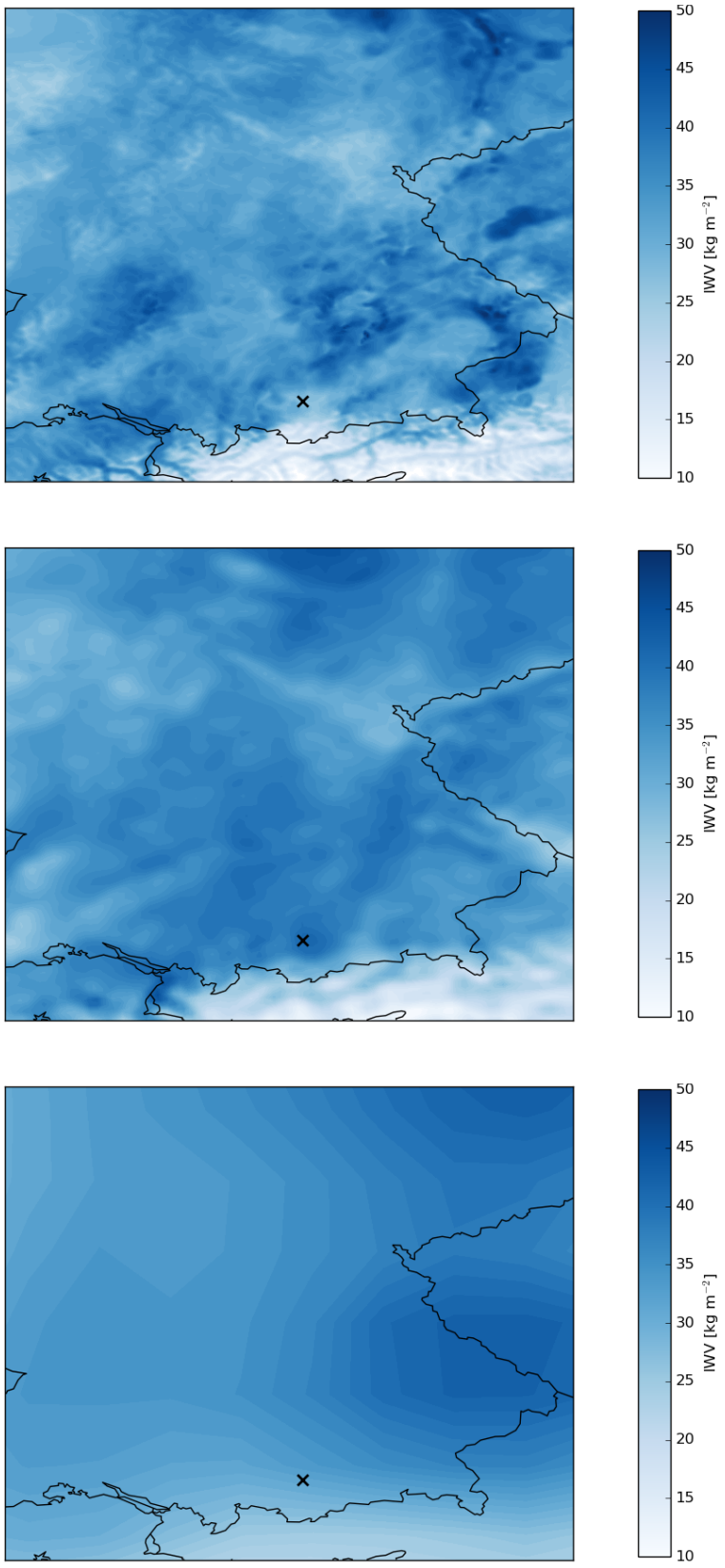

Figure 5.17: Maps of IWV at 24 August 2011 simulated with COSMO-REA2 at 20:45 UTC (top), COSMO-REA6 at 20:45 UTC (middle), and ERA-Interim at 21:00 UTC (bottom). The x marks the GPS station 0271 (47.84°N, 11.14°E)

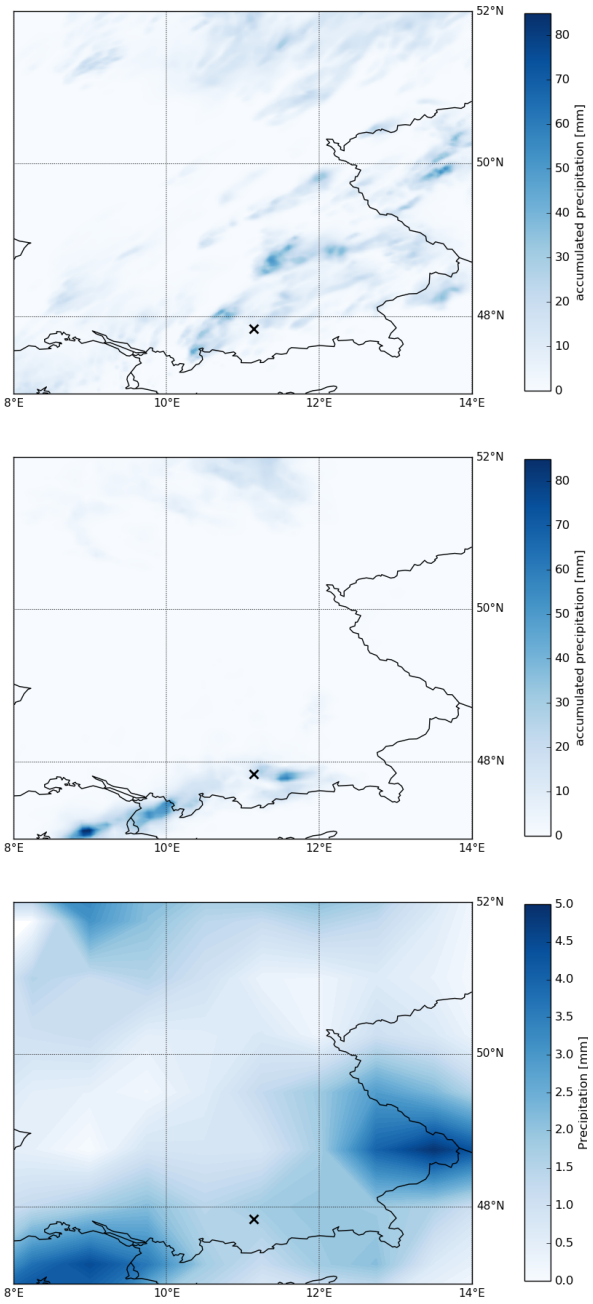

Figure 5.18: Accumulated precipitation of COSMO-REA2 (top) COSMO-REA6 (middle), and ERA-Interim (bottom) for 21:00–00:00 UTC on 24 August 2011. The x marks the GPS station 0271 (47.84°N, 11.14°E). Note, that the plot showing ERA-Interim has a different colour scale.

REA2 - COSMO-REA6, respectively, are even smaller than $1\,kg\,m^{-2}$. However, extreme differences up to $25\,kg\,m^{-2}$ can occur (Fig. 5.12). About 150 (100) GPS observations differ by more than $20\,kg\,m^{-2}$ from COSMO-REA2 (COSMO-REA6). Some of these differences may occur due to erroneous GPS observations, which are not identified with the help of the quality check. However, even between the two reanalyses, at 14 instances differences above $20\,kg\,m^{-2}$ occur. To exclude cases with erroneous GPS observations, only differences between the two COSMO reanalyses are assessed in the following. Concerning the location of events with large differences, two abnormalities can be found. At the station KLTZ (52.6°N, 11.2°E) in the north of Germany, 27 cases with differences larger than $15\,kg\,m^{-2}$ occur. Considering the length of the whole time series this is very few. However, the station with the second most events exhibits only about half as many 15 minutes intervals with such large differences, while at most stations 0 to 3 events occur. Additionally, the surrounding stations of KLTZ exhibits no events at all. These differences occur at 3 July 2009 between 6:00 and 12:00 UTC probably due to a mistake in data assimilation in COSMO-REA6. The second noticeable region is in the region of Palatinate Forest. Here, some stations next to each other show extreme differences on 29 August 2012, 21:00–24:00 UTC. During this time period a convective event occurred in this region.

Except one all events shown in Figure 5.13 occur between May and September, which are predestined months for extreme differences because of their large IWV values (cf. 5.14). In addition to that, the fact that most of the events occur between 15:00 and 22:00 UTC lead to the assumption that these events are related to convective events (cf. Sect. 5.15). Since not all cases can be investigated in detail, an exemplary case study for the GPS station 0271 (47.84°N, 11.14°E) in south Germany is presented below.

On 24 August 2011, a humid, warm air mass moves from southwest over Germany resulting in thunderstorms with strong precipitation in the evening in south-east Germany. The IWV of all four data sets — GPS, COSMO-REA2, COSMO-REA6, ERA-Interim — is nearly constant until 13:00 UTC (Fig. 5.16). The data sets vary between ca. $25\,kg\,m^{-2}$ (COSMO-REA6) and ca. $35\,kg\,m^{-2}$ (ERA-Interim). Later IWV of COSMO-REA6, ERA-Interim and GPS increases until 22:00 UTC. In contrast to that, IWV of COSMO-REA2 increases and decreases during this time period for two times resulting in extreme differences to GPS of $15\,kg\,m^{-2}$ and even larger differences to COSMO-REA6 ($17\,kg\,m^{-2}$).

The IWV field of COSMO-REA2 shows much more spatial variability than of COSMO-REA6 (Fig. 5.17). The range of IWV values is much higher for COSMO-REA2. At the location of station 0271 in south Germany, IWV simulated with COSMO-REA2 is lower than in the surroundings while it is the opposite for COSMO-REA6. In asso-

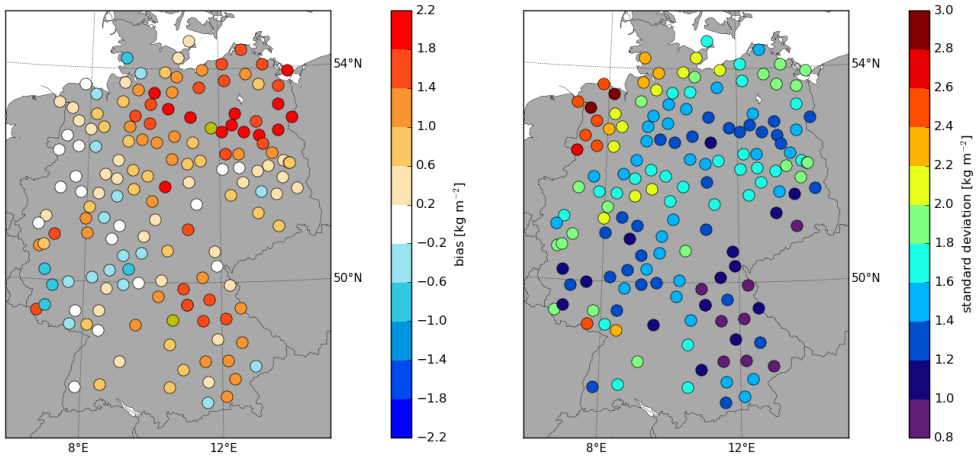

(a) Bias ICON - GPS

(b) Standard deviation ICON - GPS

Figure 5.19: Map of bias (IWV_{ICON}–IWV_{GPS}; left) and standard deviation (right) at 154 GPS stations for 24 and 25 April 2013.

ciation with the different IWV distribution, the convective precipitation also differs between the reanalyses. In general, strong precipitation is simulated by both COSMO reanalyses in south-east Germany (Fig. 5.18). However, the raining cells are stronger and more localised in COSMO-REA6. Additionally, the location of precipitation differs slightly between both reanalyses. ERA-Interim exhibits much less precipitation which is much less localised due to the coarser resolution.

This case study and the statistics of temporal occurrence of large differences suggest a relationship of convective events and large IWV differences. These events are likely to be influenced by the different resolutions of the models due to their local character. Additionally, one of the major differences between the two COSMO reanalyses is the LHN which assimilates radar measurements. Therefore, a study of these convective events focusing on the influence of LHN could help to understand the connection between IWV and precipitation in the COSMO model

5.2 EVALUATION OF HIGH RESOLUTION ICON WITH GPS MEASUREMENTS

The ICON (Sect. 3.3) simulation for the days 24 and 25 April 2013 performed within HD(CP)^2 is evaluated with the observations at 154 GPS stations. Compared to the observations, ICON is too humid for most of the stations (up to 2.3 kg m^{-2}). However, at some stations mean

IWV is up to 0.9 kg m^{-2} smaller than the GPS observations (Fig. 5.19). This is opposite to what is found for COSMO simulations, which are generally drier than the GPS observations as described in Sect. 5.1. However, the results are not easily comparable since ICON is only compared for two days while in the evaluation of the COSMO reanalyses comprises seven years of model runs. This has to be taken into account even more carefully when looking at the standard deviation, which ranges between 0.8 kg m^{-2} and 2.9 kg m^{-2}. As described in more detail in Sect. 6.4, IWV varies between 14 and 18 kg m^{-2} within these days. The relatively large IWV in combination with a large variability in IWV leads to large standard deviations. The largest standard deviations occur in north-west Germany, where IWV is most variable due to the weather situation.

Summarising, IWV from ICON is 0.7 kg m^{-2} larger than IWV from GPS observations on average and the mean standard deviation between model and observation is 1.6 kg m^{-2}.

5.3 SUMMARY AND CONCLUSIONS

The ability of model simulations to represent IWV is assessed in this section. Firstly, the comparison of a dynamical downscaling of ERA-Interim with a full reanalysis including data assimilation shows that the full reanalyses is superior to the downscaling in terms of representation of the small scale variability of IWV.

Secondly, the reanalyses COSMO-REA2, COSMO-REA6, and ERA-Interim are evaluated with GPS observations. All three reanalyses underestimate IWV in comparison with GPS observations. When it comes to random error, the mean standard deviation of both COSMO reanalyses (1.6 kg m^{-2}) is distinctly lower than the mean standard deviation of ERA-Interim (2.4 kg m^{-2}). This indicates a better representation of small scale variability of IWV in the COSMO reanalyses most likely due to the higher resolution. The standard deviations are distinctly decreased for all reanalyses when instead of instantaneous IWV values averages over one day or one month are used resulting in nearly the same standard deviations for all three reanalyses. This suggests that the spatial resolution is not as important for e. g. climatological averages as for resolving processes occurring on small temporal scale.

Despite the low standard deviation of 15 min IWV of both COSMO reanalyses, large differences of more than 20 kg m^{-2} can occur between GPS, COSMO-REA2 and COSMO-REA6 in few cases. These differences are most likely associated with convective precipitation. This analysis shows that the reanalyses are suitable for the investigation of IWV variability while the COSMO reanalyses are superior to ERA-Interim due to their higher resolution.

The ICON simulation in LES configuration shows a good agreement with GPS observations in terms of IWV. In contrast to the reanalyses, IWV simulated with ICON is on average larger than IWV observed with GPS. The standard deviation ($1.6\,\mathrm{kg\,m^{-2}}$) is the same as for the two COSMO reanalyses.

6

ASSESSING THE SMALL-SCALE VARIABILITY

The variability of water vapour on small-scales, meaning meso-γ scale, which are scales comparable to the resolution of NWP is not yet well characterized and understood. However, this small-scale variability is important for the initiation of convection, cloud development and precipitation processes (Sherwood et al., 2010). A prominent example is the convective atmospheric boundary layer where evaporation from the heterogeneous land surface and turbulent mixing create strong water vapour variability by introducing moist eddies (Shao et al., 2013, cf. Fig. 10). Knowledge on water vapour variability is valuable for improving subgrid-scale model parametrizations, for model evaluation, and for instrument intercomparisons.

The variability of IWV can be assessed with different methods. The decrease of the auto-correlation function of the IWV time series can reveal on which temporal scale correlation is reduced and therefore IWV is changed. The lower the auto-correlation of the time series for a distinct lag time the more independent are the IWV values on this time scale from the initial IWV values. The time interval in which the auto-correlation decreases by a factor of e, called e-folding time, is a measure for the strength of decay. After the e-folding decay time the dependency of IWV from the initial values is distinctly decreased. From that it can be concluded which processes lead to the most drastic change in IWV.

Another approved method for characterizing the variability of atmospheric parameters is scaling analysis. This means to identify the scaling behaviour in time series as a power law dependence with length scale of structure functions. The power spectra of kinetic energy, potential temperature and wind are used e. g. to evaluate the realism of model simulation (e. g. Hamilton et al., 2008). The scale dependence of these variables in aircraft measurements was found to have an exponent of -3 for scales above 800 km and $-5/3$ for scales below 500 km (e. g. Nastrom et al., 1984). Since water vapour is a passive tracer for advection it could be expected that its scaling is about the same. However, the existing studies of water vapour spectra show that the slope can be much steeper (Cho et al., 2000; Kahn and Teixeira, 2009; Kahn et al., 2011; Fischer et al., 2013). This difference to other atmospheric quantities can only partly be explained by the processes as evaporation and precipitation that remove or add water vapour. It is not yet completely understood. A short overview about existing studies is given in the following.

Kahn and Teixeira (2009) used Atmospheric Infrared Sounder (AIRS) observations of water vapour to investigate the scaling. They does not find a scale break at all or a very vague scale break on length scales between 100 and 1000 km. The exponent varies between -1.6 and -2.0 for height levels between 500 and 925 hPa over ocean. A comparison of height-resolved water vapour scale dependency between AIRS measurement and model simulations by Kahn et al. (2011) showed that the small-scale variance in the models (Community Atmosphere Model, version 5 (CAM5) and Geophysical Fluid Dynamics Laboratory (GFDL)) and the analyses (ECMWF and Modern ERA Retrospective Analysis for Research and Applications (MERRA)) is too small. Furthermore, they found that the slope of IWV scaling is more similar to the scaling of temperature than to the scaling of height-resolved water vapour.

Fischer et al. (2013) used airborne Differential Absorption Lidar (DIAL) observations of height-resolved water vapour at height levels between 1.5 and 10.4 km to analyse the horizontal structure scaling between 5 and 100 km. They confirmed the result of Fischer et al. (2012) that there are two distinct scaling regimes: in air masses with convection a scaling exponent of -1.35 is found and where only large-scale advective processes occur the scaling exponent is -1.63. The exponent for convective air masses is similar to the one found by Kahn et al. (2011) for meso-scale variability.

To extend these analyses to smaller time scales and assess the error of representativeness, the standard deviation of IWV within time intervals between 5 min and 3 h is used (cf. Sect. 6.4). For assessing both temporal and spatial scale simultaneously, a simulation with ICON in LES configuration which exhibit a horizontal resolution of 156 m and a output frequency of 10 s–5 min is used. From this simulation, the IWV correlations and standard deviations for distances smaller than 10 km and shorter than 1 h can be assessed.

6.1 AUTO-CORRELATION FUNCTION

The temporal variability of IWV is investigated in the following by an auto-correlation analysis. The auto-correlation can reveal on which temporal scales atmospheric processes reduces correlation and therefore the change IWV. To this end, the auto-correlation of IWV simulated with COSMO-REA6 and measured with GPS at a north-western station in Germany (51.5°N, 9.9°E) is computed exemplarily (cf. Fig. 6.1). The time series over the years 2007–2013 are separated by seasons. For both data sets, all seasons show a similar behaviour: The auto-correlation function decreases monotonically with increasing lag. The e-folding time varies between roughly 24 h and 100 h, with shortest e-folding times in summer and longest in spring. However, the standard deviation of the auto-correlation function and therefore also of

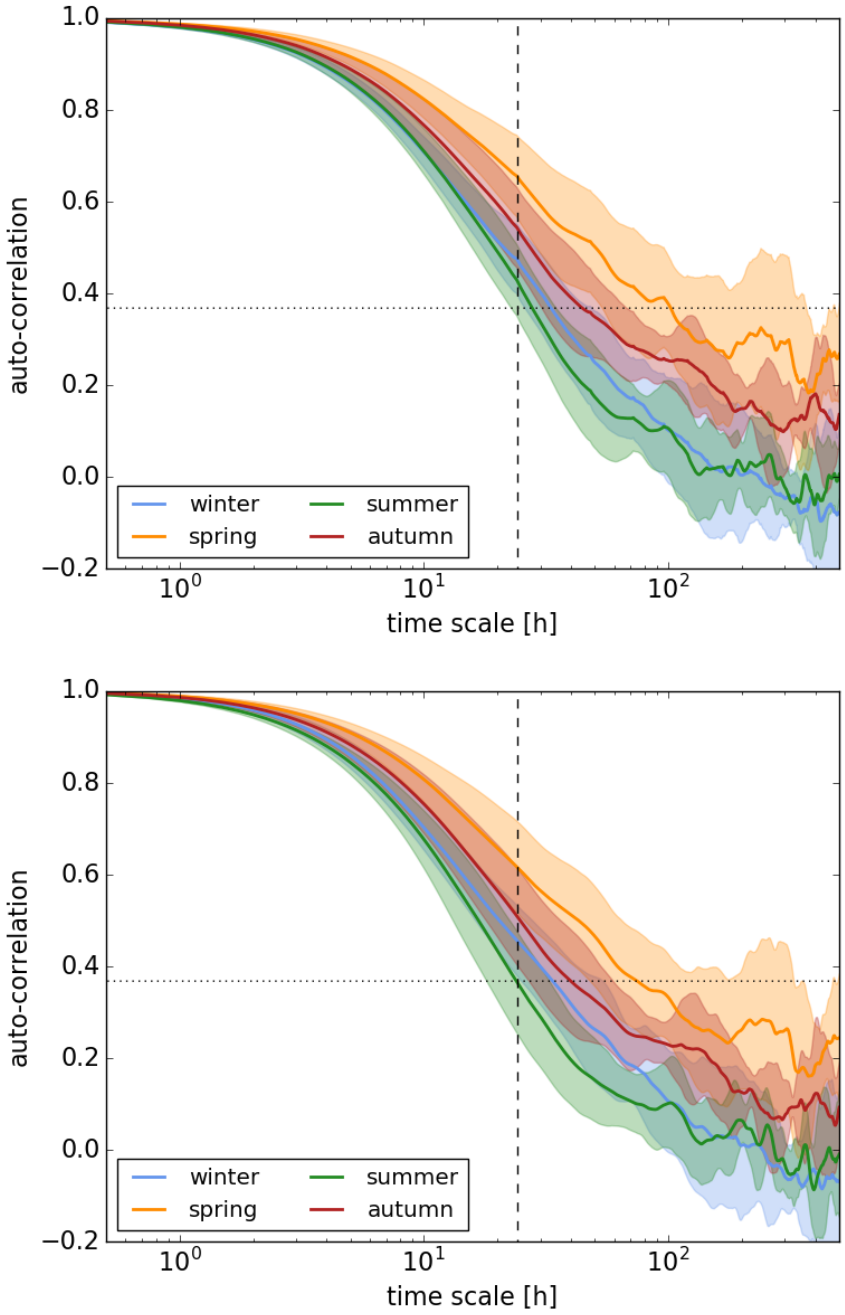

Figure 6.1: (solid lines) Mean auto-correlation of IWV and (shaded areas) its standard deviations (top) observed with GPS and (bottom) simulated with COSMO-REA6 for the years 2007–2013 averaged for each at the GPS station 0650 (51.5°N, 9.9°E) in central Germany. The horizontal dotted line represents e^{-1} and the vertical dashed line represents 24 hours.

the e-folding time are large and largest in spring. The e-folding times at most other stations are in about the same range with the same order of seasons (not shown). A slightly shorter e-folding decay time of 20 h in GPS and MWR observations and simulations with COSMO-DE during April and May 2013 at JOYCE is found in a previous study (Steinke et al., 2015).

From the e-folding time, it can be concluded that the processes leading to the strongest change in IWV are on time scales associated with synoptic variability. This result gives also important limitations on the influence of temporal matching in IWV comparisons and on generation of climate data records. The difference between the seasons indicate more or stronger changes due to synoptic systems during summer than during spring.

6.2 SCALE ANALYSIS

For a closer look at the scale dependencies resulting from IWV variabilities, the power spectrum is computed for a time series of IWV simulated with COSMO-REA6 and measured with GPS at the same northwestern station in Germany (51.5°N, 9.9°E) that is used for the analysis of auto-correlation (Sect. 6.1) with the method by Welch (1967). In general, the power spectral density increases with increasing time scale (Fig. 6.2). For both data sets, the energy is highest in summer, second highest in autumn, second lowest in spring and lowest in winter. This order of magnitude most likely results from different amount of variability in each season.

On time scales between 1.5 and 21 h, which corresponds to a length scale of approximately 30–380 km for a mean wind speed of $5\,m/s$, the exponent range from -1.5 (-1.3) in winter and spring to -2.5 (-2.2) in autumn to -3.5 (-2.8) in summer for COSMO-REA6 (GPS). In general the exponents for COSMO-REA6 are higher than for GPS observations. However, the differences between the seasons of each data set are very similar.

For time scales lower than 1 h the decrease of spectral density with decreasing time is less strong for GPS observations than for COSMO-REA6 simulations. A possible explanation is given in the following. On this time scale, GPS measurements are smoother due to the near-realtime retrieval as described in Sect. 2.1.2. This is probably causing a rather random variability and thus approaching a constant spectrum.

Summarizing, both data sets show a clear seasonal dependency, representing different synoptic situations. However, the differences between the seasons of each data set are very similar. For autumn the scaling exponents are in accordance with Kahn et al. (2011) but on the higher end for exponents expected for height-resolved humidity. This might support the argument of Kahn et al. (2011), who found

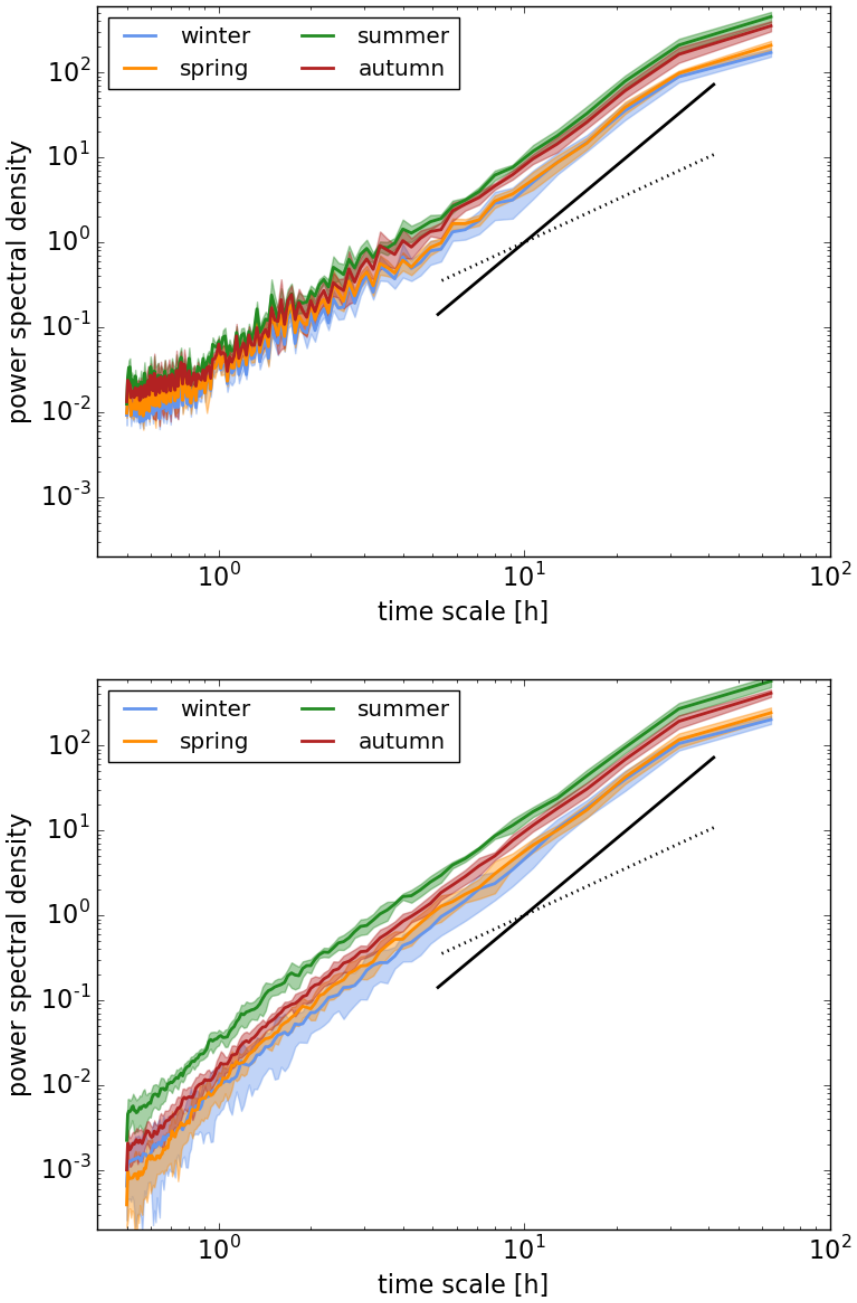

Figure 6.2: (solid lines) Power spectra of IWV and (shaded areas) its standard deviations (top) observed with GPS and (bottom) simulated with COSMO-REA6 for the years 2007–2013 averaged for each season at the GPS station 0650 (52.4°N, 7.1°E) in central Germany. The black solid line show a slope of -3 and the black dotted line show a slope of -5/3.

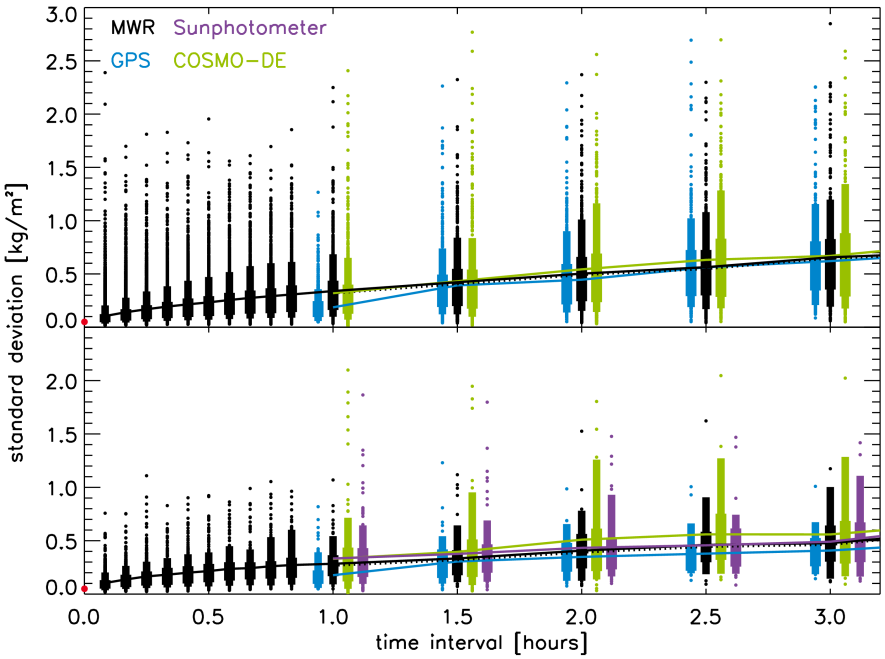

Figure 6.3: Lines: mean standard deviation of IWV during HOPE computed for varying intervals. Displayed are: MWR with 15 min resolution (dotted black), MWR with 5 s resolution (solid black), GPS (blue), and COSMO-DE (green). For the 5 s MWR measurements, the GPS measurements, and the COSMO-DE simulation the vertical bars indicate the 10, 25, 75, and 90%-percentiles of the standard deviation. The single dots indicate the outliers. The bottom panel additionally includes sun photometer data (purple) and is limited to coincident measurements during daytime clear-sky conditions. The red dot on the y-axis represents the noise level of MWR. (published in Steinke et al. (2015))

that IWV might not be a good indicator for the dependency of height-resolved humidity on different situations but rather for the temperature. This and the difference of the IWV scaling depending on the season, as seen in this study, show the need for studies of the scaling behaviour with respect to varying synoptic situations. But a study on IWV scaling for other seasons does not yet exist.

6.3 VARIABILITY IN SHORT TIME PERIODS

The following study of temporal variations due to small scale processes was already published by Steinke et al. (2015). It aims at the estimation of uncertainty due to temporal mismatching of measurements and the ability of GPS observations and COSMO-DE simulations with 15 min resolution to capture IWV variabilities.

The time series of MWR, GPS, and sunphotometer are observed during HOPE in April and May 2013 at JOYCE (cf. Sect. 4). The obser-

vations are complemented by operational simulations with COSMO-DE. Here, COSMO-DE is used instead of COSMO-REA2 since this study was performed before the COSMO reanalyses had been finished for this time period. However, the results should be comparable since COSMO-DE and COSMO-REA2 are very similar to each other (cf. Sect. 3.1). The IWV standard deviation from these time series are computed over varying time intervals from 5 min to 3 h (cf. top panel in Fig. 6.3). Note that only coincident measurements and simulations are used and only the MWR can provide estimates below 1 h. Generally, the mean standard deviation increases from $0.1\,\mathrm{kg\,m^{-2}}$ at 5 min to $0.4\,\mathrm{kg\,m^{-2}}$ at 1.5 h showing some saturation with $0.6\,\mathrm{kg\,m^{-2}}$ at 3 h intervals.

For time intervals of 1.5 h and longer, MWR, GPS and COSMO-DE again show a similar behaviour. In fact, they lie within their 25%- and 75%-percentiles. However extreme values reach standard deviation of $2.0\,\mathrm{kg\,m^{-2}}$ and higher at time intervals >1 h.

The GPS measurements show an offset for the 1 h interval. This is caused by the processing method. As described in Sect. 2.1.2 and Sect. 7.1 GPS measurements within 1 h are relatively smooth and exhibit a jump at the beginning of each hour due to the near-realtime retrieval. However, the mean standard deviation of the 15 min MWR averages are overall only slightly smaller than the mean standard deviation of the 5 s averages. This indicates firstly, that for time scales of a few hours, the coarser resolution of 15 min is sufficient enough for resolving the mean IWV variability. Secondly, that for these time intervals, GPS is well-suited as a reference instrument for model evaluation since it captures the same variability as the MWR. And thirdly, that the operational NWP model COSMO-DE is capable of reproducing the observed mean variability of IWV.

For time intervals shorter than 1 h, only the 5 s MWR data can partially resolve the short-scale, turbulence-induced variability of IWV. The minimum detected average standard deviation of $0.1\,\mathrm{kg\,m^{-2}}$ is twice as high as the MWR noise level and thus represents a lower boundary for the evaluation MWR measurements. As for the standard deviation on intervals greater than 1 h, the standard deviation increases with increasing time interval, however the slope is steeper on the shorter time scales. At the shortest time scales, the variability is dominated by a cascade of turbulence elements in the inertial subrange, whereas at increasing time scales the variability is probably dominated by the variability of subsequent updraught and downdraught regions. Noteworthy are also standard deviation values large than $1\,\mathrm{kg\,m^{-2}}$ even at the shortest time scales, which are predominantly caused by clouds (cf. Fig. 6.3).

Focusing on clear-sky, daytime cases allows to include the sunphotometer (cf. bottom panel in Fig. 6.3). When only coincident data from MWR, GPS, sunphotometer and COSMO-DE are used, the

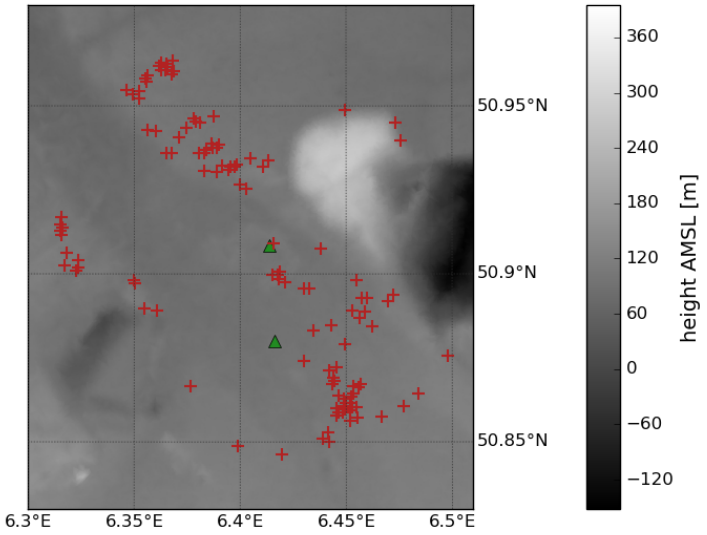

Figure 6.4: Location of 119 ICON gridpoints and 2 MWRs used in Sect. 6.4. The background is shaded according to orography of ICON.

mean standard deviations are lower by approximately 0.25 kg m^{-2} compared to the full time series (cf. bottom panel in Fig. 6.3). This is caused by the exclusion of cloudy cases that leads to the disappearance of high standard deviations. That means that hardly any standard deviations higher than 1 kg m^{-2} in any time interval occur once (partially) cloudy scenes are filtered out.

In summary, the change of the mean standard deviation with different time intervals, over which it is computed, shows that the variability of IWV is high, meaning standard deviations of more than 1.5 kg m^{-2}, even for time periods shorter than 1 h, which is mostly due to clouds. This variability cannot be resolved by more coarsely resolved data. High-resolution time series from MWR are therefore well suited to evaluate high-resolution atmospheric models like ICON aiming to derive better sub-grid parametrizations for climate models. However, for meso-γ scale comparisons, a resolution of 15 min is sufficient to resolve the mean standard deviation and therewith variability of IWV.

6.4 SPATIO-TEMPORAL VARIABILITY

To asses the temporal and spatial variability simultaneously on small scales, time series at selected gridpoints (Fig. 6.4) located in the vicinity of JOYCE simulated with a highly resolved model set-up of ICON (Sect. 3.3) is used. This high-resolution model run with ICON was performed within the project HD(CP)^2 for 24 to 26 April 2013 (Heinze et al., 2016).

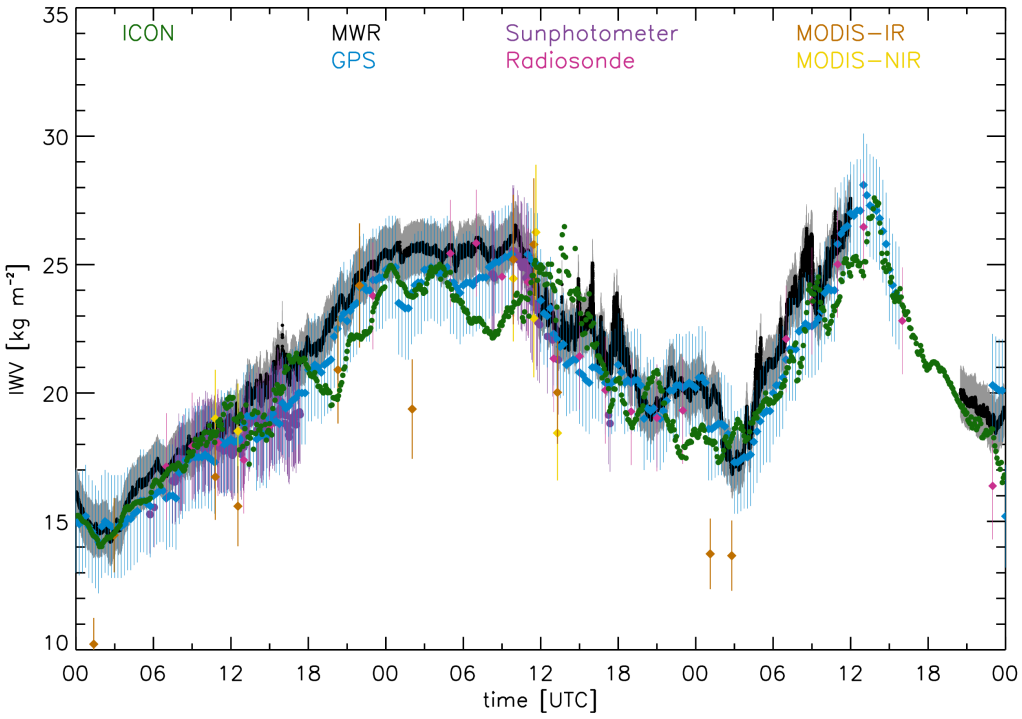

Figure 6.5: Time series of IWV during 24-26 April 2013. Displayed are the measurements and their uncertainties (cf. Tab. 2.1) MWR (black), GPS (blue), sunphotometer (purple), radiosoundings (red), MODIS-IR (orange), MODIS-NIR (yellow), as well as the simulation with ICON (dark green).

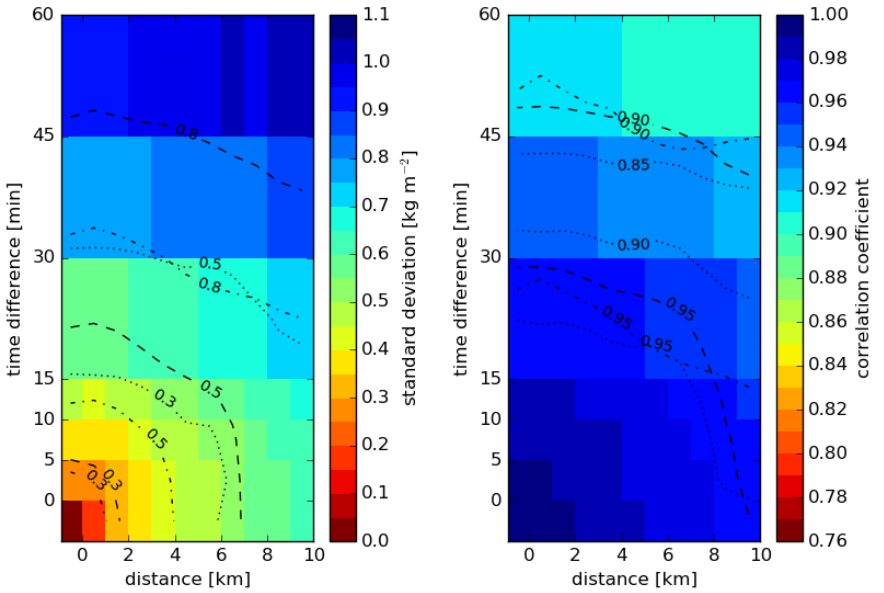

Figure 6.6: Standard deviations (left) and correlation coefficients (right) of IWV from ICON grid points (simulation for 24 - 26 April 2013) as a function of temporal and spatial distance. The lines represent the standard deviations 0.3 kg m^{-2}, 0.5 kg m^{-2}, 0.8 kg m^{-2} and correlation coefficients 0.85, 0.9, 0.95 for the three days: 24 April (dashed), 25 April (dash-dotted), and 26 April (dotted) (cf. Fig. 6.7).

The three days show different weather situations (Fig. 6.5). On 24 April 2013, western Germany is dominated by a high pressure system, which leads to nearly clear sky conditions at JOYCE with only very few, high, thin cirrus clouds during the day and thin boundary layer clouds after 21:00 UTC. The IWV increases nearly constantly from approximately 15 kg m^{-2} to ca. 25 kg m^{-2}. Strong small scale variations after noon (12–15 UTC) occur probably due to turbulence within the evolving boundary layer (cf. Steinke et al., 2015). The boundary layer clouds become more frequently on 25 April 2013, while the high ones dissolve. However, the clouds are still broken. IWV is more or less constant until noon and starts to decrease subsequently with a minimum of 17 kg m^{-2} on 26 April 2013 at 1:00 UTC. Afterwards, IWV increases to 28 kg m^{-2} until 13:00 UTC and then decreases again to 17 kg m^{-2}. During the day, the cloudiness increases until the cloud cover reaches 100% at around 6:00 UTC. The depth of the low clouds also increases and starting at 15:00 UTC there are frequent rainy periods due to a frontal passage, which accumulate to a precipitation of 0.32 mm.

During these three days IWV observations are available from several instruments. In general, the ICON simulation matches the meas-

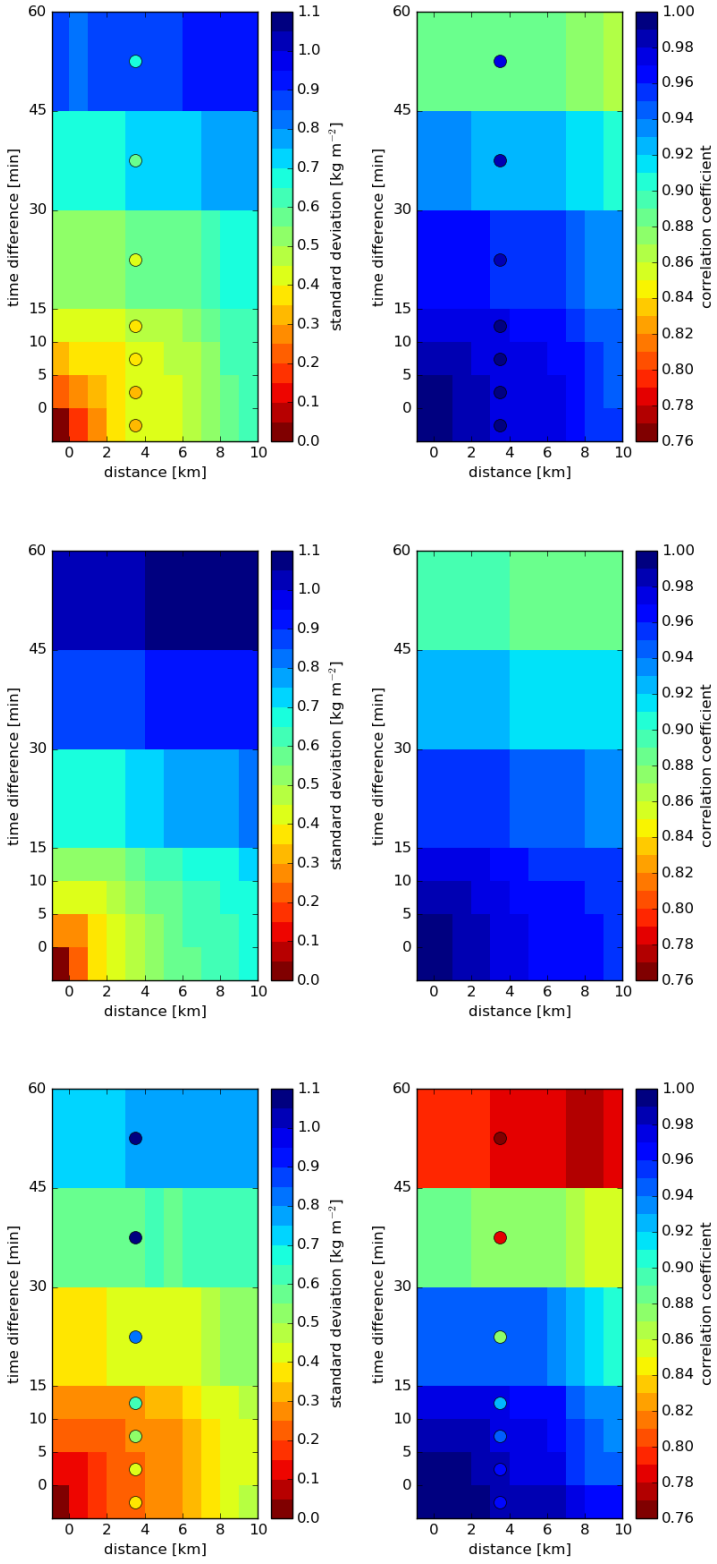

Figure 6.7: Standard deviations (left) and correlation coefficients (right) of IWV from ICON grid points (simulation for (top) 24 April, (middle) 25 April, and (bottom) 26 April 2013) as a function of temporal and spatial distance. The circles represent the standard deviations and correlation coefficients from two MWRs positioned 3.3 km apart.

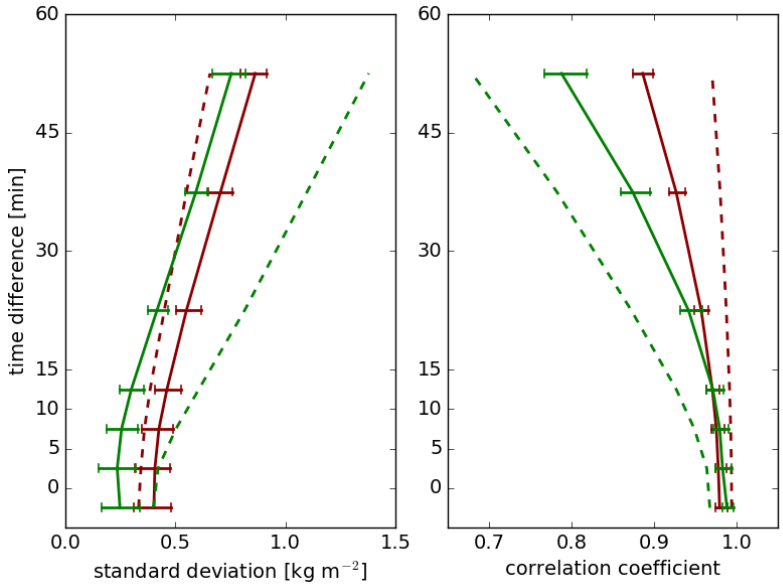

Figure 6.8: Standard deviations (left) and correlation coefficients (right) of IWV from ICON grid points in a distance of $3 - 4$ km (solid) and two MWRs positioned 3.3 km apart (dashed) for 24 April (red) and 26 April (green) for time differences between 0 and 60 min. The horizontal bars show the range due to different grid point combinations for ICON.

urements at JOYCE within their uncertainties (cf. Fig. 6.5). Additionally, the small scale variations of IWV in the convective boundary layer, which can be seen in the MWR measurements are captured by ICON due to the high output frequency. However, while the high variations on 24 April are at the same times, on 25 April, ICON shows high variability a few hours earlier than the MWR measurements. Note that there are missing measurements of the microwave radiometer at 26 April between 12:00 and 20:00 UTC.

For a more quantitative assessment, 119 ICON gridpoints with less than 20 m difference in height are selected in a way that there are nearly the same number of pairs of gridpoints (532–549) for each assessed distance. Note that, the limitation of maximum height difference reduces biases due to height differences. The temporal resolution of the time series at these gridpoints is 5 min during the spinup phase of the model, meaning 00:00 - 06:00 UTC for 24 and 25 April and due to technical problems in the spinup phase 00:00 - 18:00 UTC on 26 April. During the remaining time the output frequency is 10 s. From the time series of these three days, the IWV correlations and standard deviations for distances smaller than 10 km and shorter than 1 h are assessed for the three days (cf. Fig. 6.6). The correlation decreases distinctly with both temporal and spatial mismatch for all days, while the standard deviation increases distinctly.

For a fixed time a distance of $9-10\,\mathrm{km}$ reduces the correlation to 0.97. A similar decrease in correlation occurs when the location is fixed but a time mismatch of $15-30\,\mathrm{min}$ occurs. A mismatch of $9-10\,\mathrm{km}$ and $45-60\,\mathrm{min}$ leads to a correlation of 0.90. A similar behaviour as for the correlation is evident in the standard deviation. This implies that observations with a distance of $8-9\,\mathrm{km}$ can induce the same error as a time shift between measurements of $15-30\,\mathrm{min}$ ($0.6\,\mathrm{kg\,m^{-2}}$). The combination of temporal and spatial mismatch, which is the case for comparisons with radiosondes, can lead to even higher errors amounting to $1.1\,\mathrm{kg\,m^{-2}}$ for $9-10\,\mathrm{km}$ and $45-60\,\mathrm{min}$ difference. The IWV standard deviation observed during the case study of three days seems to be representative for the whole HOPE campaign on time scales shorter than 1 h (Sect. 6.3).

To investigate the influence of the weather situation on the impact of temporal and spatial mismatch, each day is assessed separately (cf. Fig. 6.7). The first two days, 24 and 25 April, do not differ distinctly in their correlation coefficients. The standard deviation for 24 April is in general slightly lower than for 25 April, e. g. $0.51\,\mathrm{kg\,m^{-2}}$ for $15-30\,\mathrm{min}$ and a fixed distance compared to $0.66\,\mathrm{kg\,m^{-2}}$ on 25 April. The reason for this is very likely the different mean IWV of these days: $19.5\,\mathrm{kg\,m^{-2}}$ on 24 April and $21.8\,\mathrm{kg\,m^{-2}}$ on 25 April. As described above, the weather situation is very similar for both days, i. e. no clouds or few very thin clouds. On 26 April, the situation is very different: completely cloudy and light rain due to a frontal passage. Therefore, standard deviation and correlation coefficients differ from the first two days. Despite that mean IWV of 26 April is the same as on 24 April ($19.4\,\mathrm{kg\,m^{-2}}$) the standard deviations are much lower than on the first two days, e. g. $0.39\,\mathrm{kg\,m^{-2}}$ for $15-30\,\mathrm{min}$ and a fixed distance. The differences probably occur due to the lack of small scale variability during the evolution of the boundary layer due to turbulence. The correlation coefficients for 26 April are in general lower than for the first two days by up to 0.09. The reason for this can also be found in the evolution of IWV during the day. Due to the frontal passage there is an abrupt change in the IWV field (cf. Fig. 6.5). This leads to the comparably low correlation coefficients especially for time differences of more than 30 min that is below 0.8. To rule out that the main reason for theses differences is not the different weather situation but the different temporal resolution of the time series, the calculations of standard deviation and correlation for 24 and 25 April is repeated with an artificially reduced temporal resolution of the time series of 5 min for the whole two days (cf. Fig. B.1). The differences between the different resolution for each day are by far of a smaller magnitude than the differences between the days. Therefore, the differences due to different weather situations are stronger than due to the different resolution.

In order to investigate whether the model behaviour is consistent with the observations, time series of IWV averages from two zenith pointing MWRs located 3.3 km apart from each other are used. Due to measurement gaps of one MWR on 25 April, the comparison is only conducted for 24 and 26 April. Both correlation and standard deviation decrease similarly as depicted by ICON (cf. Fig. 6.7). Interestingly, there are slight differences in the absolute values, which can not completely be explained by the fact that several locations of the model output are used while the location of the two MWRs is fixed. The differences get larger the larger the time differences become. For 24 April standard deviation and correlation coefficients of measurements and model run are more similar to each other. The reason for that could be due to missing measurements of one MWR when IWV decreases between 12:00 and 20:00 UTC (cf. 6.5). Due to this, the data sets also do not use the same temporal sampling.

A similar study has been performed before with a different ICON model setup for one day with mostly clear sky conditions (5 May 2013) at 40 gridpoints by Steinke et al. (2015). Since the mean IWV (ca. 16 $\mathrm{kg\,m^{-2}}$) is lower on 5 May the standard deviations are also lower than for 24 and 25 April but not as low as on 26 April. However, the correlation coefficients are more similar to the ones at 26 April. This is probably due to the fact that the general IWV evolution is more similar to the one on 26 than on the first two days. There is a change in increase and decrease of IWV during the day, similar to 26 April.

In conclusion, the standard deviation is an indicator for the small scale variability due to turbulence while the correlation coefficients are strongly influenced by the change of IWV due to large-scales IWV transport. This study shows that the error introduced by mismatch of instruments or model gridpoints depends on the weather situation. Therefore, it is recommended that for instrument intercomparisons not only the temporal and spatial mismatching has to be taken into account but also the weather situation. However, the standard deviation of ca. 1 $\mathrm{kg\,m^{-2}}$ found in the instrument intercomparison (cf. Sect. 4) cannot be explained completely with the representativeness error since a spatial distance of 4 km is estimated to introduce an error due to atmospheric variations of approximately 0.3–0.5 $\mathrm{kg\,m^{-2}}$.

6.5 SUMMARY AND CONCLUSIONS

The variability of water vapour has been assessed with different methods. From the results it can be concluded that synoptic influence is mainly responsible for the fact that the e-folding time of the autocorrelation is approximately between one and four days depending on seasons. This strong dependency of IWV variability on seasons is also revealed by the scale analysis. Furthermore, clouds and broken cloud fields can cause standard deviations of IWV of over 1.5 $\mathrm{kg\,m^{-2}}$

within time intervals of a few hours. Also in clear-sky conditions, atmospheric turbulence determines IWV variability on scales below 1 h. The high resolution (a few seconds) of the MWR enables to observe standard deviations higher than $0.5\,\mathrm{kg\,m^{-2}}$ for time intervals less than 30 min.

To assess spatial and temporal variability simultaneously, simulations on a 156 m grid resolution with the novel ICON model were used. IWV correlation and standard deviation for time differences smaller than 1 h and shorter than 10 km are investigated. It is shown that a temporal mismatch of $15 - 30\,\mathrm{min}$ or a spatial mismatch of 8 – 9 km can already lead to a random error of $0.6\,\mathrm{kg\,m^{-2}}$. A combination of temporal and spatial mismatch introduces even higher errors. The results are confirmed by observations of two MWR operated 3.3 km apart.

7

DIURNAL CYCLE

The knowledge of diurnal variations of IWV are crucial for sampling of water vapour data with satellites, which overpasses the same area only a few times per day. To know the diurnal cycle helps to estimate the uncertainty of e. g. means of satellite observations for climatological use (Diedrich et al., 2016). The same holds true for climatologies of radiosoundings which used to be only once or twice a day.

Furthermore, the knowledge of the diurnal cycle of IWV can help to understand the hydrological cycle, since the local change of water vapour storage $\partial IWV/\partial t$ is determined by the difference between evaporation E and precipitation P — two important processes of the hydrological cycle — and by the inflow or outflow of water vapour ($\mathrm{div}(Q)$):

$$\frac{\partial IWV}{\partial t} = E - P - \mathrm{div}(Q), \tag{7.1}$$

where

- t time
- E evaporation
- P precipitation
- Q flux of water vapour.

Another variable that influences the IWV is the temperature. The Clausius Clapeyron relationship shows that the saturation water vapour pressure only depends on temperature. Under typical atmospheric conditions this relationship can be written as:

$$\frac{de_s}{dT} \approx \frac{Le_s}{R_v T^2}, \tag{7.2}$$

where

- e_s saturation water vapour pressure
- T temperature
- L latent heat of vaporization or condensation of water
- R_v gas constant for water vapour.

This relationship shows an approximately exponential increase in the saturation water vapour pressure due to increasing temperature.

Summarising, the atmospheric parameters influencing the amount of IWV are temperature, latent heat flux and precipitation. To better understand the relationship of these parameters and IWV the diurnal cycles of them simulated with COSMO-REA6 are compared (Fig. 7.1).

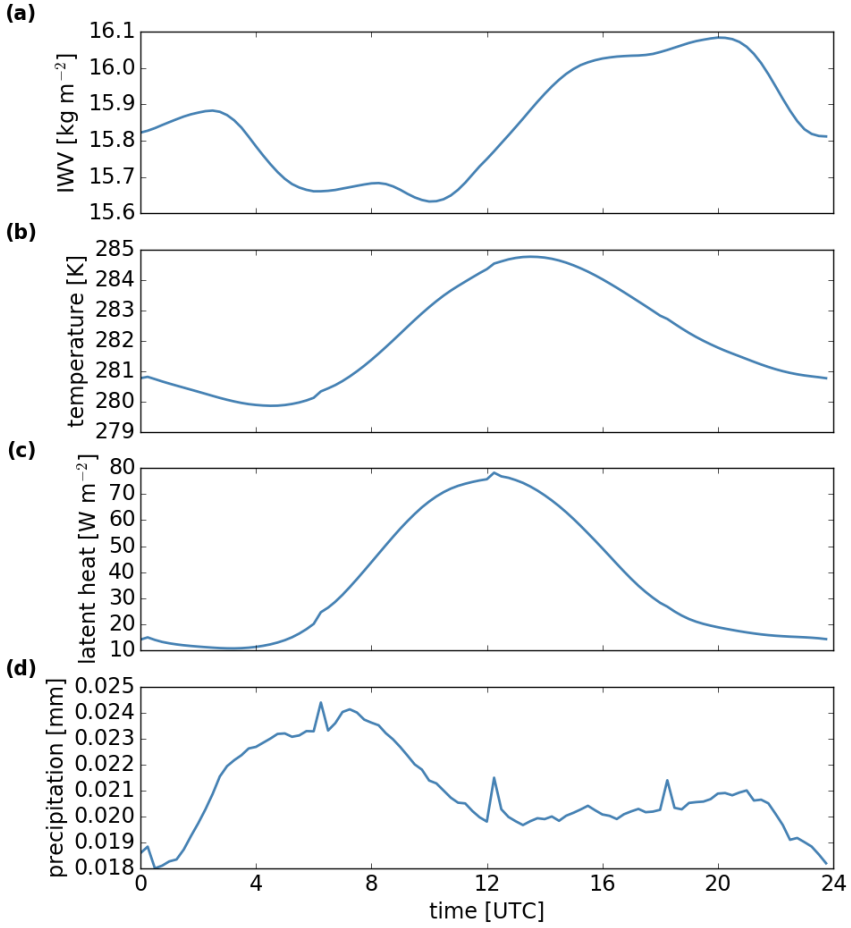

Figure 7.1: Diurnal cycle of (a) IWV, (b) temperature (2 m), (c) latent heat flux at surface, and (d) 15 min-accumulated precipitation simulated with COSMO-REA6 at nearest gridpoint to GPS stations over the years 2007-2013.

The small peaks in temperature, latent heat flux and precipitation every six hour are due to the initialisation of COSMO-REA6 at these times. The mean diurnal cycle of IWV over the years 2007–2013 has an amplitude of ca. $0.5\,\mathrm{kg\,m^{-2}}$ (3%) with a low in the morning and a maximum during the late afternoon. Temperature increases after sunrise until afternoon and decreases from then on. The Clausius-Clapeyron equation (Eq. 7.2) describes the change of water-holding capacities of the atmosphere due to a change of temperature. This influences the water storage capability of the atmosphere but not necessarily the actual IWV. Nevertheless, a correlation of 0.95 is found for temperature at 2 m height above ground and IWV (not shown). The minimum and maximum are earlier for temperature than for IWV. The latent heat flux is constant — slightly positive — during night, increases until noon and decreases afterwards. The shape of its diurnal cycle is very similar to the one of temperature since high temperatures stimulate evaporation. Precipitation peaks during the morning and is nearly constant during afternoon and early evening. Due to the relationship shown in Eq. 7.1 a positive latent heat flux increases IWV while precipitation decreases the amount of water vapour if in- and outflow are constant. To sum it up, during the morning when the on average smallest IWV occurs precipitation peaks and latent heat increases. In the afternoon and early evening, precipitation is low compared to the rest of the day and the latent heat flux decreases.

Latent heat flux is defined positive for a flow from surface to the atmosphere and negative in the opposite direction

Until now, some studies about the diurnal cycle of IWV exist. A short overview is given here. Dai et al. (2002) investigated the diurnal cycle observed by GPS over North America. They found a diurnal cycle at most of the 54 GPS stations with amplitude of 2.0–3.6 $\mathrm{kg\,m^{-2}}$ during summer and smaller amplitudes ($\leq 1.6\,\mathrm{kg\,m^{-2}}$) during the rest of the year. The diurnal cycle peaks between mid-afternoon to midnight in summer.

Note that amplitude in this thesis means the difference between minimum and maximum.

Morland et al. (2009) investigated the diurnal cycle in Bern, Switzerland and found a diurnal cycle in several data sets — microwave radiometer, GPS, ECMWF operational analysis — with a small amplitude of ca. $0.32\,\mathrm{kg\,m^{-2}}$. They focus on the influence of the temperature used for GPS observation derivation on the diurnal cycle of IWV. Since the surface air temperature, which is used to estimate the mean atmospheric temperature, exhibits much higher diurnal variations it influences the retrieved IWV. The amplitude differs only less than $0.1\,\mathrm{kg\,m^{-2}}$. However, the minimum and maximum are shifted by one or two hours to later times.

Diedrich et al. (2016) used worldwide GPS observations to investigate the daily variations of IWV. For central Europe they found amplitudes between 0.2 and $1.6\,\mathrm{kg\,m^{-2}}$ in spring and summer resulting in 3–6% in spring and 0–3% in summer. The minimum is between 4:00 and 12:00 local time (LT) with a tendency to earlier minima in spring. The diurnal cycle peaks during the second half of the day.

Furthermore, they found an increased diurnal cycle at GPS stations above 800 m AMSL and a reduced one at coastal stations.

In the following, the influence of geographic location, season, and Circulation Weather Type (CWT) are presented. Furthermore, the connection between precipitation and IWV is investigated. For these purposes, GPS observations are used as well as ERA-Interim and COSMO reanalyses. Note that the vegetation of both reanalyses does not change due to season during the whole time period. The comparison of the reanalyses with the GPS observations shows the suitability of the reanalyses for the analysis of the water cycle for which reanalyses are frequently used.

7.1 HARMONIC ANALYSIS OF DIURNAL CYCLE

The data for investigating the diurnal cycle is prepared as described in the following. First, the 15 minutely (GPS and COSMO reanalyses) or 3 hourly (ERA-Interim) data is averaged over all years (2007–2013) eventually filtered by seasons or CWT. Afterwards a harmonic analysis as described by Dai et al. (2002) is performed. The mean diurnal cycle is represented by

$$IWV(t) = IWV_0 + \sum_{n=1}^{2} S_n(t) + R \tag{7.3}$$

$$S_n(t) = \frac{1}{2} A_n \sin(nt + \sigma_n) \tag{7.4}$$

with IWV_0 is the daily mean value, t is the time, and the residual R contains the higher order harmonic oscillations of the diurnal cycle. The harmonic oscillations S_n, n=1, 2 depend on the amplitude A_n and on the phase σ_n. Note that amplitude here means the difference between maximum and minimum.

The diurnal cycles are represented by the harmonics of first and second order very well (Fig. 7.2). In general, the harmonic of the first order is dominant (Fig. 7.3). The importance of the harmonic of the second order differs. While e. g. the diurnal cycle at the station 0015 in north-east Germany is roughly point-symmetric and well represented by S_1 it is not at the station 0261 near Passau (e. g. compare Fig. 7.2a and Fig. 7.2b). Despite the more complex diurnal cycle it is well represented by the harmonics of first and second order. At most GPS stations, the Amplitude A_2 of the harmonic of the second order is less than 10% of A_1. For the diurnal cycles of the two reanalyses S_2 is more important than for the diurnal cycle of GPS. However, in any case A_2 is smaller than half of A_1 (Fig. 7.3).

The standard deviation between the fit and the averaged diurnal cycle ranges between $0.01\,\mathrm{kg\,m^{-2}}$ and $0.12\,\mathrm{kg\,m^{-2}}$, with a mean of $0.05\,\mathrm{kg\,m^{-2}}$, for all GPS stations and the COSMO reanalysis. On av-

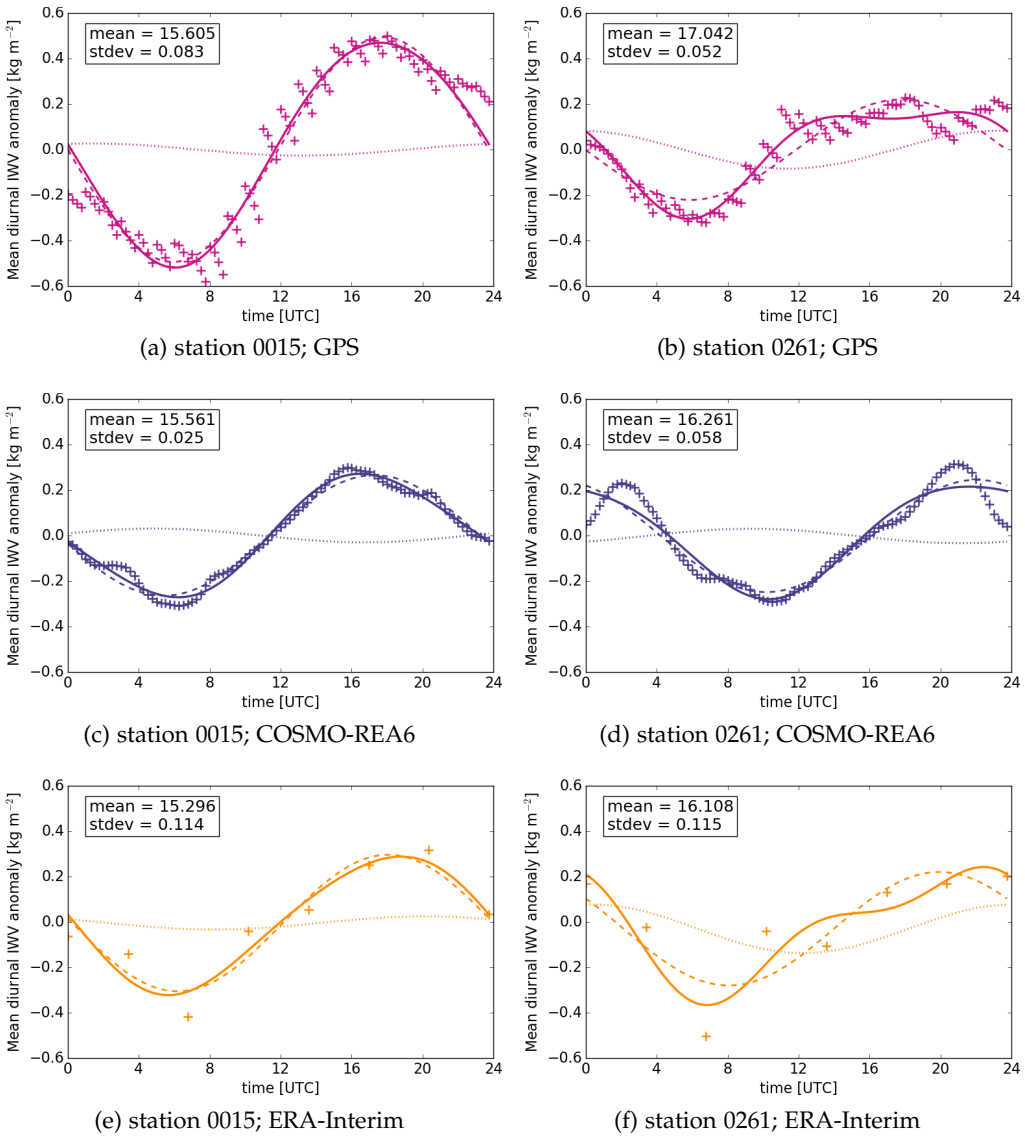

(a) station 0015; GPS

(b) station 0261; GPS

(c) station 0015; COSMO-REA6

(d) station 0261; COSMO-REA6

(e) station 0015; ERA-Interim

(f) station 0261; ERA-Interim

Figure 7.2: Mean diurnal cycles of IWV observed with GPS (pink) and simulated with ERA-Interim (orange) over the years 2007–2013 at two GPS stations in Germany: 0015 (53.2°N, 12.5°E, height AMSL: 88 m) and 0261 (48.6°N, 13.4°E, height AMSL: 377 m). The plus signs represent the original data. The harmonics S_1 and S_2 are represented by the dashed and dotted lines, respectively. The solid line is the combination of both harmonics. In the box, the mean of the respective data set and the standard deviation (stdev) between the fit and the averaged diurnal cycle are stated.

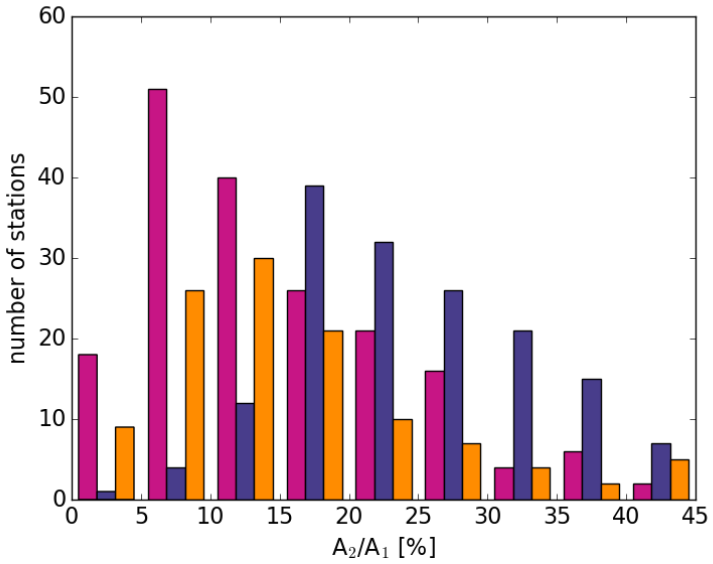

Figure 7.3: Histogram of relationship between Amplitude A_1 and Amplitude A_2 of the two harmonics (Eq. 7.3) for GPS observations (pink) and simulations with COSMO-REA6 (purple) and ERA-Interim (orange).

erage, the standard deviation is more than twice as large for ERA-Interim (0.12 kg m^{-2}) and ranges from 0.05 kg m^{-2} to 0.17 kg m^{-2}. Both, the coarser temporal resolution or poor representation of land surface processes could hamper a good fit and therefore lead to higher standard deviations.

The diurnal cycle of GPS observations (Fig. 7.2 (a) and (b)) exhibit jumps at the beginning of most full hours. As described in Sect. 2.1.2 the jumps are caused by the near-real time processing routine of the GPS retrieval at GFZ. With this retrieval, each complete hour is processed at the same time and the retrieval tend to smooth the four quaterhourly measurements.

A more detailed description of the differences of diurnal cycles and the reasons for them are given in the following sections that aim at identifying the drivers for the observed variety.

7.2 SEASONAL DEPENDENCY OF DIURNAL CYCLE

Since depending on the season the latent heat flux exhibits large differences the dependency of the diurnal cycle on seasons is assessed in the following. To eliminate the effect of differences in mean IWV in different seasons the relative amplitudes are used for this comparison (cf. Fig. 7.4).

While during summer and spring IWV exhibits a clear diurnal cycle, only small variations from the daily mean IWV can be seen

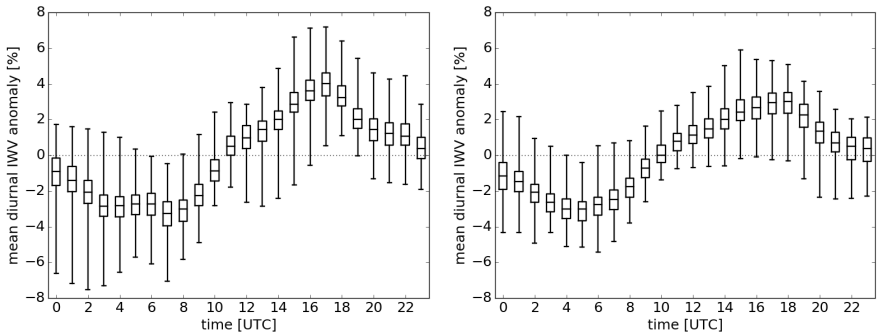

(a) Diurnal cycle in spring

(b) Diurnal cycle in summer

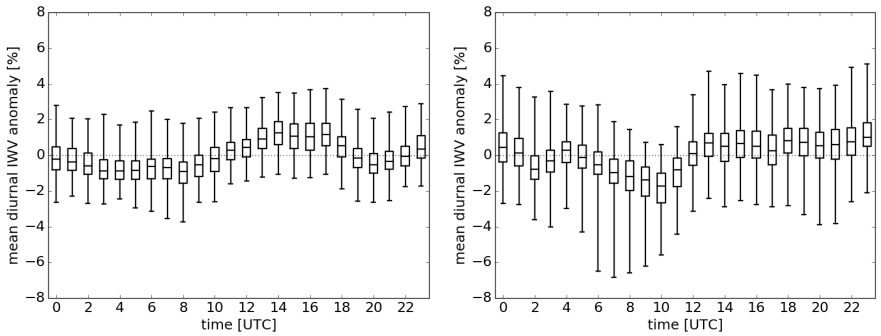

(c) Diurnal cycle in autumn

(d) Diurnal cycle in winter

Figure 7.4: The boxplots show the median (horizontal line), quartiles (box) and the maximum and minimum (whiskers) of the diurnal cycle at 183 GPS stations.

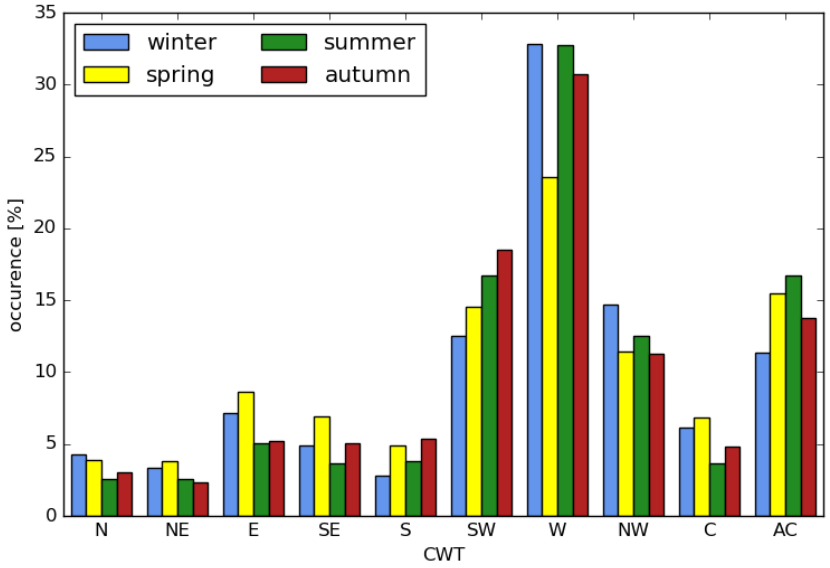

Figure 7.5: Frequency of occurrence of CWT separated into seasons.

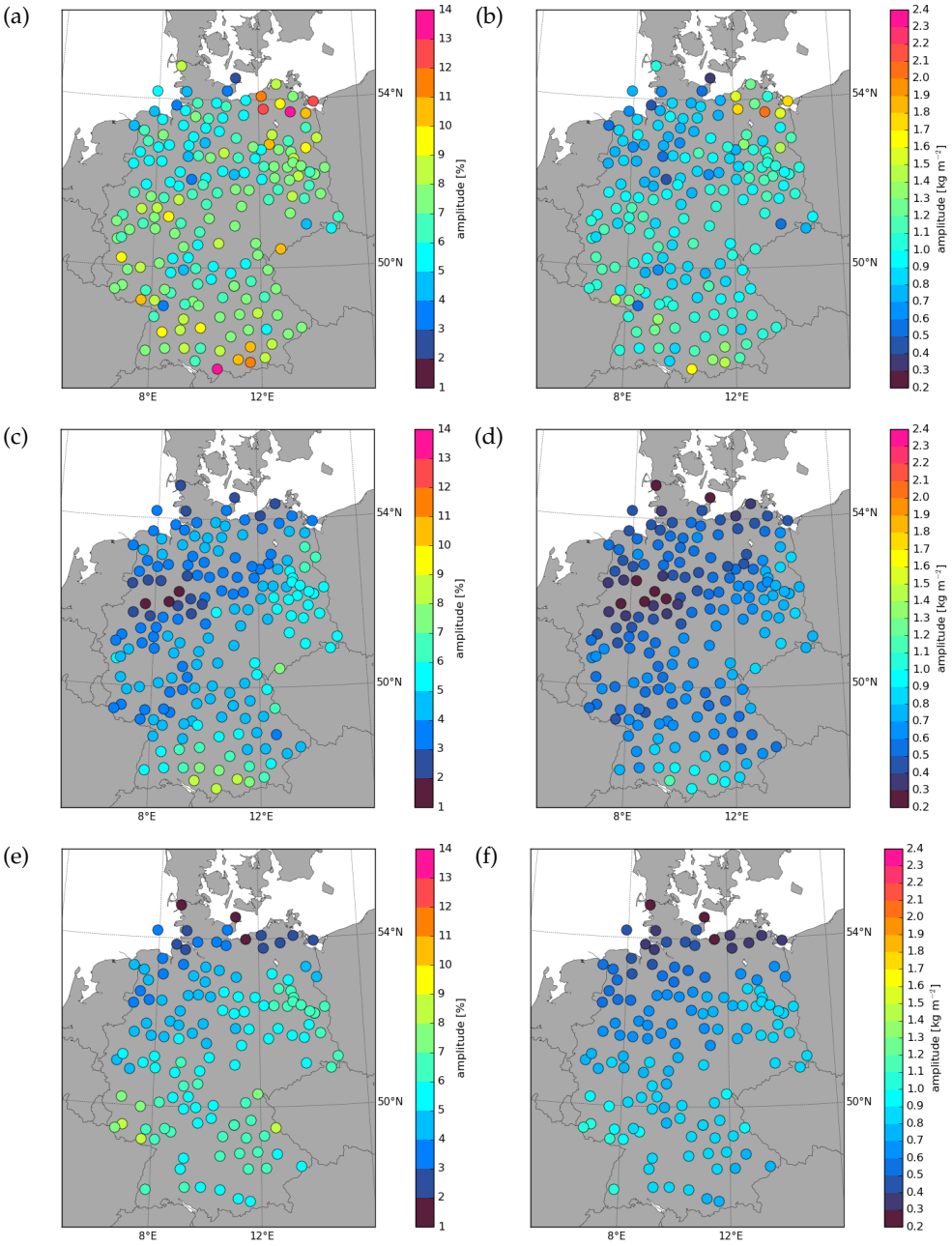

Figure 7.6: (a), (c), (e) Relative amplitude, (b), (d), (f) absolute amplitude of diurnal cycle of IWV (a)–(b) observed at 183 GPS stations and simulated with (c)–(d) COSMO-REA6 at 183 gridpoints and (e)–(f) ERA-Interim at 133 gridpoints in Germany for spring of the years 2007–2013.

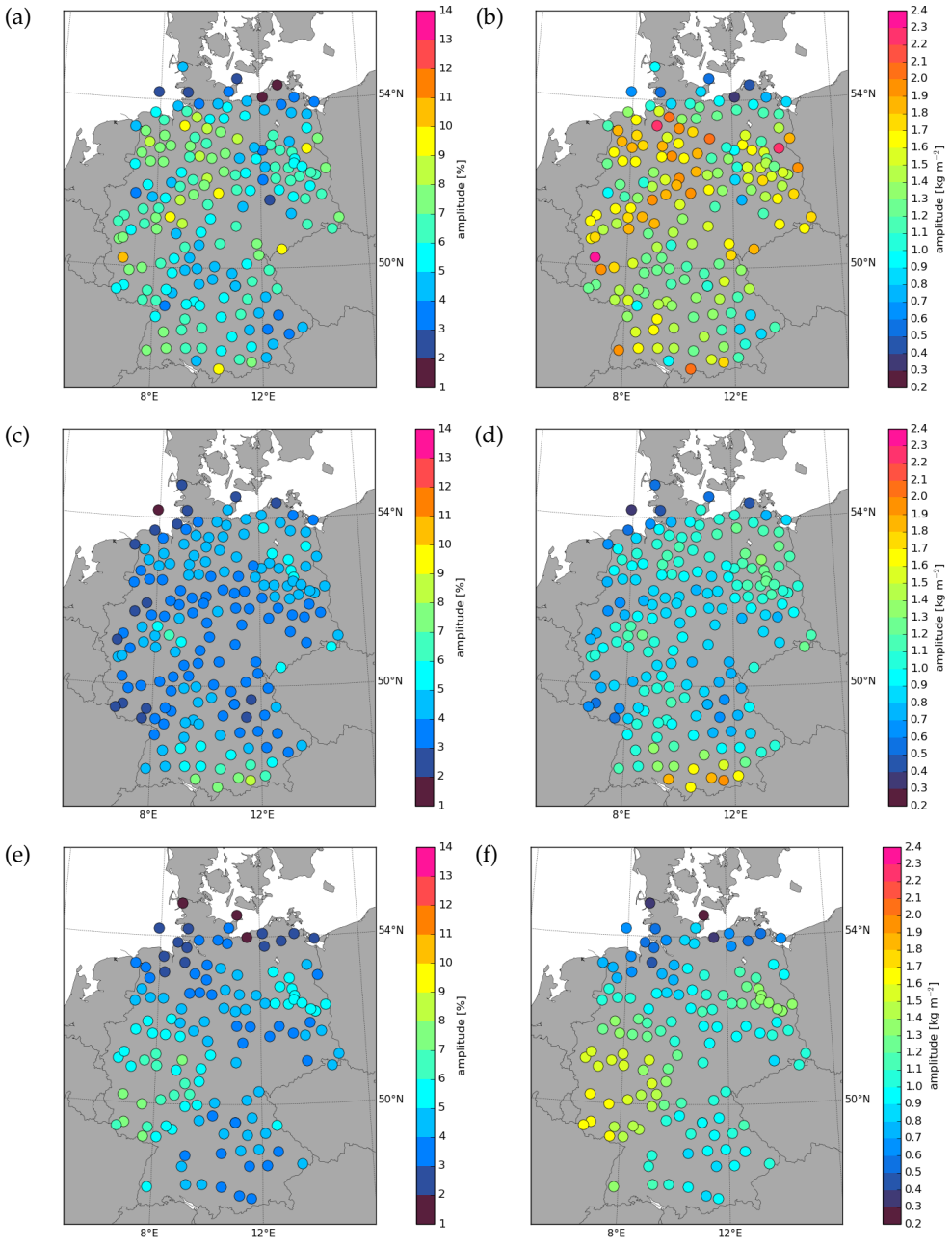

Figure 7.7: Same as Fig.7.6 but for summer.

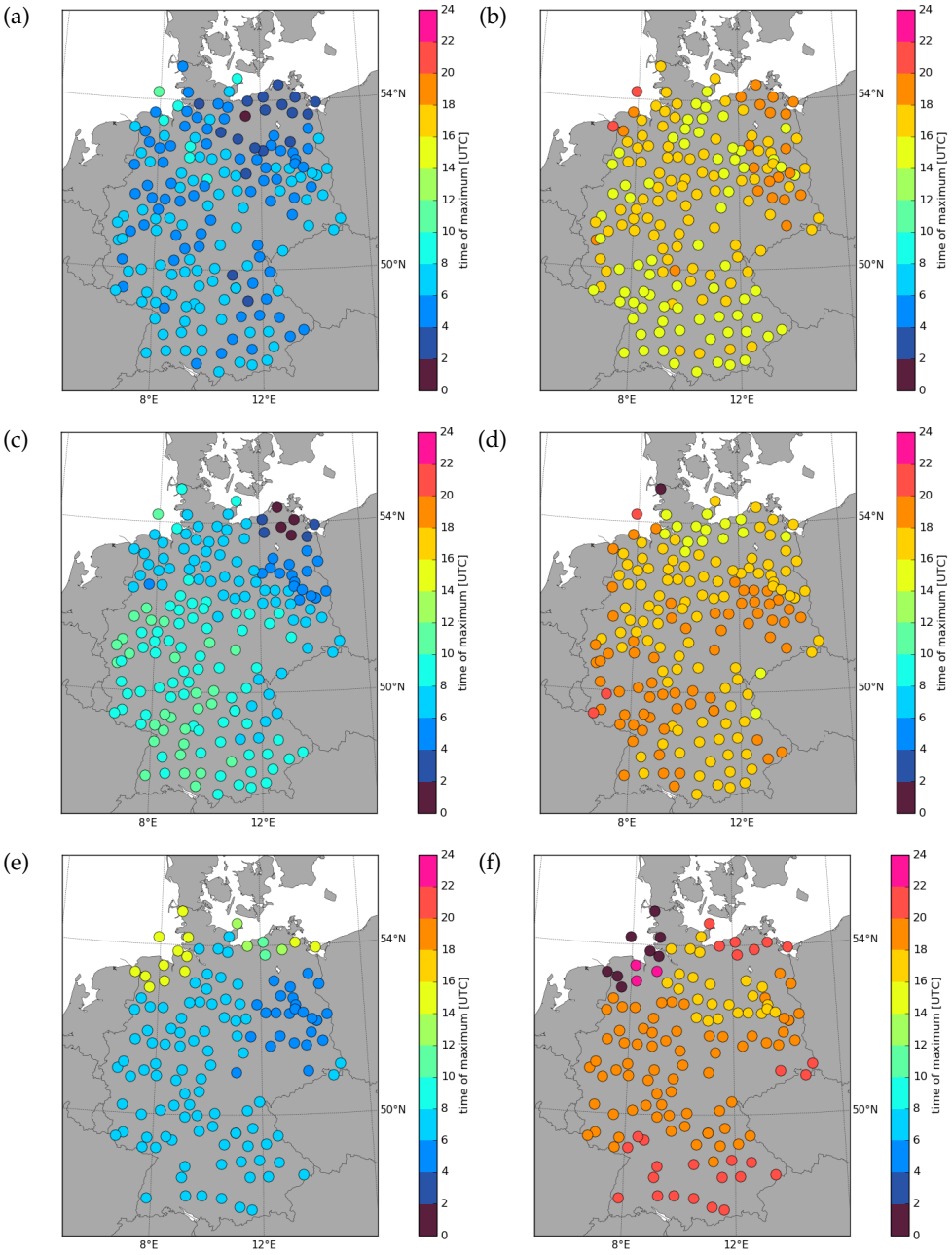

Figure 7.8: (a), (c), (e) Time of minimum, and (b), (d), (f) time of maximum of diurnal cycle of IWV (a)–(b) observed at 183 GPS stations and simulated with (c)–(d) COSMO-REA6 at 183 gridpoints and (e)–(f) ERA-Interim at 133 gridpoints in Germany for spring of the years 2007–2013.

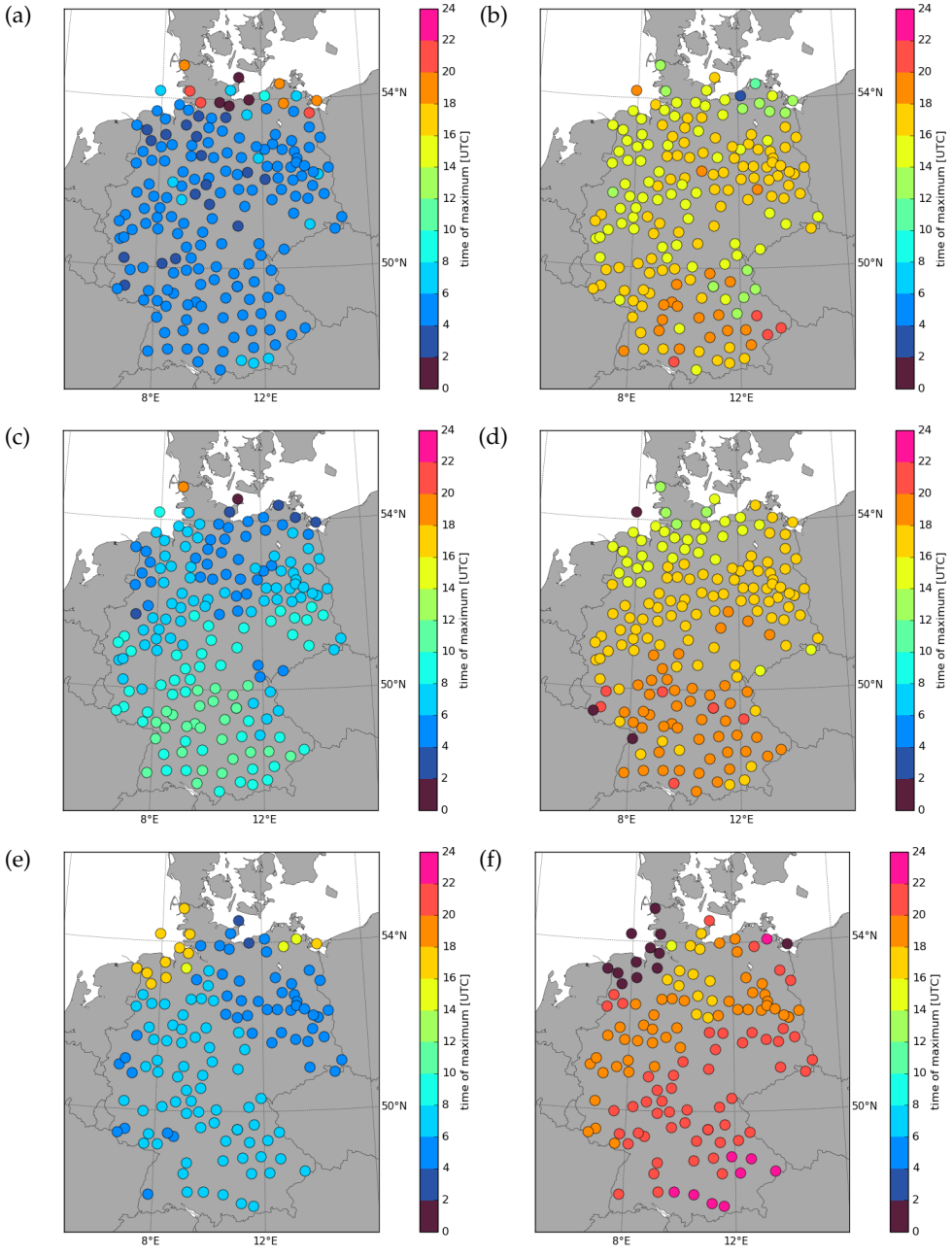

Figure 7.9: Same as Fig.7.8 but for summer.

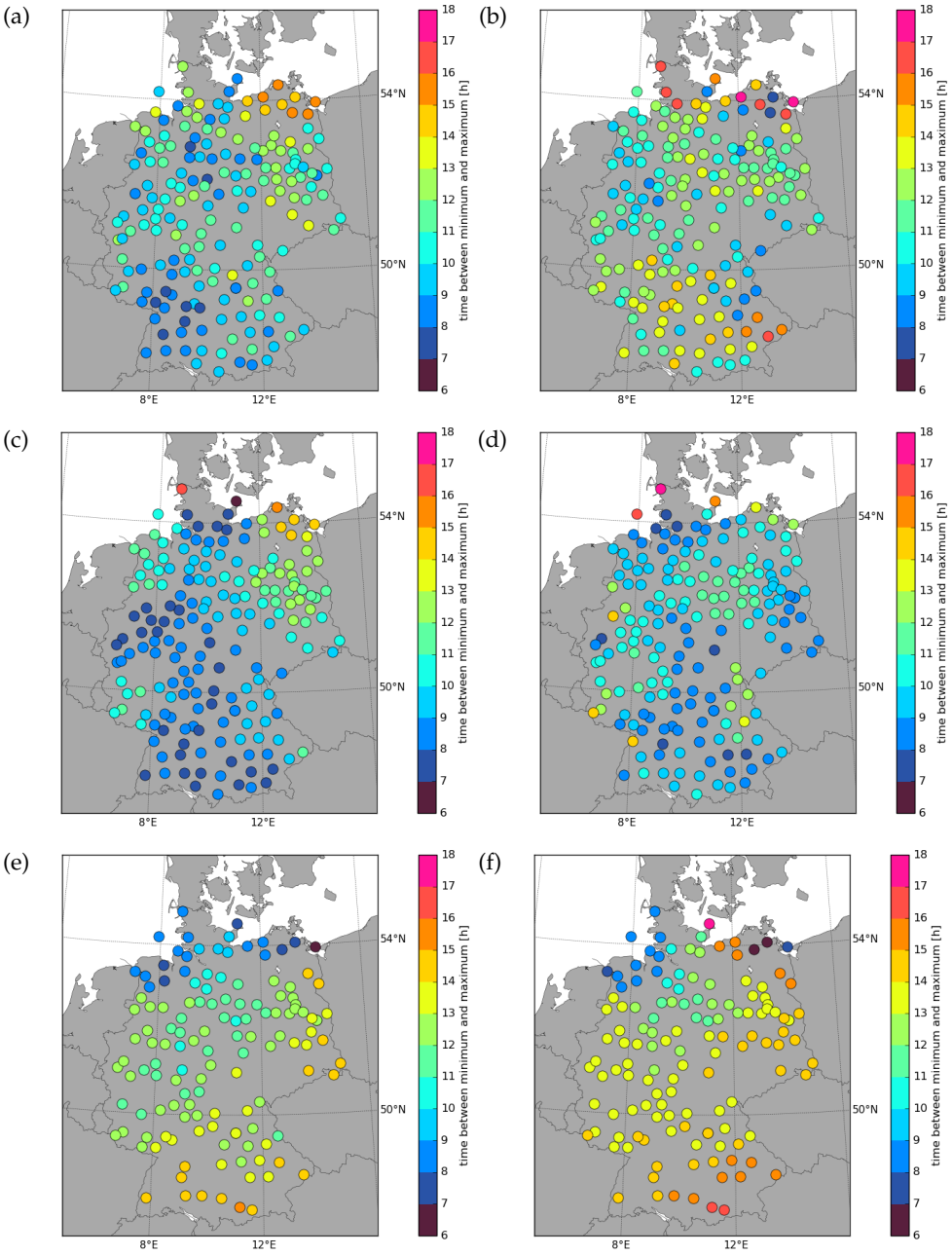

Figure 7.10: Time after minimum until maximum of diurnal cycle of IWV occurs (a)–(b) observed at 183 GPS stations and simulated with (c)–(d) COSMO-REA6 at 183 gridpoints and (e)–(f) ERA-Interim at 133 gridpoints in Germany for (a), (c), (e) spring and (b), (d), (e) summer of the years 2007–2013.

during autumn (2.2%) and winter (2.7%). In spring and summer the minimum of the median of the diurnal cycle is at 7:00 UTC and 5:00 UTC, respectively and the maximum can be seen at 17:00 UTC and 18:00 UTC, respectively. For spring and summer the amplitude is more than double the amplitude in autumn and winter: 7.3% in spring and 6.0% in summer. Additionally, the variability among the stations is large in spring and winter and smaller in summer and autumn.

Multiple factors cause these differences. First, evapotranspiration, which is the main process causing the diurnal cycle, is low during winter due to low temperatures and less transpiration of vegetation. Secondly, the weather situations dominant in autumn differ from the ones in summer and spring (cf. Fig. 7.5). In autumn westerly currents which are associated with large-scale IWV gradients dominate while in spring and summer more anticyclonic and easterly weather situations dominate which in general are not associated with strong IWV gradients. The diurnal cycle dominated by local processes is suppressed by the large-scale IWV changes in autumn. A more detailed analysis how the CWT influences the diurnal cycle is given in Sect. 7.4. The seasonal dependency of the diurnal cycle suggest further investigations only for spring and summer months which are most interesting due to their clear diurnal cycle.

Five properties of the diurnal cycle — relative and absolute amplitude, time of minimum and maximum, and time after the minimum until the maximum occur — are used to describe the diurnal cycle. In the following consideration of the regional differences of the diurnal cycle during spring and summer, ERA-Interim and COSMO-REA6 are also included in the analysis to show the suitability of the reanalyses for water cycle analysis. Since COSMO-REA6 and COSMO-REA2 does not differ significantly in their diurnal cycles of IWV, the results of COSMO-REA2 are not shown here but in Appendix C.

First the regional differences of the amplitudes are investigated. The range of amplitudes differs strongly for the three data sets. During spring, it ranges from 0.4 to 2.0 $\mathrm{kg\,m^{-2}}$ (3.0–13.7%), 0.2 to 1.1 $\mathrm{kg\,m^{-2}}$ (1.7–8.6%), and 0.2 to 1.1 $\mathrm{kg\,m^{-2}}$ (1.7–8.3%) for GPS, COSMO-REA6, and ERA-Interim, respectively. The absolute amplitudes are even higher during summer while the relative amplitudes are about the same or slightly smaller: 0.4–2.6 $\mathrm{kg\,m^{-2}}$ (1.4–12.0%), 0.4–1.9 $\mathrm{kg\,m^{-2}}$ (1.7–8.4%), and 0.3–1.7 $\mathrm{kg\,m^{-2}}$ (1.2–7.8%) for GPS observations, COSMO-REA6, and ERA-Interim simulations, respectively.

In general, the amplitude increases from north to south in spring although this pattern is much clearer in the simulations than in the GPS observations. There are some GPS stations that stick out, e. g. some north-western GPS stations that exhibit large amplitudes (cf. Fig. 7.6). These exceptions cannot be seen in the ERA-Interim and COSMO-REA6 simulations. However, in the COSMO-REA6 there are some

stations in and around the Ruhr area with comparably low amplitudes, which do not occur in ERA-Interim simulations or GPS observations. In summer, there is also a clear regional pattern in ERA-Interim amplitudes though it is slightly different than the one in spring (cf. Fig. 7.7). The coastal region exhibits the smallest amplitudes (see Sect. 7.3). An area with high amplitudes can be found around Berlin and even higher values occur in Saarland, Rhineland-Palatinate, and parts of North-Rhine Westphalia and Hesse. Besides the low amplitudes at coastal stations, this pattern cannot be seen in the GPS or COSMO-REA6 amplitudes. COSMO-REA6 amplitudes are distributed smoother than both ERA-Interim and GPS amplitudes. Especially the amplitudes of the diurnal cycle observed with GPS is diverse.

The behaviour of the diurnal cycle is described by the time of minimum and maximum. The time of the minimum is in spring and summer in the morning between 4:00 and 6:00 UTC at most GPS stations (cf. Fig. 7.8 and 7.9). For ERA-Interim it is about 1–2 h later and 1–4 h later for COSMO-REA6 for the major part of Germany. For both reanalyses, the minimum occurs ca. 2 h earlier in the East than in the west. This pattern is less clear for the GPS stations. The east-west gradient is only partly caused by an 30 min earlier sunrise and subsequently earlier solar heating, which intensifies evapotranspiration. Some northern GPS stations and COSMO-REA6 gridpoints near the coasts exhibit a minimum between 0:00 and 2:00 UTC or 18:00 to 22:00 UTC (Fig. 7.6 and 7.7). For ERA-Interim, an even larger region reaching slightly more to the south exhibit this shift to later minima (14:00–18:00 UTC). The reason for this changed diurnal cycle of coastal stations is investigated in Sect. 7.3.

In general, the time of the maximum of the diurnal cycle of GPS observations occur between 14:00 and 20:00 UTC. IWV simulated with COSMO-REA6 and ERA-Interim peaks in the periods 14:00–22:00 UTC and 16:00–23:00 UTC, respectively. All data sets have a tendency of later peaks in the summer (cf. Fig. 7.8 and 7.9). However, some GPS station exhibit the opposite behaviour. As for the minimum, in coastal regions the diurnal cycle can peak at different times (Section 7.3). In ERA-Interim a north-south gradient can be found with earlier peaks in the north. COSMO-REA6 exhibits a similar pattern. This cannot be seen in GPS. The geographic pattern in the maxima and minima of the diurnal cycle simulated with the reanalyses is presumably due to the fact that the diurnal cycle of the models is dominated by the solar heating while more locally variable factors as surface type, soil moisture, vegetation, or height which influences the observed diurnal cycle of IWV cannot vary as much in the model as in reality. This lead to a smoother regional distribution in the reanalyses than in the observations.

The length of diurnal cycle is here defined as the time after the minimum until the maximum occur. As described above, there is an east-west gradient in the time of the minimum and a north-south gradient for the time of the maximum in the diurnal cycle simulated with ERA-Interim. The combination of these two patterns leads to an increase from north-west to south-east in the length of the diurnal cycle from 7 h to 17 h (cf. Fig. 7.10). In general, it is longer in summer than in spring. The diurnal cycle measured at GPS stations and simulated with COSMO-REA6 exhibits different regional patterns as found for ERA-Interim. In spring it is longer in the north-east and shorter in the south-west for both GPS and COSMO-REA6. The length of the diurnal cycle simulated with COSMO-REA6 does only change slightly in summer. Depending on the region it increases or decreases by about 1 h. For the GPS observations, the summer is associated with an strong increase in length at most southern stations and a slighter increase at northern stations. This leads to a more diverse pattern during these months. The increase of the length in summer is most likely influenced by the longer duration of sunshine in summer and therefore enhanced solar heating and increased evaporation.

7.3 DEPENDENCY OF DIURNAL CYCLE ON GEOGRAPHIC LOCATION

One factor that influences the diurnal cycle is the geographic location. Here, the influence of the North Sea and the Baltic Sea is investigated as well as the influence of the height on the diurnal cycle.

As described in Sect. 7.2 the diurnal cycle in coastal regions differs from the one in the other parts of Germany. The relative and absolute anomalies of the diurnal cycle at the GPS stations near the sea tends to be smaller than the amplitudes of the other stations especially during summer (cf. Fig. 7.6 and 7.7). The reason for that is probably the lower difference between day and night temperatures in coastal regions especially during summer and the constant availability of moisture. Therefore, in contrast to non-coastal regions where there is nearly no latent heat flux during night smaller differences in evaporation between day and night occur in coastal regions. For ERA-Interim a larger region is affected by this effect. A much stronger difference between GPS observations and ERA-Interim at the coast can be seen in time of minimum and time of maximum. ERA-Interim shows a 4–10 h (spring) later minimum of diurnal cycle and a 4–6 h later maximum than in the other parts of Germany. At the North Sea the effect is larger than at the Baltic Sea. For GPS stations this effect is much smaller. The reason for this shift of the diurnal cycle is the so-called sea/land breeze effect. During the day the land heats faster than the sea. Subsequently, the air rises over land and sinks above the sea. This leads to an onshore wind near the surface transporting

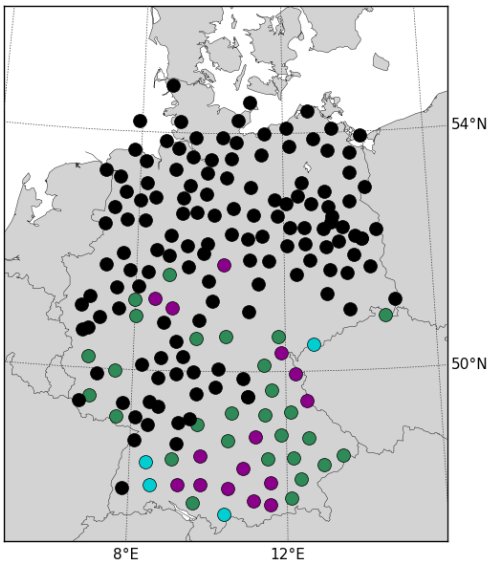

(a) Map of GPS stations

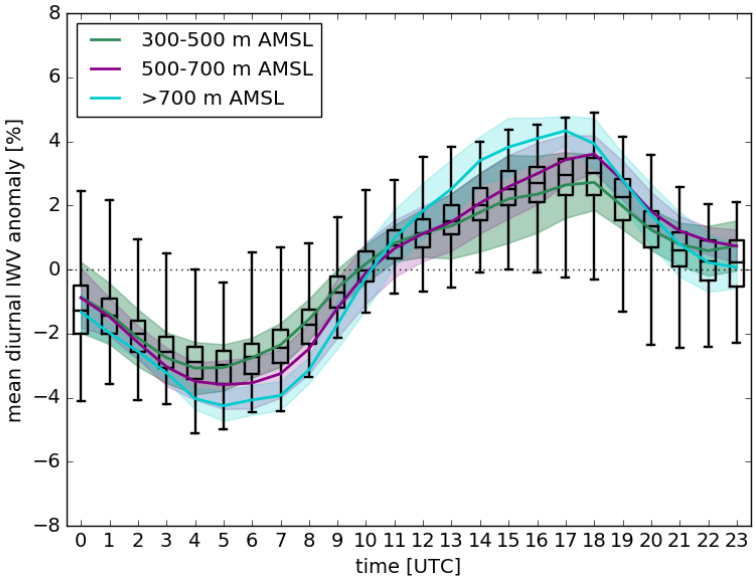

(b) Diurnal cycle of GPS stations at different height levels.

Figure 7.11: (a): GPS stations at a height of 300–500 m AMSL (green), 500–700 m AMSL (purple), and above 700 m AMSL (turquoise), and all other stations (black). (b): Mean diurnal anomaly in percent of mean IWV at GPS stations shown in the map above. The shaded areas represent the standard deviation of the diurnal anomalies within each height class. The boxplots show the median (horizontal line), quartiles (box) and the maximum and minimum (whiskers) at the other stations.

humid air towards the land. Therefore humidity peaks in the afternoon over land. During night, land cools faster than the sea and due to this stronger cooling the large scale convection changes its direction which leads to offshore winds and a peak of IWV during night over sea. Jakobson et al. (2014) found different times for minimum and maximum of diurnal cycle in simulated IWV above the Baltic Sea than over the surrounding land as a result of the sea/land breeze effect. Over sea, the minimum occurs between 0:00 and 6:00 UTC while the maximum within the time period 12:00–18:00 UTC. Above land it is the opposite: the minimum occur between 12:00 and 18:00 UTC and the diurnal cycle peaks between 0:00 and 6:00 UTC. The minima and maxima of diurnal cycles near the coast simulated with ERA-Interim matches the times found by Jakobson et al. (2014) over sea. Due to the coarse resolution of ERA-Interim the distinction between sea and land does not match the reality near the coast and the model is likely much more influenced by the sea than the corresponding GPS stations and COSMO-REA6 gridpoints are.

The height of the station also has an influence on the diurnal cycle. With increasing height the amplitude of the diurnal cycle increases (Fig. 7.11). Between 300 m and 500 m AMSL the diurnal cycle corresponds with the median of the diurnal cycle of stations below 300 m. Between 300 m and 500 m the amplitude is about 1 percentage larger and more than 2 percentage larger above 700 m. The variability in each height is highest during the maximum in the afternoon, especially within the height range of 300–500 m.

Similarly, Diedrich et al. (2016) found a higher amplitude of diurnal cycles at worldwide GPS stations above 800 m. However, they also found a distinct temporal shift in the diurnal cycle of high stations. There is only a slight shift in the same direction, meaning later occurrence of minimum and maximum, in the diurnal cycle in this study. This difference is most likely due to the fact that the high stations worldwide are between 800 m and 3600 m while here the maximum height is 907 m AMSL.

One factor of the increased relative diurnal cycle is probably the lower mean IWV at high stations. Another reason could be the higher variability in temperature which results from enhanced warming of the slope during daytime and enhanced cooling during nighttime. Furthermore, circulation between mountain and valley usually observed during fair weather conditions can enhance the diurnal cycle. Solar heating during daytime leads to an upslope wind which transports moist air originating from the valley to higher regions and during night the cooling induces wind in the opposite direction.

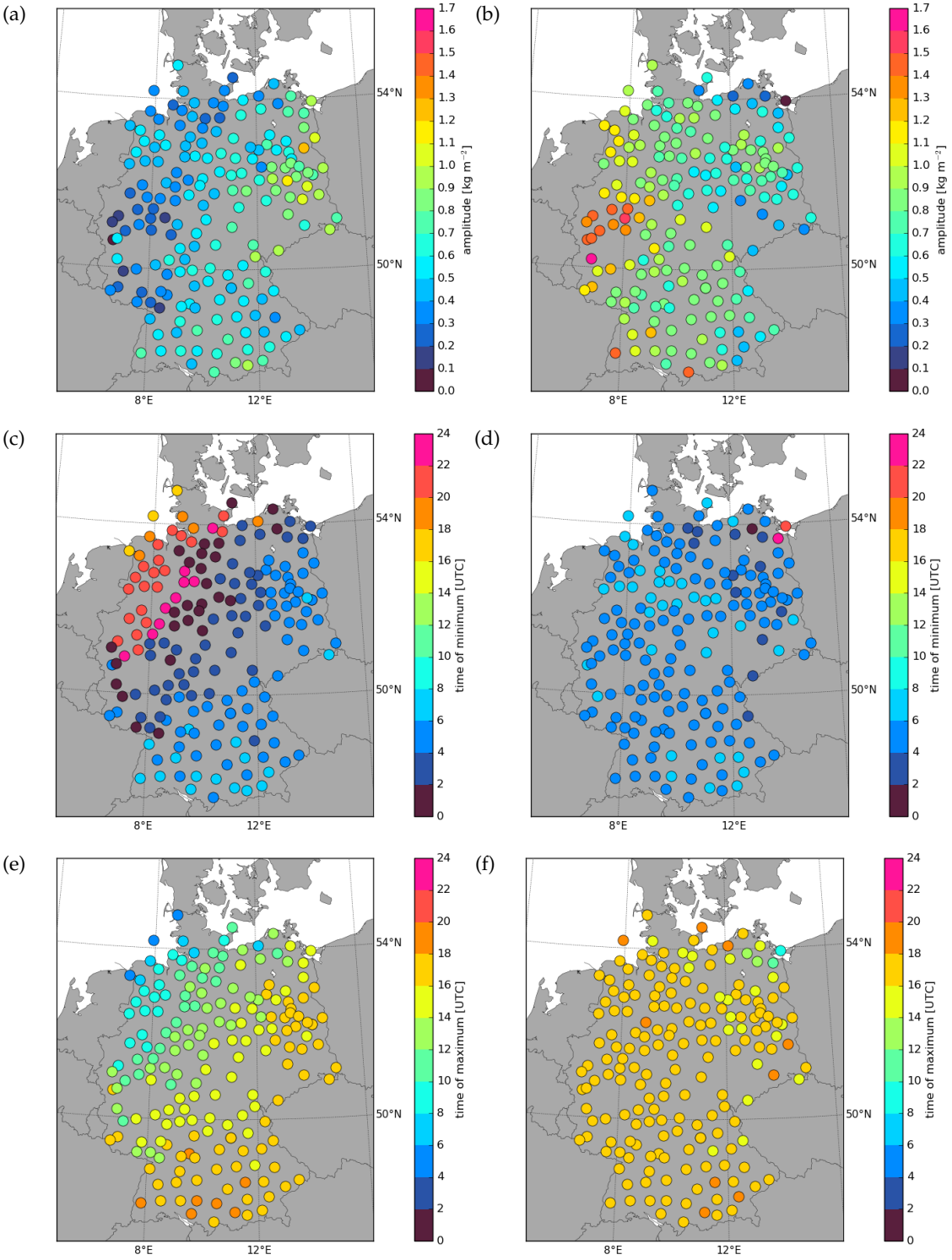

Figure 7.12: (a)–(b) Amplitude, (c)–(d) time of maximum, and (e)–(f) time of minimum of diurnal cycle of IWV at 183 GPS stations in Germany for the years 2007–2013 divided into two CWT classes: (a), (c), (e) class I includes western and cyclonic and (b), (d), (f) class II includes eastern and anticyclonic weather situations.

7.4 DEPENDENCY OF DIURNAL CYCLE ON WEATHER SITUATION

Here the dependency of the diurnal cycle on the CWT is investigated. For the CWTs classification see Sect. 5.1.2. Here, it is distinguished between two CWT classes. Class I includes western (south-western, western, north-western) and cyclonic weather situation while class II includes the eastern (northern, north-eastern, eastern, south-eastern, south) and anticyclonic weather situations. The division into two classes is conducted because only days with a weather situation which last for the whole day is included in this comparison. A finer separation would lead to a too small dataset. Cyclonic and anticyclonic CWTs are assigned due to their cloud cover similar to the according CWT class (Akkermans et al., 2011).

The diurnal cycle of class II exhibits higher amplitudes than the one of class I. The weather situations in class II are associated with higher amplitudes in the West than in east. The opposite distribution is found for diurnal cycles of class I. Strong differences occur in the time of minimum and maximum. While for class II the time of maximum (16:00–18:00 UTC) and the time of minimum (2:00–6:00 UTC) does vary very slightly from station to station, there is a strong regional dependency for class I CWTs. The minimum occurs in north-west at 16:00 UTC and in south-east at 8:00 UTC. The maximum occurs at 6:00 UTC at the north-western stations and at 20:00 UTC at the southern GPS stations.

The differences in amplitude are most likely due to the transport of humid air mass which interfere the evolution of a diurnal cycle due to local processes. The western regions are more influenced by this moisture transport than the stations in eastern Germany.

7.5 RELATIONSHIP BETWEEN DIURNAL CYCLE OF IWV AND DIURNAL CYCLE OF PRECIPITATION

The connection between the diurnal cycle of precipitation and IWV was assessed by previous studies as described in the following. Dai et al. (2002) analysed the diurnal cycles of IWV observations with GPS and precipitation from hourly rain gauge measurements at locations in North America between June and August of four years. At most locations they found weak or little correlation between diurnal variations of IWV from GPS observations and precipitation from 5 minutely tipping-bucket rain gauge measurements at one location in Aubière, France over five years. They assume that the precipitation is a source for water vapour which leads to an increase in IWV due to evaporation during precipitation. In contrast to that, Labbouz et al. (2015) found that the precipitation peaks on average 20 min after the IWV maximum in 78% of their cases at midlatitude sites. However, the surface mixing ratio peaks after the precipitation maximum in

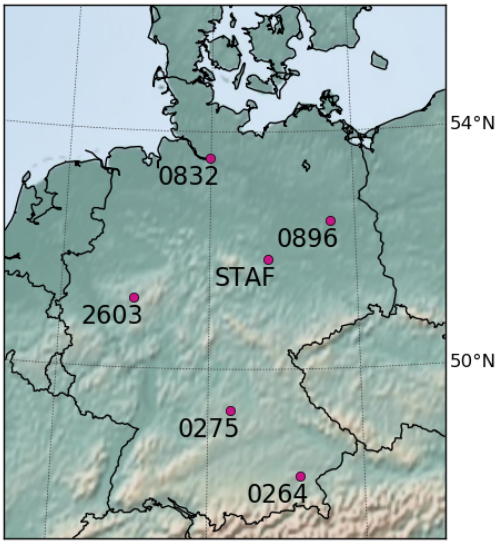

Figure 7.13: GPS stations used for Fig. 7.14 and 7.15.

60% of their cases. From the relationship shown by Eq. 7.1 in combination with the results of the two studies, it can be concluded that the convergence of low level moisture which usually leads to precipitation increases IWV. The precipitation itself is a sink of IWV and therefore reduces the amount of water in the atmosphere. This leads to a peak in IWV shortly before precipitation peaks. However, precipitation increases the availability of water as a source of evaporation. This explains the peak of surface mixing ratio after the peak of precipitation found by Labbouz et al. (2015). This increased evaporation cannot compensate the reduction of water vapour through precipitation. Therefore, IWV is still reduced after precipitation and peaks in contrast to the surface mixing ratio before the peak of precipitation.

Here, the connection between the diurnal cycle of precipitation and the diurnal cycle of IWV is investigated at six GPS stations (Fig. 7.13). For this purpose, 1-hourly accumulated rain gauge measurements are used. Due to the extreme variability of precipitation, its diurnal cycle is less smooth than the one of IWV. Therefore, for each GPS station, the 2–3 nearest rain gauge measurements within a maximum range of 10 km are averaged.

In general, positive anomalies of the diurnal cycle of IWV are associated with positive anomalies of precipitation and vice versa (Fig. 7.14 and 7.15). Both diurnal cycles peak in the afternoon and hit a low in the morning. However, there are some exceptions (e. g. Fig. 7.15 (c)). A difference between spring and summer cannot be found in this dataset.

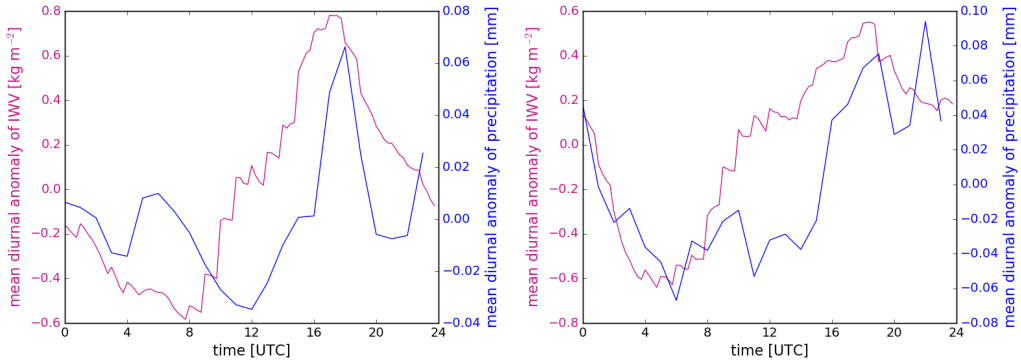

(a) spring; 0264

(b) summer; 0264

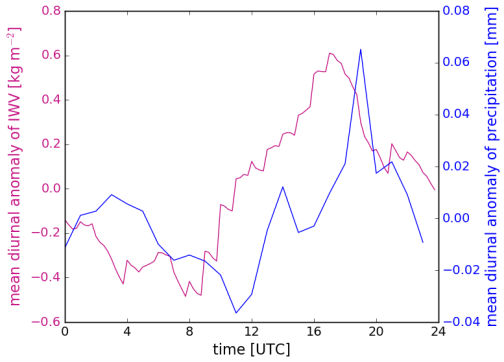

(c) spring; 0275

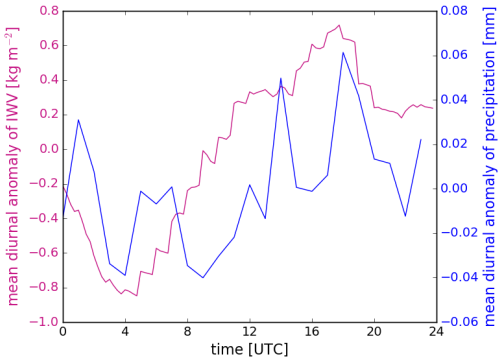

(d) summer; 0275

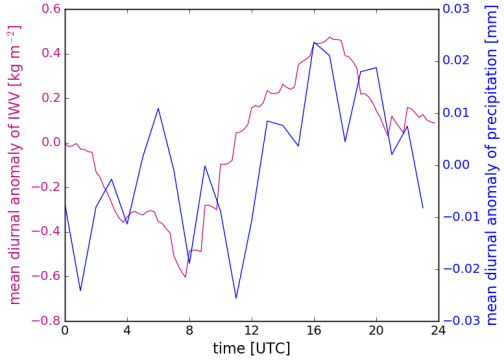

(e) spring; 0832

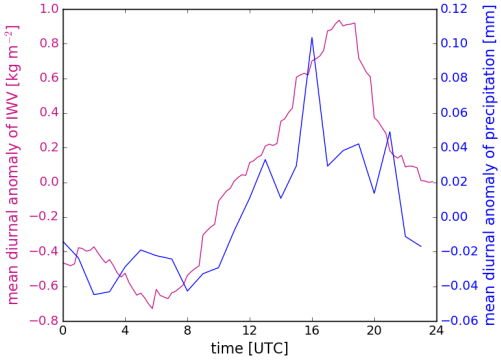

(f) summer; 0832

Figure 7.14: Mean diurnal anomaly of IWV and 1 h accumulated precipitation for spring (left column) and summer (right column) at the GPS stations 0264, 0275, and 0832 for the years 2007–2013. See Fig. 7.13 for the location of the stations.

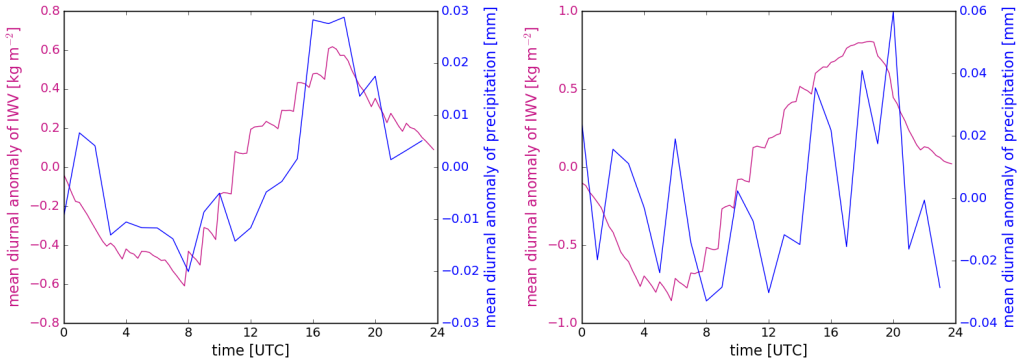

(a) spring; 0896

(b) summer; 0896

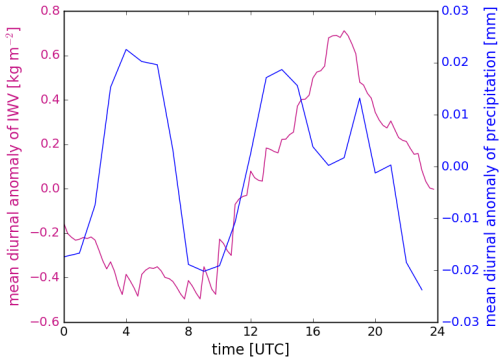

(c) spring; 2603

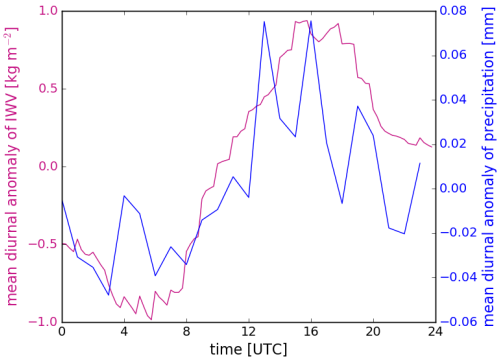

(d) summer; 2603

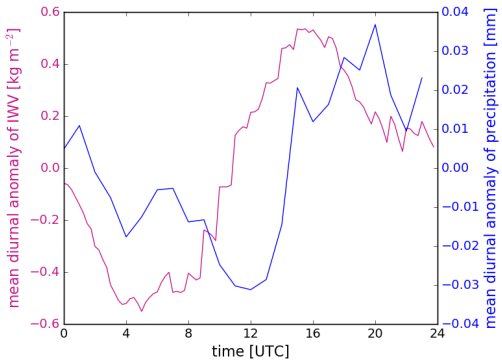

(e) spring; STAF

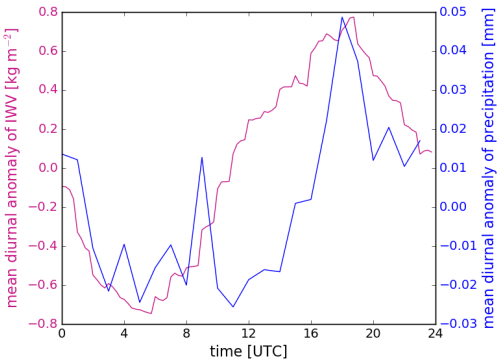

(f) summer; STAF

Figure 7.15: Mean diurnal anomaly of IWV and 1 h accumulated precipitation for spring (left column) and summer (right column) at the GPS stations 0896, 2603, and STAF for the years 2007–2013 . See Fig. 7.13 for the location of the stations.

This study is only a first approach to find the connection between IWV and precipitation. Since precipitation is even more variable than IWV and therefore does not exhibit a clear diurnal cycle, longer time periods could be helpful. Furthermore, a higher resolution of the observations could enable an advanced assessment of the temporal relationship between both atmospheric parameters. Additionally, a separation in different precipitation regimes could improve the analysis.

7.6 SUMMARY AND CONCLUSIONS

Since spring and summer exhibit a clear diurnal cycle of IWV, five properties of the diurnal cycle — relative and absolute amplitude, time of minimum and maximum, and time after the minimum until the maximum occur — are used to investigate the differences between the mean diurnal cycle of IWV observed with GPS and simulated with COSMO-REA6 and ERA-Interim. In summer the absolute amplitude is slightly larger than in spring while it is the opposite for the relative amplitude. The diurnal cycle of GPS observations exhibits higher amplitudes as well as a higher variability in its amplitudes compared to the two reanalyses. The amplitudes vary between 0.4 and 2.0 $\mathrm{kg\,m^{-2}}$ (3.0–13.7%) in spring and 0.4–2.6 $\mathrm{kg\,m^{-2}}$ (1.4–12.0%) in summer for GPS. Compared to the diurnal cycle of GPS observations, the highest amplitudes in the reanalyses are nearly 1 $\mathrm{kg\,m^{-2}}$ (4–5%) smaller while the smallest amplitudes are about the same size.

In general, the minimum of the diurnal cycle occurs in the morning (4:00 and 10:00 UTC) and the maximum occurs between 14:00 and 23:00 UTC depending on the data set. The reanalyses exhibit a regional pattern: the time of the minimum is shifted to later times from east to west and a north-west gradient is found in the time of the maximum with earlier peaks in the north. The diurnal cycle observed with GPS shows a much diverse pattern.

The influence of two regional characteristics is investigated. In coastal regions the amplitude of the diurnal cycle is reduced and shifted due to the land/sea-breeze effect. The diurnal cycle of IWV is enhanced at high altitudes and maximum and minimum are shifted to later times.

A temporal connection between IWV and precipitation in summer and spring is found. High IWV values in the afternoon come along with high precipitation. A more detailed investigation is needed. An extended time series with a higher temporal resolution can help as well as a more detailed look at separate events.

This analysis suggests that the diurnal cycle is an appropriate tool for the investigation of the water cycle. Its dependency on seasons, regions, and weather situations could indicate differences in processes of the hydrological cycle.

8

TRENDS IN IWV

Long-term trends in water vapour are important for climate monitoring due to two main reasons. First, a warming of the atmosphere will result in a strong positive feedback from water vapour (Bony et al., 2006). This is induced by the approximately exponential increase in saturation water vapour pressure when temperature increases described by the Clausius-Clapeyron equation 7.2. In combination with the strong absorption of water vapour in most parts of the longwave spectrum, this results in an amplification of the climate response on atmospheric warming.

Second, an increased amount of water vapour is expected to cause changes in the strength of the hydrological cycle ($E - P$) (Held and Soden, 2006). The strength of the hydrological cycle increases proportionally to the lower-tropospheric water vapour. This leads to an increase in moisture in wet regions and a decrease in dry regions.

Here, trends in IWV within a time period of 19 years (1995–2013) are analysed. For this time period data from the reanalysis COSMO-REA6 is available. Additionally, IWV from ERA-Interim, which is available for an even much longer time period (1979–until now), is used. For a shorter time period (2007–2013), the trends of the two reanalyses are compared to the trends analysed in IWV simulated with the more highly resolved COSMO reanalysis COSMO-REA2 as well as to the trends in IWV derived from GPS observations. The last two data sets are only available for the shorter time period of seven years. These four data sets are used to analyse trends in IWV.

In the following, the method to decompose the IWV time series and retrieve the long-term trend is described. Afterwards trends analysed in the four data sets are compared focusing on regional differences.

8.1 DECOMPOSITION OF TIME SERIES

The decomposition and trend analysis of the IWV time series is described in the following (e. g. Morland et al., 2009). The IWV time series is decomposed in a constant term, a trend, and a seasonal term represented by a series of cosine and sine harmonics (cf. Fig. 8.1):

$$\begin{aligned} IWV(t) = {} & x_1 + x_2 t \\ & + x_3 \cos(\omega_1 t) + x_4 \sin(\omega_1 t) \\ & + x_5 \cos(\omega_2 t) + x_6 \sin(\omega_2 t) \\ & + x_7 \cos(\omega_3 t) + x_8 \sin(\omega_3 t) + n(t) \end{aligned} \tag{8.1}$$

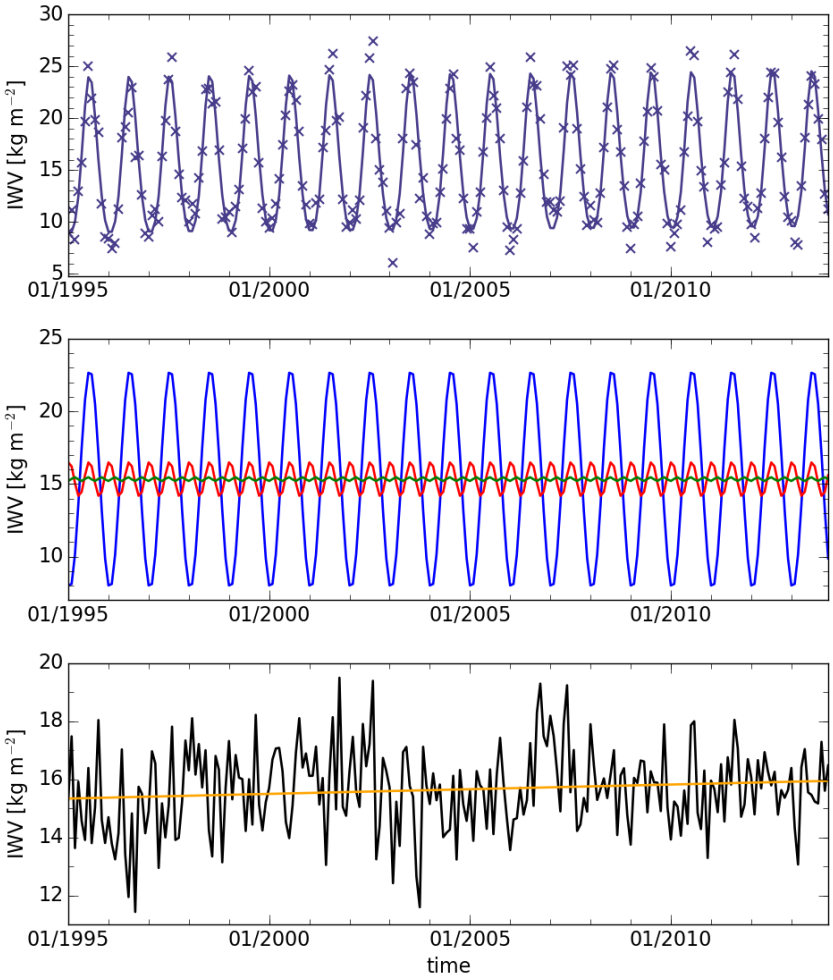

Figure 8.1: top: monthly means of IWV simulated with COSMO-REA6 (crosses) and fit (solid line); middle: annual (blue), semi-annual (red), and tre-annual (green) cosine and sine functions of the decomposition; bottom: monthly means of IWV minus annual, semi-annual, and tre-annual cosine and sine functions of the decomposition (black), and trend (orange)

with t is the time and $n(t)$ is the noise. The frequencies of the annual, semi-annual, and tre-annual cosine and sine functions are represented by $\omega_i = 2\pi i/(1\,yr)$, $i = 1,2,3$. The trend is represented by x_2. To solve this equation the least squares analysis is applied to this equation. First, the equation 8.1 is written in a matrix formulation:

$$\mathbf{IWV} = \mathbf{A} \cdot \mathbf{X} + \mathbf{N} \tag{8.2}$$

where $\mathbf{N}$ is the vector of noise that cannot be described by the decomposition and $\mathbf{IWV}$ is a vector which entries here represent the monthly means of IWV. The temporal resolution used for the vector $\mathbf{IWV}$ does not influence the trend significantly. $\mathbf{A}$ is the matrix that describes the decomposition:

$$\mathbf{A} = \begin{pmatrix} 1 & t_1 & \cos(\omega_1 t_1) & \sin(\omega_1 t_1) & \cos(\omega_2 t_1) & \sin(\omega_2 t_1) & \cos(\omega_3 t_1) & \sin(\omega_3 t_1) \\ 1 & t_2 & \cos(\omega_1 t_2) & \sin(\omega_1 t_2) & \cos(\omega_2 t_2) & \sin(\omega_2 t_2) & \cos(\omega_3 t_2) & \sin(\omega_3 t_2) \\ \vdots & \vdots & \vdots & \vdots & \vdots & \vdots & \vdots & \vdots \\ 1 & t_n & \cos(\omega_n t_n) & \sin(\omega_1 t_n) & \cos(\omega_2 t_n) & \sin(\omega_2 t_n) & \cos(\omega_3 t_n) & \sin(\omega_3 t_n) \end{pmatrix} \tag{8.3}$$

To solve this equation, noise is assumed to be neglectable and the solution vector $\mathbf{X}$ can be derived by solving the equation:

$$\mathbf{X} = (\mathbf{A}^\mathsf{T} \cdot \mathbf{A})^{-1} \cdot \mathbf{A}^\mathsf{T} \cdot \mathbf{IWV} \tag{8.4}$$

The annual harmonics is the most distinct part of the decomposition while the semi-annual and tre-annual harmonics have much smaller amplitudes (Fig. 8.1; middle). The remaining noise is small in contrast to the overall variability. Since the aim is to retrieve the trend the use of annual, semi-annual, and tre-annual cosine and sine functions to decompose the time series of monthly means is sufficiently.

8.2 IWV TRENDS

The trends of gridpoints near GPS stations of the reanalyses COSMO-REA6 and ERA-Interim, which are available for the period of 19 years (1995–2013), are calculated (Fig. 8.2). The mean positive trend is higher for COSMO-REA6 ($0.32\,kg\,m^{-2}$ per decade) than for ERA-Interim ($0.21\,kg\,m^{-2}$ per decade). The mean trend of COSMO-REA6 is higher than all the trends found in ERA-Interim at the gridpoints in Germany (Fig. 8.3). However, in both reanalyses slightly similar regional differences can be found. For COSMO-REA6 trends increases from north-west to south-east, while for ERA-Interim the lowest trends are in the western part of Germany and increase slightly

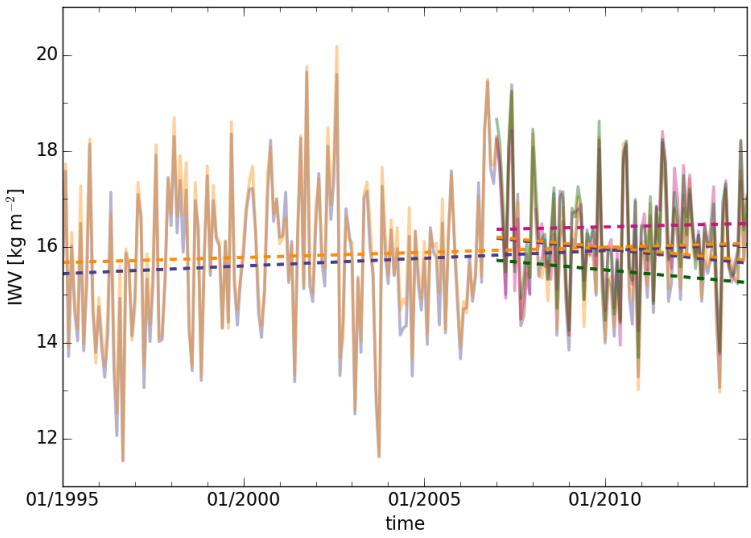

Figure 8.2: Solid lines as in the bottom panel of Fig. 8.1 for ERA-Interim (orange), COSMO-REA6 (purple), COSMO-REA2 (green), and GPS (pink). Dashed lines represent the trends for the time period 1995–2013 (long lines) and 2007–2013 (short lines).

to the east (Fig. 8.4). The differences between both reanalyses are unexpected since COSMO-REA6 is driven by ERA-Interim and the different resolutions should not have an impact on trends, which occur on large temporal scales. A possible explanation will be given later.

Since COSMO-REA2 and GPS observations are available for the time period 2007–2013, trends of COSMO-REA6 and ERA-Interim are also analysed for this shorter time period The trends of all three reanalyses are negative, -0.73, -0.67, and $-0.69\,\mathrm{kg\,m^{-2}}$ per decade for COSMO-REA2, COSMO-REA6 and ERA-Interim, respectively. The mean trend of the GPS observations ($0.25\,\mathrm{kg\,m^{-2}}$ per decade) is positive and is more similar to the trends found for the longer time period.

These results must be interpreted with caution because of the lack of analysis of homogeneity of the data sets. Schröder et al. (2016) emphasises the importance of such an analysis, which is conducted within GEWEX water vapor assessment (G-VAP). The main objective of G-VAP is to analyse and explain strengths and weaknesses of satellite-based data records of water vapour through intercomparisons and comparisons with ground-based data. Within this scope, they found several discontinuities in data records. They assume these discontinuities are a main factor for the disparity of trends in the investigated data sets. ERA-Interim exhibits the largest number of discontinuities of all data sets. For the 19 years used here, they identified four so-called breakpoints due to changes in satellite data assimilation. The influence of these discontinuities should be smaller

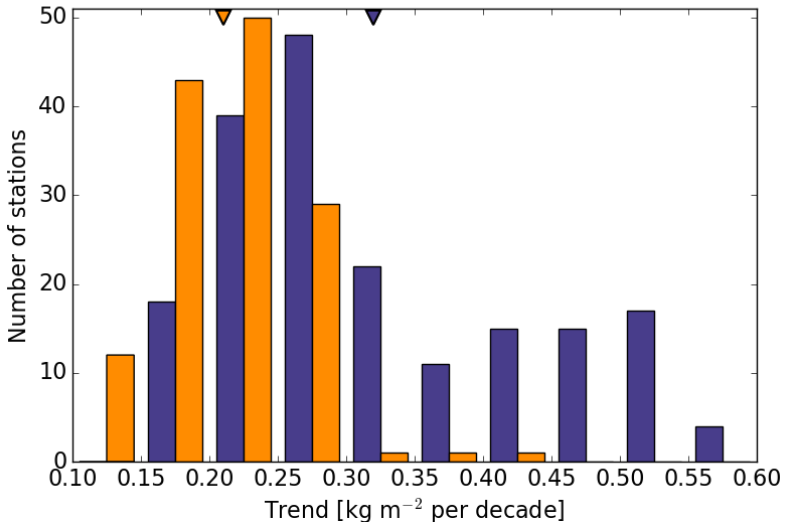

Figure 8.3: Histogram of IWV trends of COSMO-REA6 (purple) at 183 grid points and ERA-Interim (orange) at 133 grid points near GPS stations (1995–2013). The triangles represent the mean trends.

on COSMO-REA6 since no satellite data is assimilated. This could explain the different trends in the two reanalyses. Another common reason for breakpoints in model runs — change of model versions — is not pertained for the three reanalyses since all of them are runs with one model version each. The GPS observations could exhibit discontinuities due to e. g. receiver changes. However, within the quality check differences of IWV time series are checked visually for discontinuities (cf. 2.1.3.1). This should exclude most of the GPS stations with strong breakpoints.

It has to be taken into account that all trends found here are not significant due to the fact that for climatological investigations short time period and a strong seasonal variability in IWV lead to an insufficient trend/noise-relationship. However, the 19 years trends of COSMO-REA6 and ERA-Interim are similar to the trends found by other studies e. g. $0.37\,\mathrm{kg\,m^{-2}}$ per decade in radiosonde measurements in the northern Hemisphere (Durre et al., 2009), $0.4\,\mathrm{kg\,m^{-2}}$ per decade global trends in Special Sensor Microwave Imager (SSM/I) observations (Trenberth et al., 2005), and $0.18\,\mathrm{kg\,m^{-2}}$ per decade for central Europe in Global Ozone Monitoring Experiment (GOME) and SCanning Imaging Absorption spectrometer for Atmospheric CHartographY (SCIAMACHY) observations (Mieruch et al., 2008).

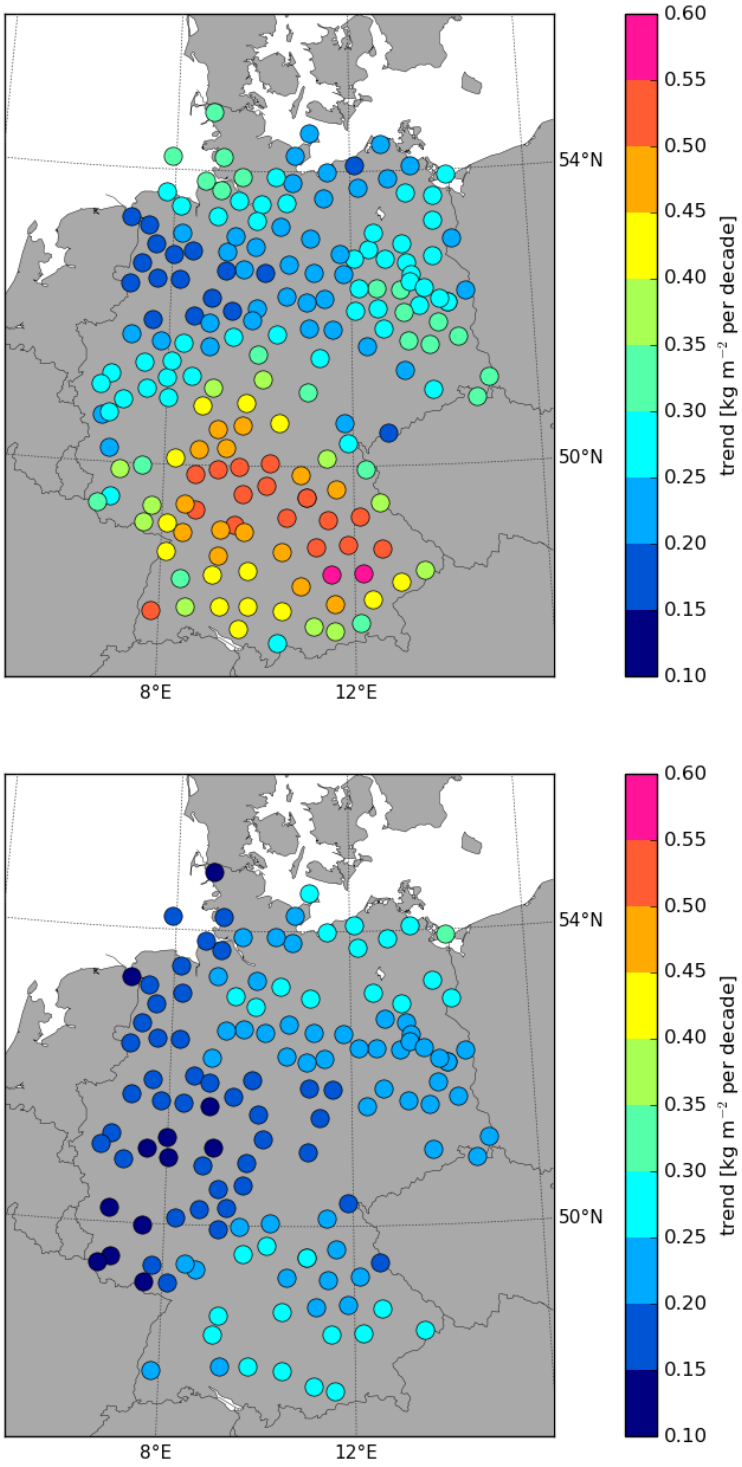

Figure 8.4: Map of IWV trends for the period 1995–2013 of COSMO-REA6 (top) at 183 grid points and ERA-Interim (bottom) at 133 grid points near GPS stations.

Part III

SUMMARY, CONCLUSIONS, AND OUTLOOK

9 SUMMARY, CONCLUSIONS, AND OUTLOOK

The present work assesses the variability of IWV on a wide range of scales from a few minutes to the diurnal cycle to trends over 19 years. To this end, various model simulations and observations are used.

9.1 SUMMARY AND CONCLUSIONS

This section will summarize the findings in order to provide an answer to the overarching question:

How large is the variability of IWV on scales from meso-γ (2–20 km) to meso-α (200–2000 km) over Germany?

To this end, the scientific questions established in Sect. 1.2 are assessed:

Q1 How well do IWV measurements of different instruments agree?

An instrument intercomparison is performed for observations of GPS, MWR, sunphotometer, radiosounding and the infrared and near-infrared retrievals of MODIS during the two months of HOPE at JOYCE. All instruments are located in close proximity to each other. In summary, this comparison shows a very good agreement between the IWV measurements on the 15 min basis with standard deviations of around $1\,\mathrm{kg\,m^{-2}}$ with the exception of MODIS.

Q2 Which instrument allows to observe the variability of IWV on which scales?

With the continuous measurements of MWR, with a temporal resolution of about 2 s, and the 15 min observations of GPS, and sunphotometer during HOPE this research question can be assessed. The standard deviations within time intervals from 5 min up to 3 h is used to quantify the variability within these time periods. During cloudy conditions standard deviations of over $1.5\,\mathrm{kg\,m^{-2}}$ within time intervals of a few hours can be observed. Considering only daytime clear-sky time periods removes the high end tail of the distribution of IWV standard deviations. Therefore, instrument intercomparisons during clear sky conditions are advantageous to assure more homogeneous conditions. This is in accordance with the instrument intercomparison described above, which shows better agreement of the IWV measurements for clear-sky daytime cases (Sect. 4).

The highly resolved IWV measurements with MWR enable to asses the variability within less than 1 h and shows that even during daytime clear-sky cases, standard deviations higher than $0.5\,\mathrm{kg\,m^{-2}}$ can

occur which is caused by turbulent transports. However, a comparison for time intervals above 30 min shows that the 15 min data sets can reproduce IWV variability with the same quality as the MWR observations.

Q3 To which degree can the COSMO reanalyses, ERA-Interim and ICON reproduce IWV and its variability and what is the benefit of high resolution simulations?

The ability of capturing IWV variability on temporal scales above 30 min, the good agreement GPS showed in the multi-instrument comparison, and a dense network of GPS stations in Germany enables GPS observations for model evaluation. Firstly, it is shown that a dynamical downscaling cannot capture the small IWV variability as good as a full reanalysis which can be seen in the much higher standard deviations between the downscaling and GPS compared to the standard deviations between the full reanalysis COSMO-REA6 and GPS. This leads to the conclusion that a full reanalysis as COSMO-REA6 is superior to a less costly downscaling.

Furthermore, the regional reanalyses COSMO-REA2 and COSMO-REA6 with horizontal resolution of 2 and 6 km, respectively, are compared with lower resolved global reanalysis ERA-Interim. On average, all reanalyses are drier than the GPS observations (0.7–1.2 $\mathrm{kg\,m^{-2}}$). The differences between the reanalyses are smaller than the regional differences. For the random error, there is a better agreement between the COSMO reanalyses and GPS observations (1.6 $\mathrm{kg\,m^{-2}}$) than between ERA-Interim and GPS (2.4 $\mathrm{kg\,m^{-2}}$). However, especially in association with convective events with strong precipitation differences of more than 20 $\mathrm{kg\,m^{-2}}$ can occur even between the two COSMO reanalysis. This leads to the conclusion that convective precipitation is associated with strong IWV variability.

The highly resolved simulations of three days over Germany with ICON in LES configuration also agree well with GPS observations (bias: 0.7 $\mathrm{kg\,m^{-2}}$, standard deviation: 1.6 $\mathrm{kg\,m^{-2}}$).

Q4 How variable is IWV on meso scales for time periods between a few minutes and a few days?

As mentioned above (**Q2**) the standard deviation within short time intervals of a few minutes can be 1.5 $\mathrm{kg\,m^{-2}}$ and larger. To assess the spatio-temporal variability on meso-γ scale ICON simulation over three days in LES configuration is used. Its high spatial resolution (156 m) and temporal output frequency (10 s–5 min) enable it for this purpose. From the spatio-temporal analysis of correlation and standard deviation for time differences smaller than 1 h and shorter than 10 km from this simulations it can be concluded that depending on the weather situation a temporal mismatch of 30–45 min or a spatial mismatch of 9–10 km can already lead to a random error of approximately 0.7 $\mathrm{kg\,m^{-2}}$. It can be even higher depending on the weather situ-

ation. As concluded from the analysis of standard deviations within time intervals, clear-sky conditions exhibit lower standard deviations. This emphasizes again that during multi-instrument comparisons the current atmospheric conditions have to be taken into account.

A combination of temporal and spatial mismatch introduces even higher errors. Measurements with two MWR confirm the results. Furthermore, it can be concluded that the standard deviation of ca. 1 kg m^{-2} found in the instrument intercomparison described above (**Q1**) cannot be explained completely with the representativeness error since a spatial distance of 4 km is estimated to introduce an error due to atmospheric variations of approximately 0.3–0.5 kg m^{-2}.

These analyses are complemented by additional two methods: auto-correlation analysis and a scale analysis of the power spectrum. The analysis (cf. Sect. 6.2) of auto-correlation (cf. Sect. 6.1) shows that the e-folding time ranges between scales of 24 and 100 h depending on season. From this, it can be concluded that synoptic processes on theses scales are associated with strongest IWV variability. The scale analysis of IWV showed that the exponent during autumn and winter on scales below 380 km is about the same as associated with temperature scaling (-3) and not with height-resolved humidity scaling in accordance with Kahn et al. (2011). This hints to a stronger relationship between temperature and IWV variability than between the variability of humidity in distinct heights and IWV.

Q5 What are the characteristics of the diurnal cycle of IWV and how is it influenced by region, season and weather situation?

To characterize the diurnal cycle of IWV the reanalyses COSMO-REA6 and ERA-Interim are used as well as GPS observations. While no clear diurnal cycle is found in autumn and winter, during spring and summer a clear diurnal cycle can be seen with a minimum in the morning (4:00–10:00 UTC) and a maximum between 14:00 and 23:00 UTC. The reanalyses exhibit a regional pattern: the time of the minimum is shifted to later times from east to west and a north-west gradient is found in the time of the maximum with earlier peaks in the north. The amplitudes of the mean diurnal IWV cycle vary between 0.4 and 2.0 kg m^{-2} (3.0–13.7%) in spring and 0.4–2.6 kg m^{-2} (1.4–12.0%) in summer for GPS. The reanalyses exhibit smaller amplitudes and lower variability in amplitudes. Furthermore, two regional peculiarities are identified: First, the land/sea-breeze effect leads to a reduction of the amplitude and a shift of the diurnal cycle. Second, at high altitudes the diurnal cycle is enhanced and maximum and minimum are shifted to later times. Concerning the weather situations, it can be concluded that over Germany western situations, which are often associated with large scale water vapour advection from the Atlantic, suppress the diurnal cycle and eastern and anti-cyclonic weather situations, which are not associated with a strong change in water vapour on large scales, allow the diurnal cycle to

evolve. This analysis shows that the representativeness of climatological means from satellite overpasses or radiosoundings once or twice a day is limited.

Q6 Is there a trend in IWV and how does it differ across Germany?

The 19 years time period which is covered by COSMO-REA6 allows for a first trend analysis. This reanalysis is complemented by ERA-Interim and for a shorter time period of 7 years also by COSMO-REA2 and GPS observations. The trend analysis is ambiguous. For the 19 years period mean positive trends of approximately $0.3\,\mathrm{kg\,m^{-2}}$ can be identified which is consent with Durre et al. (2009), Trenberth et al. (2005), and Mieruch et al. (2008) who found trends between 0.2 and $0.4\,\mathrm{kg\,m^{-2}}$. For both reanalyses an increase of the trend can be seen from west to east. The trends for the shorter time periods are negative for the reanalyses ((-0.67)–$(-0.73\,\mathrm{kg\,m^{-2}})$) and positive for GPS observations ($0.25\,\mathrm{kg\,m^{-2}}$). Due to the high natural variability even the time period of 19 years is too short to identify significant trends.

9.2 OUTLOOK

The present work characterizes IWV variability on meso scales over Germany and shows the importance of the consideration of IWV variability. However, further research is desirable to further reinforce the presented results.

Unfortunately, there are shortcomings in two of the data sets used in this study. First, the GPS observations exhibit a jump at the beginning of each hour and a smoothing of the four observations during an hour due to the NRT retrieval. A reprocessing of the data which is still under investigation by GFZ could solve these problems. Second, some external parameters of the COSMO reanalyses especially concerning the vegetation do not change depending on the month but are fixed values of November for the whole simulation period. A reproduction of these simulations which fixes the mentioned problems and includes further improvements as e. g. a newer model version and an improved aerosol scheme is already planned.

The studies on variability of IWV on meso-γ scale are conducted with observations and simulations for time periods of three days to two months on one location in Germany. Studies for a longer time period, different regions, and more diverse atmospheric conditions can show if the encouraging results can be confirmed in more general terms. Furthermore, regional or seasonal differences of the IWV variability on meso-γ scales could be assessed.

The assessment of the connection between the diurnal cycle of IWV and precipitation deserves further research. Due to the fact that precipitation is even more variable than IWV, time series with higher

temporal resolution could help to assess the connection between both atmospheric parameters. A distinction between weather situation to distinguish between different precipitation regimes could be helpful as well.

Part IV

APPENDIX

A

GPS STATIONS

Table A.1: List of GPS stations provided by GFZ with reasons for rejection (cf. Chapt. 2.1.3.1).

Name of GPS station	*reason for rejection*
0005	< 50% of time period
0010	< 50% of time period
0070	< 50% of time period
0139	< 50% of time period
0140	< 50% of time period
0143	< 50% of time period
0146	< 50% of time period
0200	< 50% of time period
0208	< 50% of time period
0212	< 50% of time period
0215	< 50% of time period
0274	< 50% of time period
0286	regular jumps in diurnal cycle
0291	regular jumps in diurnal cycle
0292	change of offset
0293	bias due to wrong surface pressure
0294	regular jumps in diurnal cycle
0512	change of offset
0513	change of offset
0526	change of offset
0527	change of offset
0529	< 50% of time period
0576	< 50% of time period
0578	< 50% of time period
0582	< 50% of time period
0583	< 50% of time period
0587	< 50% of time period
0590	< 50% of time period

Name of GPS station	*reason for rejection*
0591	< 50% of time period
0593	< 50% of time period
0594	< 50% of time period
0595	< 50% of time period
0596	< 50% of time period
0597	< 50% of time period
0599	< 50% of time period
0600	< 50% of time period
0608	< 50% of time period
0610	< 50% of time period
0712	< 50% of time period
0714	< 50% of time period
0716	< 50% of time period
0718	< 50% of time period
0719	< 50% of time period
0769	< 50% of time period
0791	change of offset
0793	change of offset
0795	change of offset
0797	change of offset
0799	change of offset
0928	change of offset
0930	change of offset
0931	< 50% of time period
0932	change of offset
1385	< 50% of time period
1393	< 50% of time period
1399	< 50% of time period
2576	change of offset
2578	unidentified patterns
2579	unidentified patterns
2590	unidentified patterns
2591	unidentified patterns
2599	< 50% of time period
2604	< 50% of time period
2623	bias due to wrong surface pressure
AURI	change of offset

Name of GPS station	*reason for rejection*
BOR1	change of offset
BORK	< 50% of time period
BRUS	< 50% of time period
BSCN	< 50% of time period
BUDP	bias due to wrong surface pressure
COTT	< 50% of time period
DES3	< 50% of time period
EFBG	change of offset
FEHR	< 50% of time period
GIES	< 50% of time period
GOE2	< 50% of time period
GOPE	< 50% of time period
GPO1	< 50% of time period
GPO2	< 50% of time period
GRAZ	bias due to wrong surface pressure
HANN	< 50% of time period
HERZ	< 50% of time period
HOBU	change of offset
KARL	change of offset
KIEL	< 50% of time period
MAG5	< 50% of time period
MLVL	< 50% of time period
NORD	< 50% of time period
OBE2	< 50% of time period
OSNA	change of offset
POTS	< 50% of time period
PREN	< 50% of time period
PTBB	< 50% of time period
ROST	< 50% of time period
SAL2	< 50% of time period
SCHL	< 50% of time period
SMSP	< 50% of time period
SWED	< 50% of time period
SYLT	< 50% of time period
TANZ	< 50% of time period
TORI	< 50% of time period
ULM1	< 50% of time period

Name of GPS station	*reason for rejection*
VIER	< 50% of time period
WEID	< 50% of time period
WEIL	< 50% of time period
WITT	< 50% of time period
WROC	< 50% of time period
WTZR	< 50% of time period
WUE2	< 50% of time period
WUEN	< 50% of time period
WUER	< 50% of time period

B

TEMPORAL AND SPATIAL VARIABILITY

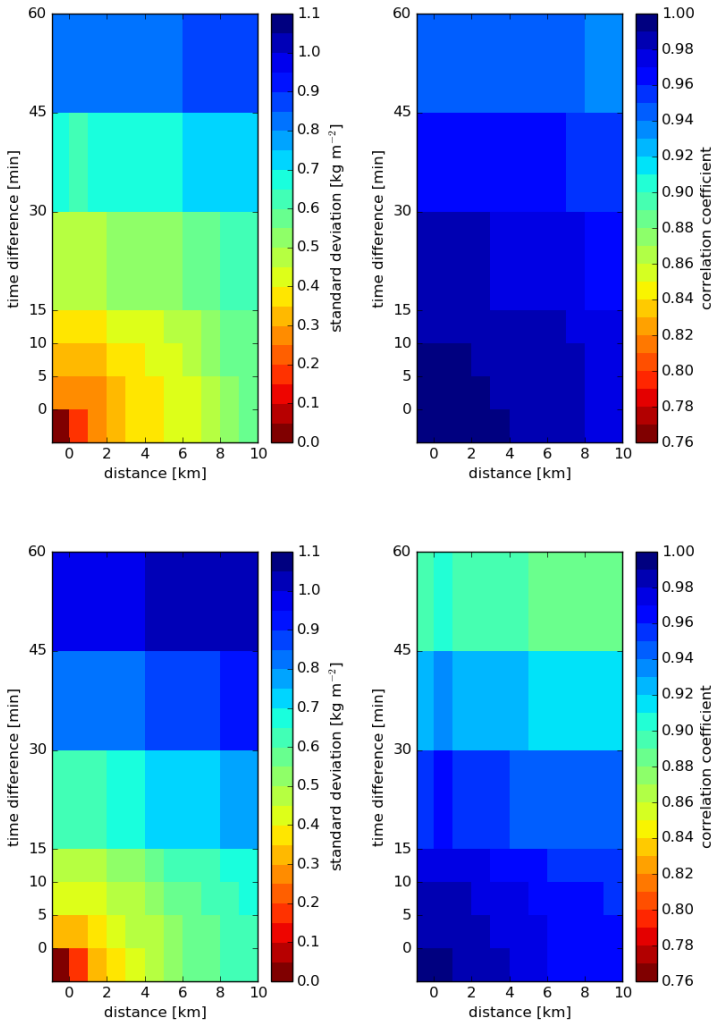

Figure B.1: Standard deviations (left) and correlation coefficients (right) of IWV with artificially reduced temporal resolution of 5 min from ICON grid points (simulation for (top) 24 April, (bottom) 25 April) as a function of temporal and spatial distance.

C

DIURNAL CYCLE OF COSMO-REA2

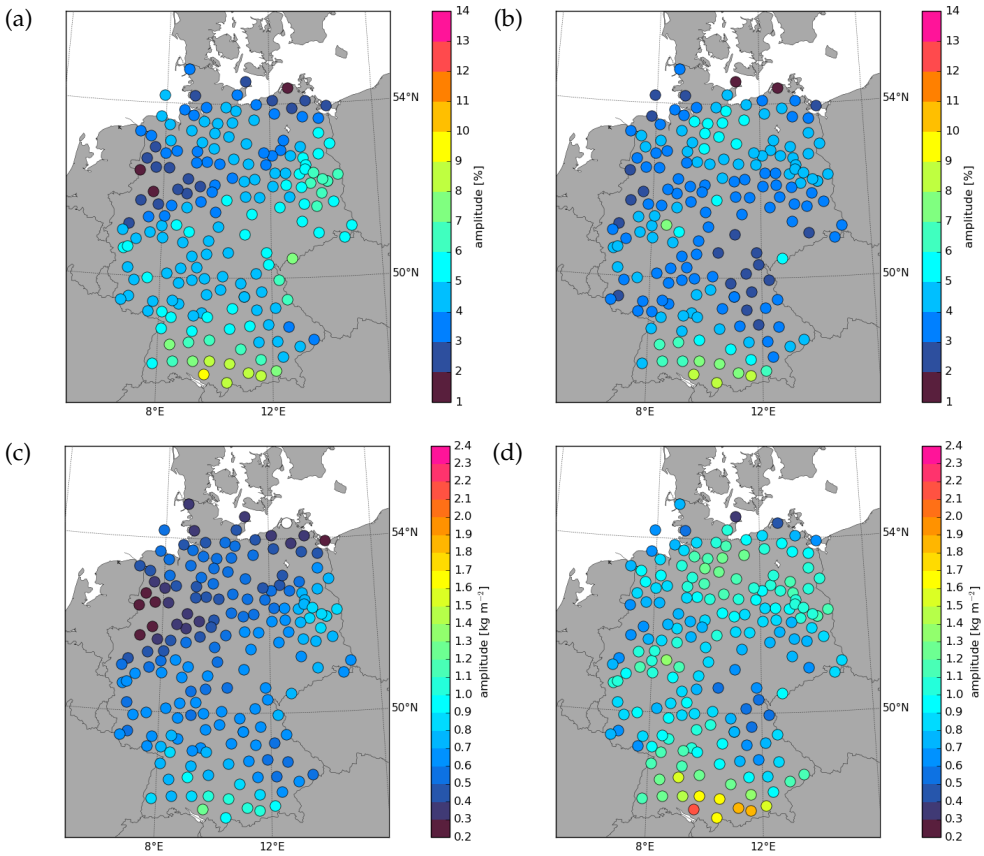

Figure C.1: (a)–(b) Relative amplitude, and (c)–(d) absolute amplitude of diurnal cycle of IWV simulated with COSMO-REA2 at 183 grid-points near GPS stations in Germany for (a), (c) spring and (b), (d) summer of the years 2007–2013.

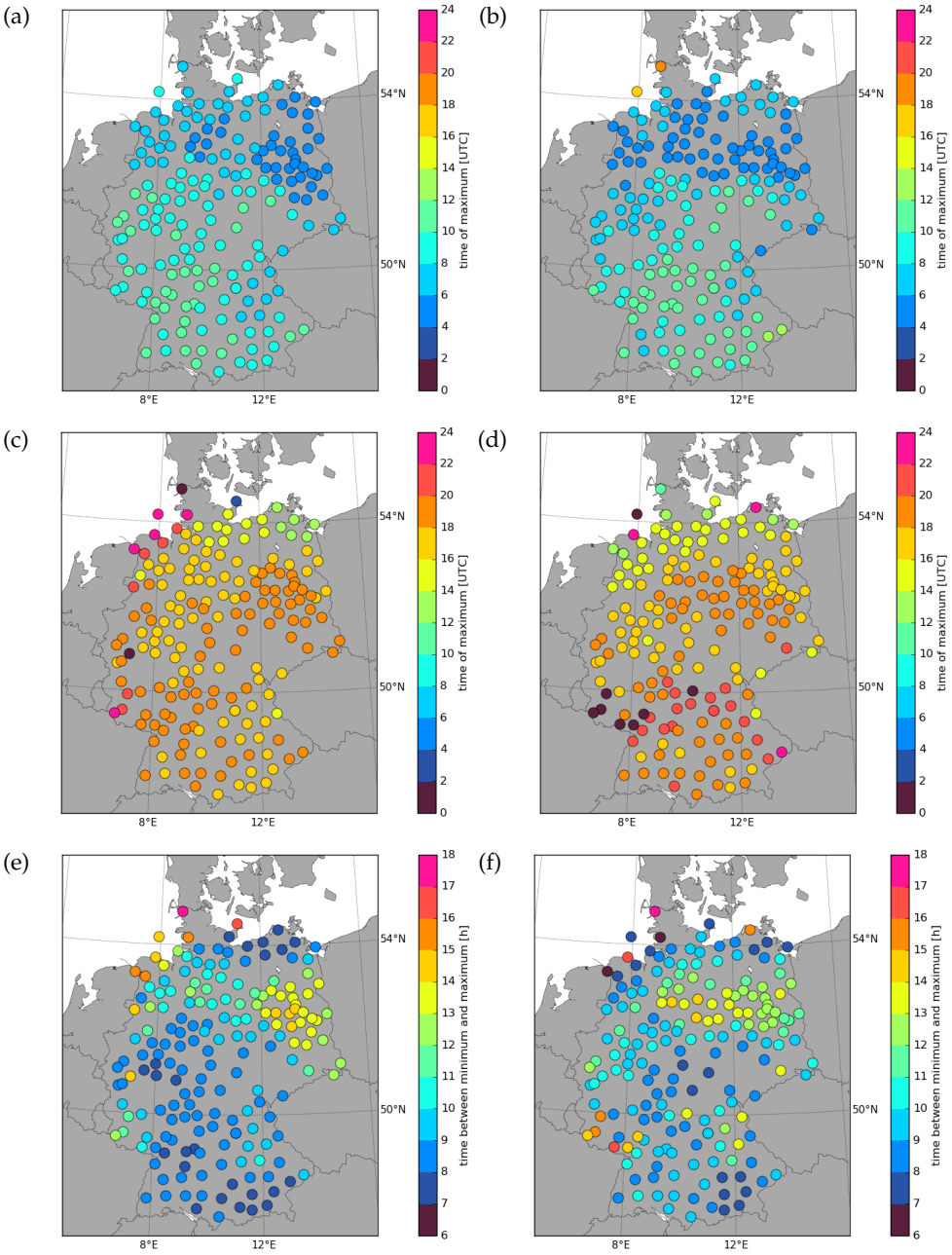

Figure C.2: (a)–(b) Time of minimum, (c)–(d) time of maximum of diurnal cycle of IWV, and (e)–(f) time after minimum until maximum of diurnal cycle occurs simulated with COSMO-REA2 at 183 grid-points near GPS stations in Germany for (a), (c) spring and (b), (d) summer of the years 2007–2013.

BIBLIOGRAPHY

Akkermans, T., Böhme, T., Demuzere, M., Crewell, S., Selbach, C., Reinhardt, T., Seifert, A., Ament, F., and Lipzig, N. P. M. v. (2011). Regime-dependent evaluation of accumulated precipitation in COSMO. *Theoretical and Applied Climatology*, 108(1-2):39–52.

Alexandrov, M. D., Schmid, B., Turner, D. D., Cairns, B., Oinas, V., Lacis, A. A., Gutman, S. I., Westwater, E. R., Smirnov, A., and Eilers, J. (2009). Columnar water vapor retrievals from multifilter rotating shadowband radiometer data. *Journal of Geophysical Research: Atmospheres*, 114(D2):D02306.

Arakawa, A. and Lamb, V. R. (1977). Computational Design of the Basic Dynamical Processes of the UCLA General Circulation Model. In Chang, J., editor, *Methods in Computational Physics: Advances in Research and Applications*, volume 17 of *General Circulation Models of the Atmosphere*, pages 173–265. Elsevier.

Baldauf, M., Seifert, A., Förstner, J., Majewski, D., Raschendorfer, M., and Reinhardt, T. (2011). Operational Convective-Scale Numerical Weather Prediction with the COSMO Model: Description and Sensitivities. *Monthly Weather Review*, 139(12):3887–3905.

Bengtsson, L., Bonnet, R.-M., Calisto, M., Destouni, G., Gurney, R., Johannsessen, J., Kerr, Y., Lahoz, W., and Rast, M. (2014). *The Earth's Hydrological Cycle*. Springer.

Bennouna, Y. S., Torres, B., Cachorro, V. E., Ortiz de Galisteo, J. P., and Toledano, C. (2013). The evaluation of the integrated water vapour annual cycle over the Iberian Peninsula from EOS-MODIS against different ground-based techniques. *Quarterly Journal of the Royal Meteorological Society*, 139(676):1935 – 1956.

Bevis, M., Businger, S., Herring, T. A., Rocken, C., Anthes, R. A., and Ware, R. H. (1992). GPS meteorology: Remote sensing of atmospheric water vapor using the global positioning system. *Journal of Geophysical Research: Atmospheres*, 97(D14):15787–15801.

Bokoye, A. I., Royer, A., O'Neill, N. T., Cliche, P., McArthur, L. J. B., Teillet, P. M., Fedosejevs, G., and Thériault, J.-M. (2003). Multisensor analysis of integrated atmospheric water vapor over Canada and Alaska. *Journal of Geophysical Research: Atmospheres*, 108(D15):4480.

Bollmeyer, C., Keller, J. D., Ohlwein, C., Wahl, S., Crewell, S., Friederichs, P., Hense, A., Keune, J., Kneifel, S., Pscheidt, I., Redl,

S., and Steinke, S. (2015). Towards a high-resolution regional reanalysis for the European CORDEX domain. *Quarterly Journal of the Royal Meteorological Society*, 141(686):1–15.

Bony, S., Colman, R., Kattsov, V. M., Allan, R. P., Bretherton, C. S., Dufresne, J.-L., Hall, A., Hallegatte, S., Holland, M. M., Ingram, W., Randall, D. A., Soden, B. J., Tselioudis, G., and Webb, M. J. (2006). How Well Do We Understand and Evaluate Climate Change Feedback Processes? *Journal of Climate*, 19(15):3445–3482.

Buehler, S. A., Östman, S., Melsheimer, C., Holl, G., Eliasson, S., John, V. O., Blumenstock, T., Hase, F., Elgered, G., Raffalski, U., Nasuno, T., Satoh, M., Milz, M., and Mendrok, J. (2012). A multi-instrument comparison of integrated water vapour measurements at a high latitude site. *Atmospheric Chemistry and Physics*, 12(22):10925–10943.

Böhme, T., Stapelberg, S., Akkermans, T., Crewell, S., Fischer, J., Reinhardt, T., Seifert, A., Selbach, C., and Van Lipzig, N. (2011). Long-term evaluation of COSMO forecasting using combined observational data of the GOP period. *Meteorologische Zeitschrift*, 20(2):119–132.

Cai, C. and Gao, Y. (2013). Modeling and assessment of combined GPS/GLONASS precise point positioning. *GPS Solutions*, 17(2):223–236.

Cho, J. Y. N., Newell, R. E., and Sachse, G. W. (2000). Anomalous scaling of mesoscale tropospheric humidity fluctuations. *Geophysical Research Letters*, 27(3):377–380.

Dai, A., Wang, J., Ware, R. H., and Van Hove, T. (2002). Diurnal variation in water vapor over North America and its implications for sampling errors in radiosonde humidity. *Journal of Geophysical Research*, 107(D10):4090.

Dee, D. P., Uppala, S. M., Simmons, A. J., Berrisford, P., Poli, P., Kobayashi, S., Andrae, U., Balmaseda, M. A., Balsamo, G., Bauer, P., Bechtold, P., Beljaars, A. C. M., van de Berg, L., Bidlot, J., Bormann, N., Delsol, C., Dragani, R., Fuentes, M., Geer, A. J., Haimberger, L., Healy, S. B., Hersbach, H., Hólm, E. V., Isaksen, L., Kållberg, P., Köhler, M., Matricardi, M., McNally, A. P., Monge-Sanz, B. M., Morcrette, J.-J., Park, B.-K., Peubey, C., de Rosnay, P., Tavolato, C., Thépaut, J.-N., and Vitart, F. (2011). The ERA-Interim reanalysis: configuration and performance of the data assimilation system. *Quarterly Journal of the Royal Meteorological Society*, 137(656):553–597.

Deng, Z., Bender, M., Zus, F., Ge, M., Dick, G., Ramatschi, M., Wickert, J., Löhnert, U., and Schön, S. (2011). Validation of tropospheric slant path delays derived from single and dual frequency GPS receivers. *Radio Science*, 46(6):RS6007.

Diedrich, H., Wittchen, F., Preusker, R., and Fischer, J. (2016). Representativeness of total column water vapour retrievals from instruments on polar orbiting satellites. *Atmospheric Chemistry and Physics*, 16(13):8331–8339.

Doms, G., Förstner, J., Heise, E., Herzog, H.-J., Mironov, D., Raschendorfer, M., Reinhardt, T., Ritter, B., Schrodin, R., Schulz, J.-P., and Vogel, G. (2011). A Description of the Nonhydrostatic Regional COSMO Model Part II : Physical Parameterization. Technical report, Consortium for Small-Scale Modelling.

Dubovik, O., Sinyuk, A., Lapyonok, T., Holben, B. N., Mishchenko, M., Yang, P., Eck, T. F., Volten, H., Muñoz, O., Veihelmann, B., van der Zande, W. J., Leon, J.-F., Sorokin, M., and Slutsker, I. (2006). Application of spheroid models to account for aerosol particle nonsphericity in remote sensing of desert dust. *Journal of Geophysical Research: Atmospheres*, 111(D11):D11208.

Durre, I., Williams, C. N., Yin, X., and Vose, R. S. (2009). Radiosonde-based trends in precipitable water over the Northern Hemisphere: An update. *Journal of Geophysical Research: Atmospheres*, 114(D5):D05112.

Elósegui, P., Davis, J. L., Jaldehag, R. T. K., Johansson, J. M., Niell, A. E., and Shapiro, I. I. (1995). Geodesy using the Global Positioning System: The effects of signal scattering on estimates of site position. *Journal of Geophysical Research: Solid Earth*, 100(B6):9921–9934.

Fischer, L., Craig, G. C., and Kiemle, C. (2013). Horizontal structure function and vertical correlation analysis of mesoscale water vapor variability observed by airborne lidar. *Journal of Geophysical Research: Atmospheres*, 118(14):7579–7590.

Fischer, L., Kiemle, C., and Craig, G. C. (2012). Height-resolved variability of midlatitude tropospheric water vapor measured by an airborne lidar. *Geophysical Research Letters*, 39(6):L06803.

Gao, B.-C. and Kaufman, Y. J. (2003). Water vapor retrievals using Moderate Resolution Imaging Spectroradiometer (MODIS) near-infrared channels. *Journal of Geophysical Research: Atmospheres*, 108(D13):4389.

Gendt, G., Dick, G., Reigber, C., Tomassini, M., Liu, Y., and Ramatschi, M. (2004). Near Real Time GPS Water Vapor Monitoring for Numerical Weather Prediction in Germany. *Journal of the Meteorological Society of Japan*, 82(1B):361–370.

Gérard, E., Tan, D. G. H., Garand, L., Wulfmeyer, V., Ehret, G., and Di Girolamo, P. (2004). Major Advances Foreseen in Humidity Pro-

filing from the Water Vapour Lidar Experiment in Space (WALES). *Bulletin of the American Meteorological Society*, 85(2):237–251.

Hamilton, K., Takahashi, Y. O., and Ohfuchi, W. (2008). Mesoscale spectrum of atmospheric motions investigated in a very fine resolution global general circulation model. *Journal of Geophysical Research: Atmospheres*, 113(D18):D18110.

Heinze, R., Dipankar, A., Carbajal Henken, C., Moseley, C., Sourdeval, O., Trömel, S., Xie, X., Adamidis, P., Ament, F., Baars, H., Barthlott, C., Behrendt, A., Blahak, U., Bley, S., Brdar, S., Brueck, M., Crewell, S., Deneke, H., Di Girolamo, P., Evaristo, R., Fischer, J., Frank, C., Friederichs, P., Göcke, T., Gorges, K., Hande, L., Hanke, M., Hansen, A., Hege, H.-C., Hoose, C., Jahns, T., Kalthoff, N., Klocke, D., Kneifel, S., Knippertz, P., Kuhn, A., van Laar, T., Macke, A., Maurer, V., Mayer, B., Meyer, C. I., Muppa, S. K., Neggers, R. A. J., Orlandi, E., Pantillon, F., Pospichal, B., Röber, N., Scheck, L., Seifert, A., Seifert, P., Senf, F., Siligam, P., Simmer, C., Steinke, S., Stevens, B., Wapler, K., Weniger, M., Wulfmeyer, V., Zängl, G., Zhang, D., and Quaas, J. (2016). Large-eddy simulations over Germany using ICON: A comprehensive evaluation. *Quarterly Journal of the Royal Meteorological Society*, in publication.

Held, I. M. and Soden, B. J. (2006). Robust Responses of the Hydrological Cycle to Global Warming. *Journal of Climate*, 19(21):5686–5699.

Ingold, T., Schmid, B., Mätzler, C., Demoulin, P., and Kämpfer, N. (2000). Modeled and empirical approaches for retrieving columnar water vapor from solar transmittance measurements in the 0.72, 0.82, and 0.94 μm absorption bands. *Journal of Geophysical Research: Atmospheres*, 105(D19):24327–24343.

Jakobson, E., Keernik, H., Luhamaa, A., and Ohvril, H. (2014). Diurnal variability of water vapour in the Baltic Sea region according to NCEP-CFSR and BaltAn65 + reanalyses. *Oceanologia*, 56(2):191–204.

Janssen, M. A. (1993). *An Introduction to the Passive Remote Sensing of Atmospheres*. Atmospheric Remote Sensing by Microwave Radiometry. J. Wiley & Sons, Inc, New York.

Kahn, B. H. and Teixeira, J. (2009). A Global Climatology of Temperature and Water Vapor Variance Scaling from the Atmospheric Infrared Sounder. *Journal of Climate*, 22(20):5558–5576.

Kahn, B. H., Teixeira, J., Fetzer, E. J., Gettelman, A., Hristova-Veleva, S. M., Huang, X., Kochanski, A. K., Köhler, M., Krueger, S. K., Wood, R., and Zhao, M. (2011). Temperature and water vapor variance scaling in global models: Comparison to satellite and aircraft data. *Journal of the Atmospheric Sciences*, 68:2156–2168.

Kiehl, J. T. and Trenberth, K. E. (1997). Earth's Annual Global Mean Energy Budget. *Bulletin of the American Meteorological Society*, 78(2):197–208.

Labbouz, L., Van Baelen, J., and Duroure, C. (2015). Investigation of the links between water vapor field evolution and rain rate based on 5 years of measurements at a midlatitude site. *Geophysical Research Letters*, 42(21):2015GL066048.

Li, X., Zhang, X., Ren, X., Fritsche, M., Wickert, J., and Schuh, H. (2015). Precise positioning with current multi-constellation Global Navigation Satellite Systems: GPS, GLONASS, Galileo and BeiDou. *Scientific Reports*, 5:8328.

Lorenz, C. and Kunstmann, H. (2012). The Hydrological Cycle in Three State-of-the-Art Reanalyses: Intercomparison and Performance Analysis. *Journal of Hydrometeorology*, 13(5):1397–1420.

Löhnert, U. and Crewell, S. (2003). Accuracy of cloud liquid water path from ground-based microwave radiometry 1. Dependency on cloud model statistics. *Radio Science*, 38(3):8041.

Löhnert, U., Schween, J. H., Acquistapace, C., Ebell, K., Maahn, M., Barrera-Verdejo, M., Hirsikko, A., Bohn, B., Knaps, A., O'Connor, E., Simmer, C., Wahner, A., and Crewell, S. (2015). JOYCE: Jülich Observatory for Cloud Evolution. *Bulletin of the American Meteorological Society*, 96(7):1157–1174.

Löhnert, U., Turner, D. D., and Crewell, S. (2009). Ground-Based Temperature and Humidity Profiling Using Spectral Infrared and Microwave Observations. Part I: Simulated Retrieval Performance in Clear-Sky Conditions. *Journal of Applied Meteorology and Climatology*, 48(5):1017–1032.

Martin, L., Mätzler, C., Hewison, T. J., and Ruffieux, D. (2006). Intercomparison of integrated water vapour measurements. *Meteorologische Zeitschrift*, 15(1):57–64.

Maschwitz, G., Löhnert, U., Crewell, S., Rose, T., and Turner, D. D. (2013). Investigation of ground-based microwave radiometer calibration techniques at 530 hPa. *Atmospheric Measurement Techniques*, 6(10):2641–2658.

Mieruch, S., Noël, S., Bovensmann, H., and Burrows, J. P. (2008). Analysis of global water vapour trends from satellite measurements in the visible spectral range. *Atmospheric Chemistry and Physics*, 8(3):491–504.

Morland, J., Collaud Coen, M., Hocke, K., Jeannet, P., and Mätzler, C. (2009). Tropospheric water vapour above Switzerland over the last 12 years. *Atmospheric Chemistry and Physics*, 9(16):5975–5988.

Nash, J., Oakley, T., Vömel, H., and Wei, L. (2011). WMO intercomparison of high quality radiosonde systems, Yangjiang, China, 12 July-3 August 2010. Tech. Rep. 107, World Meteorological Organization.

Nastrom, G. D., Gage, K. S., and Jasperson, W. H. (1984). Kinetic energy spectrum of large-and mesoscale atmospheric processes. *Nature*, 310(5972):36–38.

Niell, A. E. (1996). Global mapping functions for the atmosphere delay at radio wavelengths. *Journal of Geophysical Research: Solid Earth*, 101(B2):3227–3246.

Ning, T. and Elgered, G. (2012). Trends in the Atmospheric Water Vapor Content From Ground-Based GPS: The Impact of the Elevation Cutoff Angle. *IEEE Journal of Selected Topics in Applied Earth Observations and Remote Sensing*, 5(3):744–751.

Pałm, M., Melsheimer, C., Noël, S., Heise, S., Notholt, J., Burrows, J., and Schrems, O. (2010). Integrated water vapor above Ny Ålesund, Spitsbergen: a multi-sensor intercomparison. *Atmospheric Chemistry and Physics*, 10(3):1215–1226.

Philipp, A., Beck, C., Huth, R., and Jacobeit, J. (2016). Development and comparison of circulation type classifications using the COST 733 dataset and software. *International Journal of Climatology*, 36(7):2673–2691.

Pressel, K. G., Collins, W. D., and Desai, A. R. (2014). The spatial scale dependence of water vapor variability inferred from observations from a very tall tower. *Journal of Geophysical Research: Atmospheres*, 119(16):9822–9837.

Ritter, B. and Geleyn, J.-F. (1992). A Comprehensive Radiation Scheme for Numerical Weather Prediction Models with Potential Applications in Climate Simulations. *Monthly Weather Review*, 120(2):303–325.

Rose, T., Crewell, S., Löhnert, U., and Simmer, C. (2005). A network suitable microwave radiometer for operational monitoring of the cloudy atmosphere. *Atmospheric Research*, 75(3):183–200.

Saastamoinen, J. (1972). Atmospheric correction for the troposphere and stratosphere in radio ranging satellites. In Henriksen, S. W., Mancini, A., and Chovitz, B. H., editors, *Geophysical Monograph Series*, volume 15, pages 247–251. American Geophysical Union, Washington, D. C.

Schmid, B., Michalsky, J. J., Slater, D. W., Barnard, J. C., Halthore, R. N., Liljegren, J. C., Holben, B. N., Eck, T. F., Livingston, J. M., Rus-

sell, P. B., Ingold, T., and Slutsker, I. (2001). Comparison of columnar water-vapor measurements from solar transmittance methods. *Applied optics*, 40(12):1886–1896.

Schneider, M., Romero, P. M., Hase, F., Blumenstock, T., Cuevas, E., and Ramos, R. (2010). Continuous quality assessment of atmospheric water vapour measurement techniques: FTIR, Cimel, MFRSR, GPS, and Vaisala RS92. *Atmospheric Measurement Techniques*, 3(2):323–338.

Schröder, M., Lockhoff, M., Forsythe, J. M., Cronk, H. Q., Vonder Haar, T. H., and Bennartz, R. (2016). The GEWEX Water Vapor Assessment: Results from Intercomparison, Trend, and Homogeneity Analysis of Total Column Water Vapor. *Journal of Applied Meteorology and Climatology*, 55(7):1633–1649.

Seeber, G. (2008). *Satellite Geodesy*. Walter de Gruyter.

Seemann, S. W., Li, J., Menzel, W. P., and Gumley, L. E. (2003). Operational Retrieval of Atmospheric Temperature, Moisture, and Ozone from MODIS Infrared Radiances. *Journal of Applied Meteorology*, 42(8):1072–1091.

Shao, Y., Liu, S., Schween, J. H., and Crewell, S. (2013). Large-Eddy Atmosphere–Land-Surface Modelling over Heterogeneous Surfaces: Model Development and Comparison with Measurements. *Boundary-Layer Meteorology*, 148(2):333–356.

Sherwood, S. C., Roca, R., Weckwerth, T. M., and Andronova, N. G. (2010). Tropospheric water vapor, convection, and climate. *Reviews of Geophysics*, 48(2):RG2001.

Simmer, C., Adrian, G., Jones, S., Wirth, V., Göber, M., Hohenegger, C., Janjic, T., Keller, J., Ohlwein, C., Seifert, A., Trömel, S., Ulbrich, T., Wapler, K., Weissmann, M., Keller, J., Masbou, M., Meilinger, S., Riß, N., Schomburg, A., Vormann, A., and Weingärtner, C. (2015). HErZ - The German Hans-Ertel Centre for Weather Research. *Bulletin of the American Meteorological Society*.

Steinke, S., Eikenberg, S., Löhnert, U., Dick, G., Klocke, D., Di Girolamo, P., and Crewell, S. (2015). Assessment of small-scale integrated water vapour variability during HOPE. *Atmospheric Chemistry and Physics*, 15(5):2675–2692.

Steppeler, J., Doms, G., Schättler, U., Bitzer, H. W., Gassmann, A., Damrath, U., and Gregoric, G. (2003). Meso-gamma scale forecasts using the nonhydrostatic model LM. *Meteorology and Atmospheric Physics*, 82(1-4):75–96.

Stevens, B. and Bony, S. (2013). What Are Climate Models Missing? *Science*, 340(6136):1053–1054.

Stoew, B., Elgered, G., and Johansson, J. M. (2001). An assessment of estimates of integrated water vapor from ground-based GPS data. *Meteorology and Atmospheric Physics*, 77(1-4):99–107.

Thayer, G. D. (1974). An improved equation for the radio refractive index of air. *Radio Science*, 9(10):803–807.

Tiedtke, M. (1989). A Comprehensive Mass Flux Scheme for Cumulus Parameterization in Large-Scale Models. *Monthly Weather Review*, 117(8):1779–1800.

Torres, B., Cachorro, V. E., Toledano, C., Ortiz de Galisteo, J. P., Berjón, A., de Frutos, A. M., Bennouna, Y., and Laulainen, N. (2010). Precipitable water vapor characterization in the Gulf of Cadiz region (southwestern Spain) based on Sun photometer, GPS, and radiosonde data. *Journal of Geophysical Research: Atmospheres*, 115(D18):D18103.

Trenberth, K. E., Fasullo, J., and Smith, L. (2005). Trends and variability in column-integrated atmospheric water vapor. *Climate Dynamics*, 24(7-8):741–758.

Wahl, S., Bollmeyer, C., Crewell, S., Figura, C., Friederichs, P., Hense, A., Keller, J., and Ohlwein, C. (2016). A novel convective-scale regional reanalysis COSMO-REA2: Improving the representation of precipitation. *Meteorologische Zeitschrift*, submitted September 2016.

Wang, J. and Zhang, L. (2008). Systematic Errors in Global Radiosonde Precipitable Water Data from Comparisons with Ground-Based GPS Measurements. *Journal of Climate*, 21(10):2218–2238.

Weissmann, M., Göber, M., Hohenegger, C., Janjic, T., Keller, J., Ohlwein, C., Seifert, A., Trömel, S., Ulbrich, T., Wapler, K., Bollmeyer, C., and Deneke, H. (2014). Initial phase of the Hans-Ertel Centre for Weather Research — A virtual centre at the interface of basic and applied weather and climate research. *Meteorologische Zeitschrift*, 23(3):193–208.

Welch, P. (1967). The use of fast Fourier transform for the estimation of power spectra: A method based on time averaging over short, modified periodograms. *IEEE Transactions on Audio and Electroacoustics*, 15(2):70–73.

Wickert, J., Michalak, G., Schmidt, T., Beyerle, G., Cheng, C.-Z., Healy, S. B., Heise, S., Huang, C.-Y., Jakowski, N., Köhler, W., Mayer, C., Offiler, D., Ozawa, E., Pavelyev, A. G., Rothacher, M., Tapley, B., and Köhler, C. (2009). GPS Radio Occultation: Results from CHAMP, GRACE and FORMOSAT-3/COSMIC. *Terrestrial, Atmospheric and Oceanic Sciences*, 20(1):35.

Younes, S. A. and Elmezayen, A. G. (2012). A comprehensive comparison of atmospheric mapping functions for GPS measurements in Egypt. *Journal of Geodetic Science*, 2(3):216–223.

Zumberge, J. F., Heflin, M. B., Jefferson, D. C., Watkins, M. M., and Webb, F. H. (1997). Precise point positioning for the efficient and robust analysis of GPS data from large networks. *Journal of Geophysical Research: Solid Earth*, 102(B3):5005–5017.

Zängl, G., Reinert, D., Rípodas, P., and Baldauf, M. (2014). The ICON (ICOsahedral Non-hydrostatic) modelling framework of DWD and MPI-M: Description of the non-hydrostatic dynamical core. *Quarterly Journal of the Royal Meteorological Society*, 141(687):1490 – 1504.

DANKSAGUNG

Diese Arbeit wurde im Rahmen des Hans-Ertel-Zentrum für Wetterforschung (HErZ) ausgführt. Dieses Netzwerk aus Universitäten, Forschungsinstituten und dem Deutschen Wetterdienst wird vom Bundesministerium für Verkehr, Bau und Stadtentwicklung (BMVBS) finanziert. Die ICON Simulation wurde im Rahmen von HD(CP)^2, finanziert vom Bundesministerium für Bildung und Forschung (BMBF), erstellt und die Messungen stammen zum Teil aus dem HD(CP)^2 Observational Prototype Experiment (HOPE).

Vielen Dank an Susanne für die Begutachtung und Betreuung der Arbeit. Du hast dir immer Zeit genommen, mir mit Rat und Tat zur Seite zu stehen.

Danke Roel, dafür, dass du dich bereit erklärt hat, diese Arbeit zu begutachten.

Mein Dank geht auch an die weiteren Mitglieder meines Doctoral Comitees für ihren Rat, an Harrie-Jan und an Matthieu, der es immer geschafft hat mich mit seiner Begeisterung für meine Arbeit anzustecken.

Vielen Dank auch an Galina und das GeoForschungsZentrum Potsdam (GFZ) Potsdam für die Bereitstellung der GPS Messungen.

Ein großer Dank geht auch an Chris, Clarissa und Christopher, für den Transfer mehrere Terabyte Reanalyse Daten nach Köln und an das übrige Bonner HErZ-Team, insbesondere an Sabrina.

Liebe Infernos und InScapes, danke für die schöne Zeit in den letzten Jahren. Ganz besonderer Dank geht dabei an Sarah, Vera, Kerstin, Lisa, Karin, Nadine und Mario für die moralische Unterstützung. Vera gebührt weiterer Dank fürs Korrekturlesen. Nicht zu vergessen, Danke an Sebastian und Claudia für das gemeinsame Durchstehen des Endspurts.

Sonja, Max auch wenn ihr nicht mehr hier seid, ich habe euch nicht vegessen.

Vielen Dank an alle Freunde, die mich regelmäßig auf andere Gedanken gebracht und vom Arbeiten abgehalten haben.

Konrad, vielen Dank für deine Geduld, Unterstützung und Liebe.

Ganz besonderer Dank gilt auch meiner Familie für ihre Unterstützung. Meiner Mutter danke ich dafür, dass sie mich stets ermutigt hat, neugierig zu sein.

ERKLÄRUNG

Ich versichere, dass ich die von mir vorgelegte Dissertation selbständig angefertigt, die benutzten Quellen und Hilfsmittel vollständig angegeben und die Stellen der Arbeit - einschließlich Tabellen, Karten und Abbildungen -, die anderen Werken im Wortlaut oder dem Sinn nach entnommen sind, in jedem Einzelfall als Entlehnung kenntlich gemacht habe; dass diese Dissertation noch keiner anderen Fakultät oder Universität zur Prüfung vorgelegen hat; dass sie - abgesehen von unten angegebenen Teilpublikationen - noch nicht veröffentlich worden ist, sowie dass ich eine solche Veröffentlichung vor Abschluss des Promotionsverfahrens nicht vornehmen werde. Die Bestimmungen der Promotionsordnung sind mir bekannt. Die von mir vorgelegte Dissertation ist von Prof. Dr. Susanne Crewell betreut worden.

Köln, Mai 2017

Sandra Steinke

Teilpublikationen

Steinke, S., Eikenberg, S., Löhnert, U., Dick, G., Klocke, D., Di Girolamo, P., and Crewell, S. (2015). Assessment of small-scale integrated water vapour variability during HOPE. *Atmospheric Chemistry and Physics*, 15(5):2675–2692.

Bollmeyer, C., Keller, J. D., Ohlwein, C., Wahl, S., Crewell, S., Friederichs, P., Hense, A., Keune, J., Kneifel, S., Pscheidt, I., Redl, S., and Steinke, S. (2015). Towards a high-resolution regional reanalysis for the European CORDEX domain. *Quarterly Journal of the Royal Meteorological Society*, 141(686):1–15.